Characterization of HgCdTe and HgCdSe Materials

for Third Generation Infrared Detectors

by

Wenfeng Zhao

A Dissertation Presented in Partial Fulfillment
of the Requirements for the Degree
Doctor of Philosophy

Approved November 2011 by the
Graduate Supervisory Committee:

David J. Smith, Chair
Martha McCartney
Ray Carpenter
Peter Bennett
Michael J. Treacy

ARIZONA STATE UNIVERSITY

December 2011

ABSTRACT

HgCdTe is the dominant material currently in use for infrared (IR) focal-plane-array (FPA) technology. In this dissertation, transmission electron microscopy (TEM) was used for the characterization of epitaxial HgCdTe epilayers and HgCdTe-based devices.

The microstructure of CdTe surface passivation layers deposited either by hot-wall epitaxy (HWE) or molecular beam epitaxy (MBE) on HgCdTe heterostructures was evaluated. The as-deposited CdTe passivation layers were polycrystalline and columnar. The CdTe grains were larger and more irregular when deposited by HWE, whereas those deposited by MBE were generally well-textured with mostly vertical grain boundaries. Observations and measurements using several TEM techniques showed that the CdTe/HgCdTe interface became considerably more abrupt after annealing, and the crystallinity of the CdTe layer was also improved.

The microstructure and compositional profiles of CdTe(211)B/ZnTe/Si(211) heterostructures grown by MBE was investigated. Many inclined {111}-type stacking faults were present throughout the thin ZnTe layer, terminating near the point of initiation of CdTe growth. A rotation angle of about 3.5° was observed between lattice planes of the Si substrate and the final CdTe epilayer. Lattice parameter measurement and elemental profiles indicated that some local intermixing of Zn and Cd had taken place. The average widths of the ZnTe layer and the (Cd, Zn)Te transition region were found to be roughly 6.5 nm and 3.5 nm, respectively.

Initial observations of CdTe(211)B/GaAs(211) heterostructures indicated much reduced defect densities near the vicinity of the substrate and within the CdTe epilayers. HgCdTe epilayers grown on CdTe(211)B/GaAs(211) composite substrate were generally of high quality, despite the presence of precipitates at the HgCdTe/CdTe interface.

The microstructure of HgCdSe thin films grown by MBE on ZnTe/Si(112) and GaSb(112) substrates were investigated. The quality of the HgCdSe growth was dependent on the growth temperature and materials flux, independent of the substrate. The materials grown at 100°C were generally of high quality, while those grown at 140°C had {111}-type stacking defects and high dislocation densities. For epitaxial growth of HgCdSe on GaSb substrates, better preparation of the GaSb buffer layer will be essential in order to ensure that high-quality HgCdSe can be grown.

This thesis is dedicated to my Mom and Dad

for their love and encouragement and their confidence in me.

This Ph.D. would not have been possible without their support.

ACKNOWLEDGMENTS

I would like to thank all people who have helped and inspired me during my doctoral study. I especially want to take this opportunity to express my sincere gratitude to my advisor, Prof. David J. Smith, for his support, guidance, and encouragement. His perpetual energy and enthusiasm in microscopy has greatly impressed and motivated me. His patience and generosity has helped me go through tough times. It is a great honor and an unforgettable experience for me to work in his group.

I am also grateful to Prof. Martha McCartney for her support and advice. I would like to thank Prof. Ray Carpenter, Prof. Michael Treacy, Prof. Peter Bennett for serving on my committee.

I appreciate the collaboration and discussion with Dr. Steve Tobin in BAE systems, Dr. Randy Jacobs in Night Vision and Electronic Sensors Directorate, Dr. Yuanping Chen and Dr. Gregory Brill in U.S. Army Research Laboratory.

I would like to acknowledge Mr. Karl Weiss, Dr. Zhenquan Liu, Mr. Grant Baumgardner and Mr. Gordon Tam for training and helping me to prepare samples and operate electron microscopes.

I would like to thank members of our research group for their help. I especially want to thank Dr. Changzhen Wang for his immense help during my initial training and his encouragement during the tough times. I am very grateful to Dr. Lin Zhou and Dr. David Cullen for their training on analytical electron microscopy, Dr. Suk Chung and Dr. Titus Leo for discussions of TEM lab. I would like to thank Kai, Lu and Luying for their discussions, assistance and

friendship. My best wishes to Allison, Desai, Dinghao, JJ, Lu, Michael, Sahar and Zhaofeng for success in their degree program.

I would like to thank my friends Ni Jiao, Minghui Liu, Xinxin Li, Yanyan Fang and Jingyi Huang for their friendship. I would like to thank Yu Huang, Kewei Sun, Junshi Wang, Qiushi Fu, Zhibin Zhou, Xin Liu, and Xinghui Kongde for being my best basketball buddies.

Finally, I would like to express my most sincere thanks and appreciate towards my parents and grandparents for their continued support and unconditional love throughout years. Without the help of them, I would not have accomplished my goals with so much positive energy and enthusiasm. My appreciation is beyond description.

TABLE OF CONTENTS

Page

CHAPTER Page

CHAPTER Page

LIST OF FIGURES

Figure Page

Figure Page

Figure Page

Chapter 1

INTRODUCTION

Radiation in the electromagnetic spectrum can be classified by wavelength into several bands, including γ-rays, X-rays, ultraviolet, visible light, infrared, microwave and radio waves. Infrared (IR) light is defined as electromagnetic radiation with a wavelength longer than that of visible light, normally measured from the nominal edge of visible red light at 0.74 μm, and extending conventionally to 300 μm. IR detectors are needed to convert IR radiation into some measureable output, normally an electronic signal, thus representing a vital connection to the invisible optical domain. Mercury cadmium telluride (MCT) has long been regarded as the premier material for IR detection purposes.

1. 1 History of HgCdTe

The discovery of HgCdTe in 1958 by the group led by Lawson at the Royal Radar Establishment in England had a major impact on the infrared (IR) detector community, and triggered extensive research on this material.[1] Significant advances in focal-plane array (FPA) technology using HgCdTe have since been made, and it currently represents the dominant material used in all IR spectral bands, primarily for space and military applications.[2]

Much of the original research involving HgCdTe was conducted behind closed doors during the early years of its development, funded by several large defense firms such as Texas Instruments, Hughes Aircraft, and Honeywell.

Mainly through the auspices of the Defense Advanced Projects Research Agency (DARPA), the situation was abruptly changed in 1980, and the first US Workshop on the Physics and Chemistry of HgCdTe was held in 1981.[2]

Over more than 50 years, the ternary HgCdTe alloy has successfully overcome major challenges from alternative materials, such as lead-salt ternary alloys (PbSnTe and PbSnSe), GaAs/AlGaAs quantum-well photodetectors, InSb-based III–V materials, and InAs/GaInSb strained layer superlattices. It has been predicted that, because of its excellent properties, HgCdTe technology will continue to expand the range of its applications well into the future.[3]

1. 2 Material properties of HgCdTe

HgCdTe is a pseudo-binary semiconductor alloy that crystallizes in the zincblende structure. Several properties of HgCdTe qualify it as being highly useful for infrared (IR) detection. These include adjustable bandgap over the 1–30μm range, direct bandgap with high absorption coefficient, and the availability of wide bandgap lattice-matched substrates for epitaxial growth.[4]

1.2.1 Bandgap

$Hg_{1-x}Cd_xTe$ has the unique feature of a direct band gap that is tunable from visible to infrared simply by adjusting the composition x of the alloy. Because of its band gap tunability with x, $Hg_{1-x}Cd_xTe$ has evolved to become the most important material for detector applications over the entire IR range.[5] A number

of expressions approximating the bandgap energy are available.[6] The most widely used expression is due to Hansen *et al.*[7]

$$E_g = -0.302 + 1.93x + 5.35\times10^{-4}(1-2x)T - 0.81x^2 + 0.832x^3 \qquad (1.1)$$

Where E_g is bandgap energy in electron volts, x is cadmium concentration, T is temperature in Kelvin.

The bandgap energy E_g for $Hg_{1-x}Cd_xTe$ versus alloy composition x at temperatures 77 and 300K are shown in Fig. 1.1. As the Cd composition increases, the energy gap for $Hg_{1-x}Cd_xTe$ gradually increases from -0.3eV for HgTe up to 1.6eV for CdTe. Also plotted in Fig. 1.1 is the cutoff wavelength $\lambda_c(x, T)$, defined as the wavelength at which the response has dropped to 50% of its peak value. The bandgap energy tunability results in IR detector applications that span short wavelength IR (SWIR: 1–3 μm), middle wavelength (MWIR: 3–5 μm), long wavelength (LWIR: 8–14 μm) and very long wavelength (VLWIR: 14–30 μm) ranges.[3]

1.2.2 Lattice constant

As shown in Fig. 1.1, the lattice constant of $Hg_{1-x}Cd_xTe$ alloys changes by only 0.02% for x compositions ranging from CdTe to HgTe. This leads to two important consequences for applications: Firstly, HgCdTe can be grown on natural infrared-transparent lattice-matched CdZnTe substrates, thus allowing growth of high-quality HgCdTe epitaxial layers with very low dislocation densities (10^4 cm^{-2}). Secondly, it provides the possibility to grow complex multilayer heterojunctions that are needed for the third generation FPA.[3]

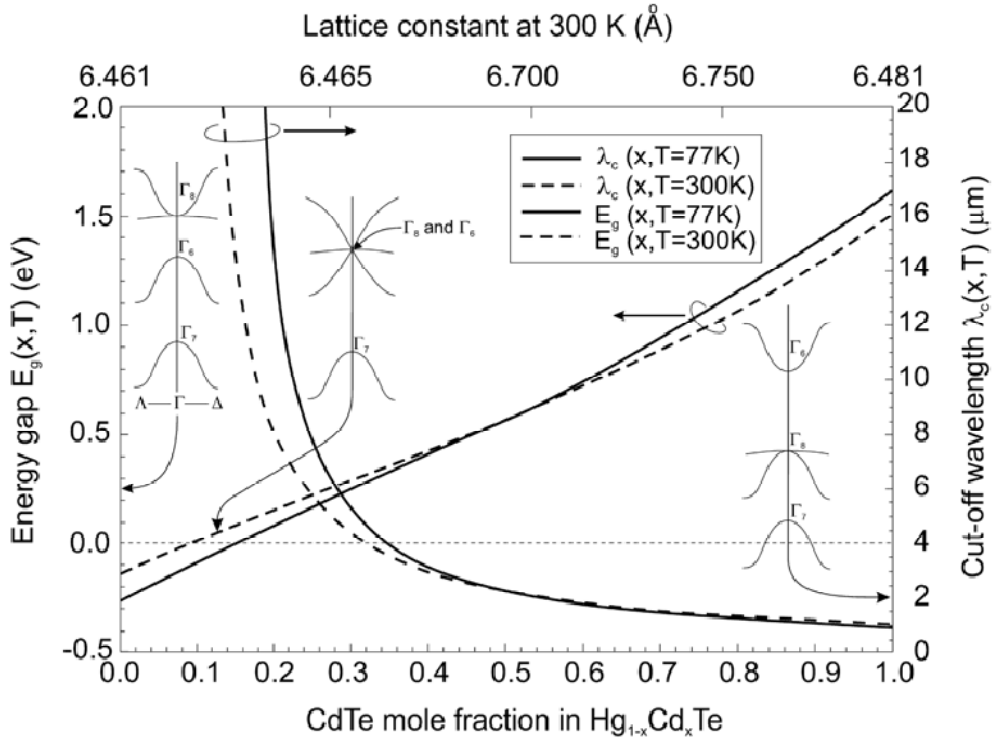

Fig. 1.1. Bandgap structure of HgCdTe near the Γ-point for three different values of the forbidden energy gap.[3]

1.2.3 Optical coefficient

The most important optical parameter for IR detector materials is the absorption coefficient near the band edge, specifically in the region within 20meV from the conduction band edge.[3] Direct bandgap semiconductors, such as HgCdTe, have a sharp onset of the optical absorption as the photon energy increases above E_g. In contrast, indirect semiconductors, such as silicon or germanium, have softer absorption curves.[5] The optical absorption coefficient for HgCdTe has been measured by Scott[8] and is illustrated in Fig. 1.2 over a wide range of alloy compositions. The strong optical absorption allows HgCdTe

detector structures to absorb a very high percentage of the incident signal while being relatively thin, on the order of 10–20 μm. Minimizing the detector thickness leads to minimization of the volume of material which might otherwise generate noise and excess thermal carriers.[3]

In high quality samples, the measured absorption in the short-wavelength region is in good agreement with the Kane model calculation[3], while the situation becomes more complicated in the long-wavelength region because of the appearance of an absorption tail extending to energies lower than the energy gap. This tail has been attributed to composition-induced disorder. According to Finkman and Schacham[9], the absorption tail obeys a modified Urbach's rule:

$$\alpha = \alpha_0 \exp[\frac{\sigma(E - E_0)}{T + T_0}] \text{ in cm}^{-1} \qquad (1.2)$$

Where T is in Kelvin, E is in electron Volts and $\alpha_0 = \exp(53.62x-18.88)$, $E_0 = -0.3424+1.838x+0.148x^2$ (in electron Volts), $T_0 = 81.9$ (in Kelvin), $\sigma = 3.267 \times 104(1+x)$ (in Kelvin per electron Volts) are fitting parameters that vary smoothly with composition. The fitting was performed with data at $x = 0.215$ and $x = 1$ and for temperatures between 80 and 300K.

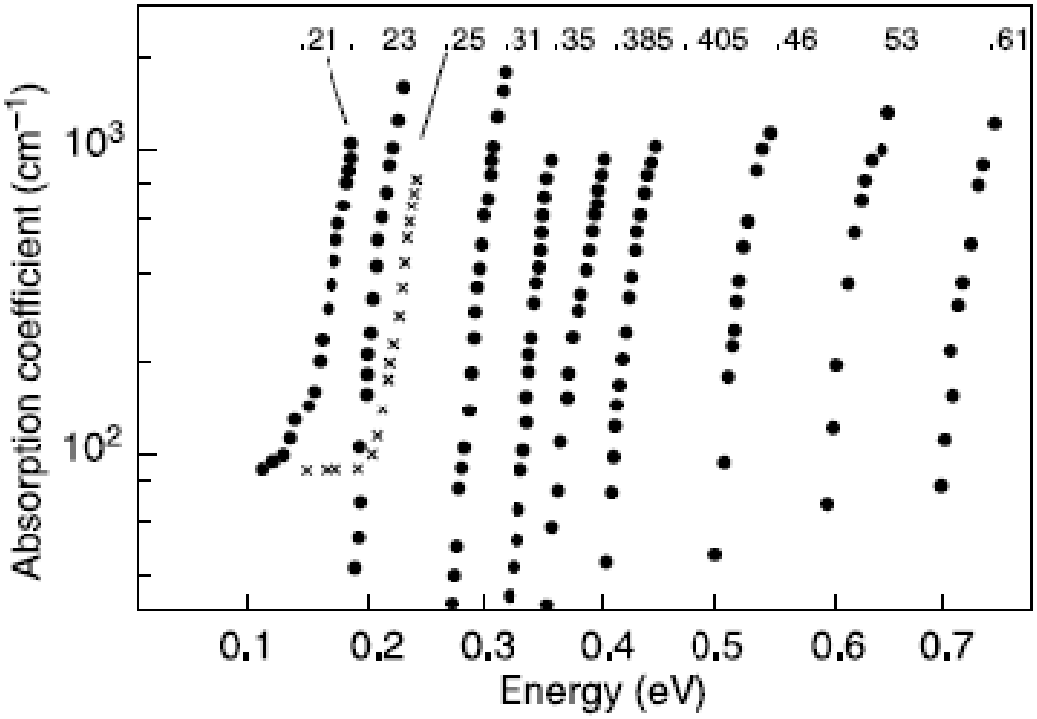

Fig. 1.2. Optical absorption coefficient of $Hg_{1-x}Cd_xTe$ as a function of x.[8]

1.3 Growth of HgCdTe

The growth of HgCdTe has evolved, along with many other semiconductor materials technologies, over the past 50 years. The principal growth methods include bulk growth, liquid-phase epitaxy (LPE), metalorganic chemical vapour deposition (MOCVD), and molecular beam epitaxy (MBE).[5] The timeline for evolution of these growth technologies is illustrated in Fig. 1.3.

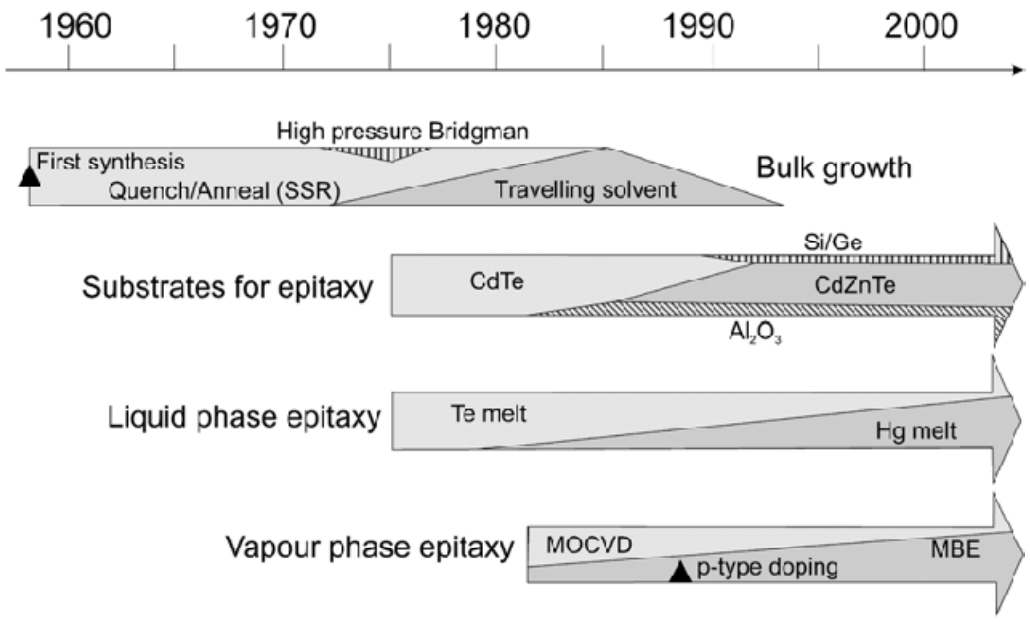

Fig. 1.3. Evolution of HgCdTe crystal growth technology from 1958 to the present.[5]

1.3.1 Bulk methods

Several historical reviews of the development of bulk-grown HgCdTe (MCT) have been published.[4] Kruse and Micklethwaite[10,11] gave comprehensive information on the growth techniques used in the 1960s and 70s. Throughout the 1980s, various viewpoints on the merits and limitations of bulk growth methods were expressed.[4] Electrical properties were seen to be superior to those in epitaxial material while structural properties and available area were seen as the major limitations.[12] Many techniques were tried in the early years but three prime techniques appear to have survived. These are: solid state recrystallization (SSR), Bridgman, and travelling heater method (THM).[4] Tennant *et al.*[13] have provided an authoritative view of the major issues in these growth techniques, and pointed

out the problems of structural defects and size limitations for use in second generation devices.

1.3.2 Liquid-phase epitaxy

The technique of liquid-phase epitaxy (LPE), which had become a well-established method for thin-film growth of III–V compounds since the early 1960s, was not applied to growth of HgCdTe (MCT) until the late 1970s, with the first published paper being by Harman.[14] Since then, the field has grown rapidly to the point that LPE is the most mature method among the various epitaxial techniques. In the early 1990s, bulk growth was replaced by LPE and is now considered very mature for production of first- and second-generation IR detectors. The three main approaches for LPE growth of MCT, namely tipping, dipping and horizontal sliding boat, have all been used for many years for III–V materials.[4] However, LPE technology is limited for the variety of advanced MCT structures required for third generation detectors, due to the poor surface morphology and difficulties in controlling layer thicknesses and interface quality.[5]

1.3.3 Molecular beam epitaxy

Molecular beam epitaxy (MBE) has become one of the leading growth techniques in semiconductor technology for developing new compounds and device structures, based upon its relative simplicity and precise control over growth parameters.[4] The first successful demonstration of epitaxial growth of MCT by MBE was reported in 1981.[15] Since then a great deal of progress has

been achieved in eliminating defects, improving growth and doping control, and demonstrating IR electro-optical devices. At present, MBE is considered as the dominant vapor phase method for the growth of MCT. It offers low temperature growth under ultrahigh-vacuum (UHV) conditions, *in situ* *n*-type and *p*-type doping, and control of composition, doping and interfacial profiles. MBE is now the preferred method for growing complex layer structures for multi-color detectors.[16]

1. 4 Substrates for HgCdTe growth

Epitaxial growth of thin layers of HgCdTe (MCT) for infrared focal-plane array (IR FPA) requires a suitable substrate. CdTe was initially used, since it was available from commercial sources in reasonably large sizes. The main drawback of CdTe is its lattice mismatch of a few per cent with LWIR and MWIR MCT.[5] In the mid-1980s, it was demonstrated that the addition of a few percent of ZnTe to CdTe (typically 4%) could create a lattice-matched substrate.[4] CdTe and closely lattice-matched CdZnTe substrates are typically grown by the modified vertical and horizontal unseeded Bridgman technique.[3]

CdZnTe substrates have severe drawbacks for MCT growth such as the lack of large areas, and high production costs. More importantly, the difference in the thermal expansion coefficients (TEC) in CdZnTe substrates and Si readout integrated circuits (ROIC), as well as recent interest in large-area IR FPAs (1024 × 1024 and 2048 × 2048) have resulted in serious limitations for CdZnTe substrate application. Readily producible CdZnTe substrates are currently limited

to areas of approximately 30 cm^2. At this size, the wafers used for growth are unable to accommodate more than two 1024 × 1024 FPAs.[3]

For more than 30 years, materials researchers have been searching for an alternative substrate to lattice-matched CdZnTe for vapor-phase growth. Numerous materials have been tried, such as sapphire, Ge, Si, GaAs, and InSb, primarily utilizing MBE.[2] Although all these materials have been investigated, Si has clear advantages over the other substrates because of its low cost, large wafer size, and a thermal-expansion coefficient that perfectly matches that of the Si readout circuitry in an FPA structure.[3] In order to accommodate the large lattice mismatch (~19%) between HgCdTe and Si, a CdTe buffer layer is usually deposited by MBE on the Si substrate prior to the growth of HgCdTe.[17] Using optimized growth conditions for Si(211)B substrates, CdTe(211)B layers with EPD of 1.5×10^5 cm^{-2} were obtained.[18] While this level of EPD has little impact on MWIR HgCdTe/Si detectors, it must be reduced still further to achieve high-performance LWIR detectors.

1.5 Surface passivation

The surface passivation of HgCdTe (MCT) has become a major concern due to several critical issues, including the problem of defect formation in the interface region resulting from the nonstoichiometric, contaminated, decomposition (Hg evaporation) or damaged surface prior to or during the passivation process.[19] These defects induce a high density of fixed passivant charges and interface traps, which are usually responsible for the excessive dark

current, low signal, and high noise level found in the photo-detectors.[20] In MBE-grown MCT used for the third generation infrared detectors, surface leakage currents prove to be the performance-limiting factor.[19] Thus, there has been a continuous, ongoing effort to achieve optimal and reliable passivation of MCT surfaces. Thin films of native anodic oxides, such as SiO_2, ZnS, and CdTe, have been extensively investigated as passivants for MCT.[21] Among these options, CdTe has become one of the major choices in the IR industry, due to its excellent material properties as a passivant for MCT junctions, including its chemical compatibility to MCT, good adhesion, and larger bandgap energy.[22]

1.6 Detection Mechanism of HgCdTe Photodiodes

1.6.1 Photodiodes

A photodiode is a type of photodetector capable of converting light into either current or voltage, depending upon the mode of operation. The most common example of a photovoltaic detector is the abrupt *p*-*n* junction prepared in the semiconductor, which is often referred to simply as a photodiode. The principle of operation of the *p*-*n* junction photodiode is illustrated in Fig. 1.4. When a photon of sufficient energy strikes the diode, it excites an electron, thereby creating a mobile electron and a positively charged electron hole. If the absorption occurs in the depletion region of the junction, or one diffusion length away from it, these carriers are swept from the junction by the built-in field of the depletion region. Holes thus move toward the anode, and electrons toward the

cathode, and a photocurrent is produced, which shifts the current-voltage (*I*-*V*) characteristic in the direction of negative or reverse current.[3]

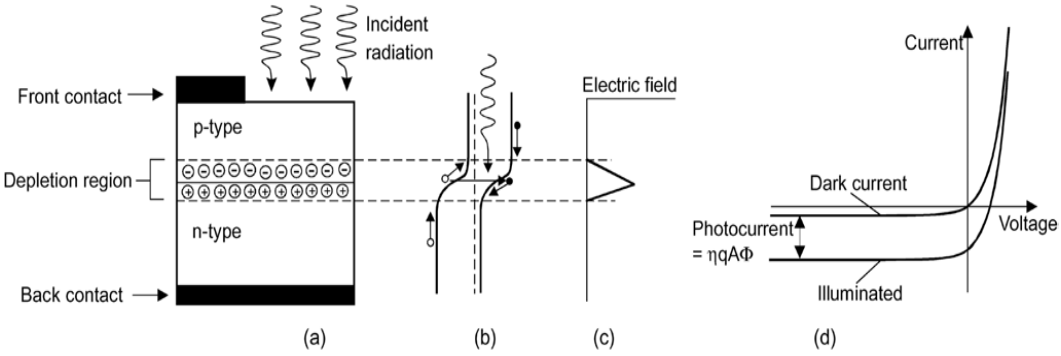

Fig. 1.4. *p*–*n* junction photodiode: (a) structure of abrupt junction, (b) energy band diagram, (c) electric field and (d) *I*–*V* characteristics.[3]

An example of a HgCdTe photodiode is shown in Fig. 1.5. An *n*-type layer of HgCdTe is grown on a CdZnTe substrate, followed by a *p*+-layer to form the junction. Mesa etching defines the individual diodes. The surface is passivated to prevent surface accumulation or inversion. Contacts are made to the *p*+-layer in each pixel and to the *n*-type layer at the edge of the array. Infrared flux is incident through the IR-transparent substrate.[5]

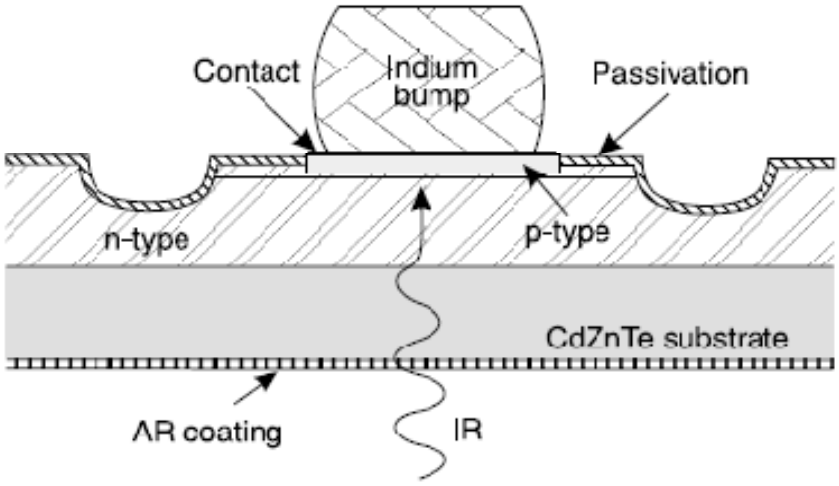

Fig. 1.5. Cross section of a mesa-etched HgCdTe photodiode.[5]

1.6.2 Readout Multiplexers

Once the incident photon energy becomes an electrically measurable charge, the charge must be collected and registered. This function occurs in the multiplexing readout circuitry. This multiplexing has several advantages over reading out every detector independently. These include reduced power consumption, fewer amplifiers and lines from the cold finger to the outside warm world, and independent optimization of detector materials and multiplexer. Indium bump bonding of readout electronics provides for multiplexing of the signals from thousands of pixels onto a few output lines, greatly simplifying the interface between the vacuum-enclosed cryogenic sensor and the system electronics.[3] These multiplexers may be a separate integrated circuit connected to the array as a hybrid, as illustrated in Fig. 1.6.

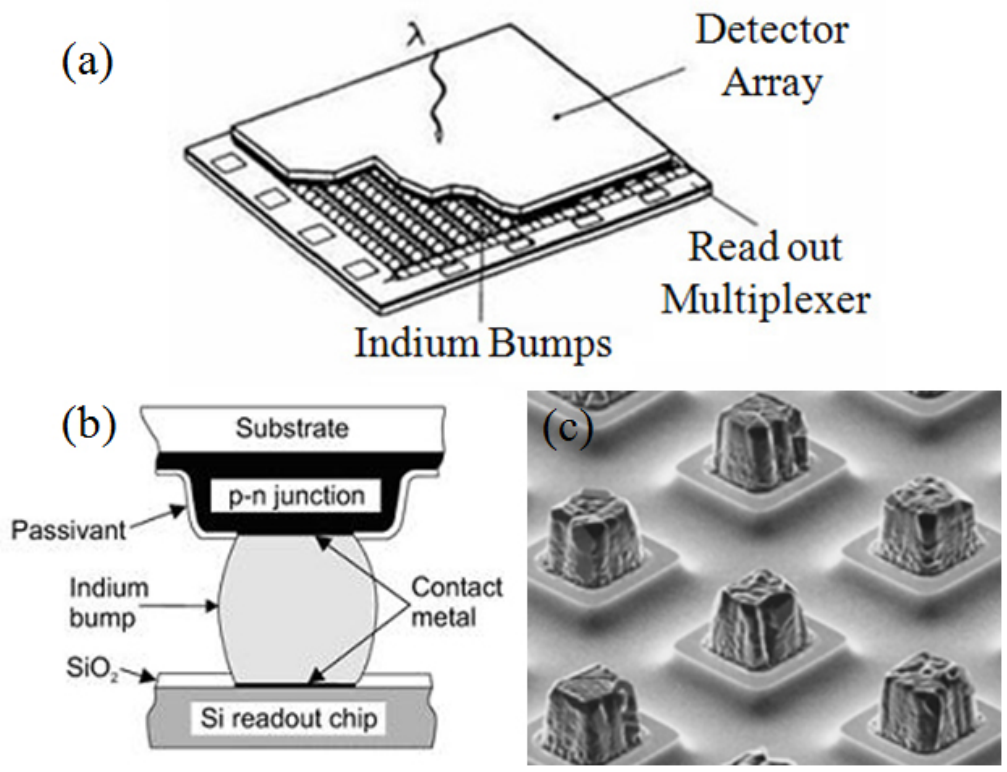

Fig. 1.6. (a) Hybrid IR FPA, (b) cross section of structure, (c) indium bumps on Si multiplexer.[3]

1.7 Third generation detectors

The US Army is principally interested in developing third generation IR systems in order to extend both detection and identification ranges significantly beyond the capability of current systems.[23] The definition of third generation IR systems is not particularly well established. According to Reago *et al.*[24], the third generation is defined in order to maintain the current advantage enjoyed by US and allied armed forces. This class of devices includes both cooled and uncooled FPAs[24, 25]

(1) High-performance, high-resolution cooled imagers having multi-colour

bands,

(2) medium- to high-performance uncooled imagers,

(3) very low cost expendable uncooled imagers.

1.7.1 Two-color HgCdTe detectors

Considerable progress in the development of multi-color HgCdTe FPAs has been recently demonstrated by many research groups, usually by employing MBE for the growth of a variety of devices.[3]

The unit cell of two-color integrated FPAs consists of two detectors, each sensitive to a different spectral band. The first demonstrated two-color HgCdTe detector, as shown in Fig. 1.7, is the bias-selectable *n-p-n* triple-layer heterojunction (TLHJ), back-to-back photodiode. A critical step in device formation is connected with the *in situ p*-type As-doped layer with good structural and electrical properties to prevent internal gain from generating spectral crosstalk. The Band 1 and Band 2 alloy compositions can be any two *x*-values as long as Band 1 has a higher *x*-value than Band 2. The polarity of the bias across the structure determines which junction is active, and thereby the spectral band of the detector. The bias switching is performed by the readout integrated circuit (ROIC).[3]

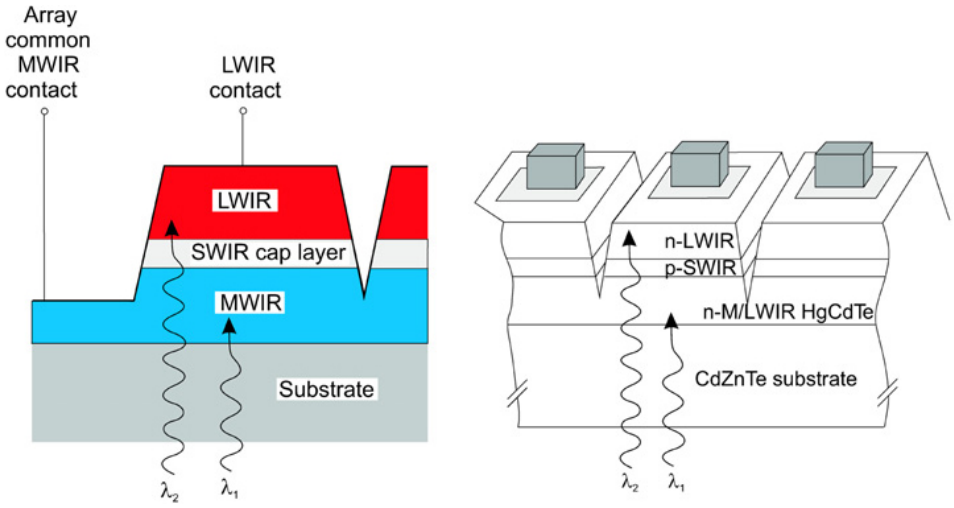

Fig. 1.7. Cross section of two-color *n-p-n* detector structure.[3]

1.7.2 Alternative materials systems

Much effort has been expended to push the HgCdTe technology to both large-format and low-cost systems while still maintaining superior performance.[26] However, even with all the advances made in this technology, HgCdTe still faces a challenge that to date has not been overcome, namely that the dislocation density of HgCdTe grown on scalable substrates is two orders of magnitude higher than state-of-the-art HgCdTe material grown on nonscalable CdZnTe.[27] A number of alternative materials technologies to HgCdTe have emerged over the years, but most have since fallen by the wayside.

In the early 1990s, quantum-well IR photodetectors (QWIPs) were thought to be a competitive technology, but their time seems to have come and gone due to fundamental limitations associated with intersubband transitions at higher temperature operation (>70K) and relatively low quantum efficiencies (typically less than 10%).[2]

The world of bandgap engineering is currently enamored with type-II superlattices (T2SLs) (InAs-GaSb and related alloys) for both the MWIR and LWIR regions. The laws of physics are favorable for T2SLs, predicting good quantum efficiencies. By adjusting the strain in the superlattice, the Auger process can be suppressed. Additionally, the larger effective mass in the SLS material reduces tunneling currents in the space charge region. T2SL-based detectors have seen rapid progress over the past few years.[2] However, the merits of this material system rest on yet-to-be experimentally verified predictions of higher performance and engineering advantages. Whether the superlattice IR photodetectors can outperform the ‘‘bulk’’ narrow-gap HgCdTe detectors is one of the most important questions for the future of IR photodetectors.[26]

Among the possible small gap II-VI semiconductor alloys for IR detectors, HgZnTe, HgMnTe, and HgCdSe can be considered as alternatives to HgCdTe. However, none of these ternary alloy systems has been systematically explored in the device context.[3] Recently, it was proposed that HgCdSe might replace HgCdTe for IR applications due to its advantage of having commercially available large-area substrates readily available.[27] The lattice constant and bandgap of various semiconductor systems are shown in Fig. 1.8.

Analogous to the alloying of HgTe and CdTe, HgSe and CdSe crystallize in the zincblende structure to form an alloy of $Hg_{1-x}Cd_xSe$. The bandgap of this material can be tuned simply by adjusting the x composition to absorb any wavelength of IR light, similar to $Hg_{1-x}Cd_xTe$. In addition, two commercially available III-V binary semiconductors, namely InAs and GaSb, can be used as

large-area substrates that are nearly lattice-matched to HgCdSe. With the small lattice mismatch present between these substrates and HgCdSe, it seems reasonable to assume that the final HgCdSe dislocation density could be similar to the dislocation densities for HgCdTe materials grown on bulk CdZnTe substrates.[27]

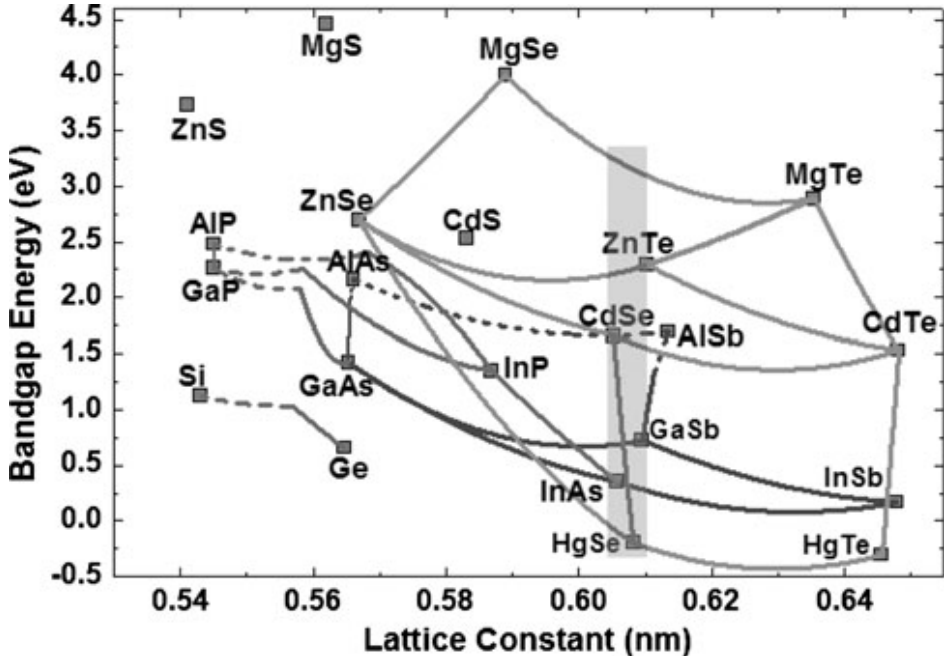

Fig. 1.8. Energy gap versus lattice parameter for several semiconductor material systems. The shaded region highlights semiconductors that have lattice parameters near 6.1Å.[27]

1.8 Outline of dissertation

In this dissertation, microstructural characterization of LPE- and MBE-grown HgCdTe alloys and related materials is undertaken. Transmission electron

microscopy (TEM) imaging and small-probe microanalysis have been used throughout to characterize the materials in order to improve the growth process.

In chapter two, the details of experimental procedures involved in this dissertation are summarized. Materials growth methods, including LPE and MBE, are briefly described. Sample preparation methods essential for TEM characterization, including ion milling and FIB milling, are explained in detail.

In chapter three, the microstructure of CdTe surface passivation layers deposited on HgCdTe heterostructures is described and discussed. The growth of CdTe layers by different techniques and processing methods is compared, using TEM imaging and analytical techniques. TEM sample preparation by FIB milling is demonstrated.

In chapter four, microstructural characterization of HgCdTe layers grown by MBE on both Si(211) and GaAs(211) substrates is described. The nucleation of ZnTe layers on stepped Si(211) surfaces, and the microstructure of the composite HgCdTe/CdTe(211)B/ZnTe/Si(211) material are characterized using a wide range of TEM imaging and analytical techniques. The microstructure of the CdTe(211)B/GaAs(211) heterostructure is also characterized using TEM.

In chapter five, microstructural characterization of HgCdSe layers grown by MBE on GaSb(112) and ZnTe/Si(112) substrates is reported. These results include some of the first ever electron micrographs of HgCdSe material grown on GaSb substrates. Samples of HgCdSe were grown at different temperatures and flux ratios in order to determine the optimal growth parameters, and the

microstructure of the composite HgCdSe/ZnTe/Si(112) and HgCdSe/GaSb(112) materials are characterized by TEM methods.

In chapter six, conclusions and opportunities for future work are presented. Proposals and comments for further improvement of TEM sample preparation are also given.

REFERENCES

[1] W.D. Lawson, S. Nielson, E.H. Putley, and A.S. Young, J. Phys. Chem. Solids **9**, 325 (1959).

[2] M.A. Kinch, J. Electron. Mater. **39**, 1043 (2010).

[3] A. Rogalski, Rep. Prog. Phys. **68**, 2267 (2005).

[4] P. Capper, Properties of Narrow Gap Cadmium-based Compounds (EMIS Datareviews Series No. 10) (1994).

[5] P. Norton, Opto-Electron. Rev. **10**, 159 (2002).

[6] G.L. Hansen, J.L. Schmit, and T.N. Casselman, J. Appl. Phys. **53**, 7099 (1982).

[7] G.L. Hansen, and J.L. Schmit, J. Appl. Phys. **54**, 1639 (1983).

[8] M.W. Scott, J. Appl. Phys. **1**, 239 (1962).

[9] E. Finkman, and S.E. Schacham, J. Appl. Phys. **56**, 2896 (1984).

[10] P.W. Kruse, Semicond. Semimet. **18**, 1 (1981).

[11] W.F.H. Micklethwaite, Semicond. Semimet. **18**, 47, (1981).

[12] A.W. Vere, Proc. SPIE **659**, 10 (1986).

[13] W.E. Tennant, C.A. Cockrum, J.B. Gilpin, M.A. Kinch, M.B. Reine, and R.P. Ruth, J. Vac. Sci. Technol. **B 10**, 1359 (1992).

[14] T.C. Harman, J. Electron. Mater. **8**, 191 (1979).

[15] J.P. Faurie, and A. Million, J. Cryst. Growth **54**, 582 (1981).

[16] M. Reddy, J.M. Peterson, D.D. Lofgreen, J.A. Franklin, T. Vang, E.P.G. Smith, J.G.A. Wehner, I. Kasai, J.W. Bangs, and S.M. Johnson, J. Electron. Mater. **37**, 1274 (2008).

[17] T.D. Golding, O.W. Holland, M.J. Kim, J.H. Dinan, L.A. Almeida, J.M. Arias, J. Bajaj, H. D. Shih, and W. P. Kirk, J. Electron. Mater. **32**, 882 (2003).

[18] S. Rujirawat, L.A. Almeida, Y.P. Chen, S. Sivananthan, D.J. Smith, Appl. Phys. Lett. **71**, 1810 (1997).

[19] V. Kumar, R. Pal, P.K. Chaudhury, B.L. Sharma, and V. Gopal, J. Electron. Mater. **34**, 1225 (2005).

[20] O.P. Agnihotri, C.A. Musca, and L. Faraone, Semicond. Sci. Technol. **13**, 839 (1998).

[21] R.R. Singh, D. Kaushik, M. Sharma, D. Kumar, and R.K. Pandey, Semicond. Sci. Technol. **23**, 1 (2008).

[22] S.Y. An, J.S. Kim, D.W. Seo, and S.H. Suh, J. Electron. Mater. **31**, 683 (2002).

[23] S. Horn, P. Norton, T. Cincotta, A.J. Stoltz, Jr., J.D. Benson, P. Perconti, J. Campbell, Proc. SPIE **5074**, 44 (2003).

[24] D. Reago, S. Horn, and R. Vollmerhausen, Proc. SPIE **3701**, 108 (1999).

[25] P. Norton, J. Campbell, S. Horn, and D. Reago, Proc. SPIE **4130**, 226 (2000).

[26] A. Rogalski, Infrared Phys. Technol. **50**, 240 (2007).

[27] G. Brill, Y. Chen, and P. Wijewarnasuriya, J. Electron. Mater. **40**, 1679 (2011).

Chapter 2

EXPERIMENTAL PROCEDURES

This chapter first outlines the methods used for materials growth, including liquid-phase epitaxy (LPE) and molecular beam epitaxy (MBE). Sample preparation methods, including ion milling and focused-ion-beam milling, suitable for electron microscopy examination of HgCdTe/CdZnTe and HgCdTe/CdTe/Si heterostructures are then described in detail. A method of etching for minimizing ion-milling damage is introduced. High resolution transmission electron microscopy (HREM), scanning transmission electron microscopy (STEM) and analytical electron microscopy (AEM), which are heavily used in the experimental studies described in the later chapters, are also briefly summarized.

2.1 Material growth

2.1.1 LPE growth of HgCdTe *p*-*n* heterojunction

The *p*-on-*n* $Hg_{1-x}Cd_xTe$ heterojunction device structures were grown by LPE on nominally lattice-matched CdZnTe(111)B substrates by Dr. S. Tobin and colleagues at BAE Systems. The *x* concentration was determined by carefully weighing the constituents then transferring the materials to the LPE "boat". The boat was then heated in the furnace to several hundred degrees Celsius until a liquid phase was reached, after which it was slowly cooled.[1] The In-doped *n*-type absorber layers were first grown in a horizontal slider system using a Te-rich melt.

The As-doped *p*-type cap layers, usually with higher *x* concentration corresponding to higher bandgap material, were grown in a vertical dipper system from an Hg-rich melt. Individual devices were defined by wet-chemical mesa-etching and then passivated with ultrahigh-vacuum-deposited CdTe. Some wafers were annealed in Hg atmosphere at 250°C for 96h to reduce the Hg vacancy concentration and to cause interdiffusion between the CdTe passivation layer and the HgCdTe surface region.

2.1.2 MBE growth of CdTe and $Hg_{1-x}Cd_xSe$ materials

Samples of CdTe(211)B/ZnTe/Si(211), $Hg_{1-x}Cd_xSe$/ZnTe/Si(112) and $Hg_{1-x}Cd_xSe$/GaSb(112) heterostructures were grown by MBE in Army Research Laboratory. Samples of HgCdTe/CdTe(211)B/GaAs(211) were grown by MBE in U.S. Army RDECOM, CERDEC Night Vision and Electronic Sensors Directorate. Figure 2.1 shows a schematic of a typical MBE growth chamber. The substrate was held in the MBE chamber in direct line of the shuttered effusion cells. The effusion cells were used to heat the ultra-pure materials, which slowly sublimated and then condensed on the wafer. During operation, reflection-high-energy electron diffraction (RHEED) was normally used to monitor growth of the crystal layers. Computer-controlled shutters were located in front of each effusion cell, allowing precise control of the layer thicknesses down to a single atomic layer. The growth temperatures were usually less than 200˚C, which was approximately 150˚C below typical growth temperatures used for metalorganic chemical vapor

deposition (MOCVD). Hg, solid CdTe, Te, and Se were used as the source materials.

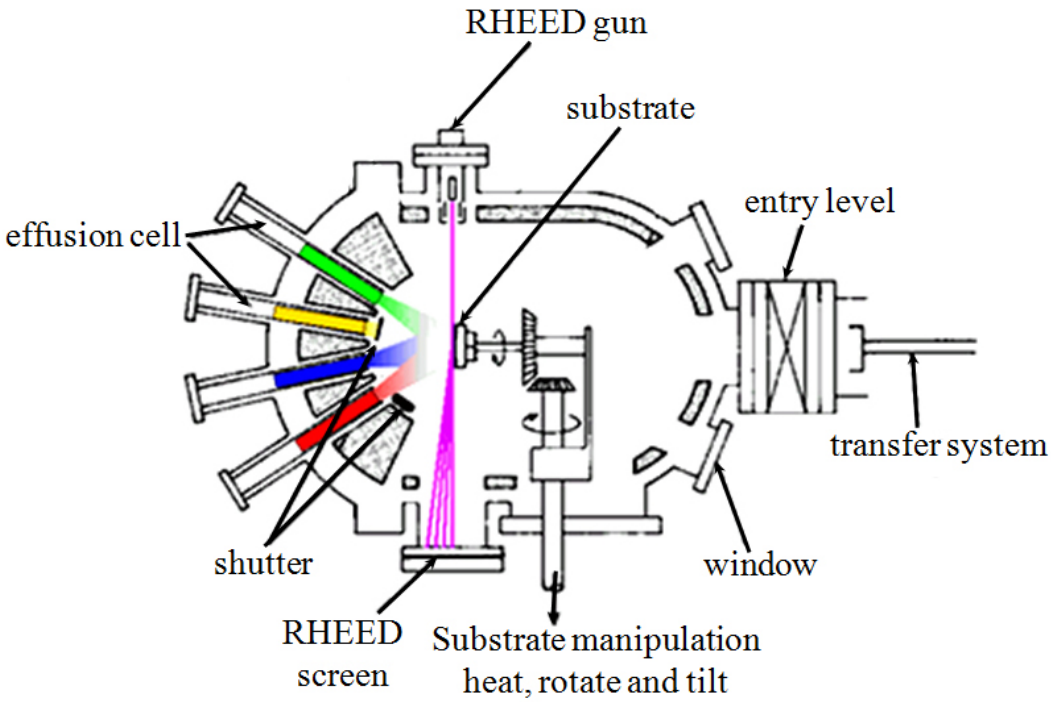

Fig. 2.1. Schematic of an MBE system.[2]

2.2 TEM sample preparation

Samples suitable for TEM examination were prepared in the cross-sectional geometry using standard mechanical polishing and dimpling, followed by argon-ion milling. However, the Hg-containing material studied in this dissertation research had to be treated very carefully in order to obtain suitable electron-transparent thin foils due to: mechanical weakness of the substrate; poor adhesion between the film and the substrate; and inherent susceptibility to ion-milling

damage. In this section, the special procedures developed for TEM sample preparation in this research are described.

2.2.1 HgCdTe/CdZnTe heterostructures

Since the CdZnTe substrates were extremely weak and brittle, diamond blades, which are commonly used to slice Si wafers, could not be used at any time. Otherwise, sample vibration would easily initiate crack formation, leading to the propagation of cracks through the entire wafer. Samples were instead cleaved into pieces about 3 mm in width. Two pieces were then glued with film layers face-to-face in the case of cross-sectional samples. The samples had to be gently pressed with a sample clamp to remove excess glue between the two pieces. The samples were then placed into an oven for curing for about 30 minutes. The oven temperature had to be maintained at a temperature of no more than 90°C throughout the entire preparation process because higher temperature would cause Hg diffusion and cause the original structures to be altered.

After sample curing, standard mechanical polishing and dimpling were used for further thinning. The first side of the cross-sectional sample was gently ground down by a few millimeters depending on the initial sample thickness, followed by polishing with diamond lapping paper until most visible scratches around the target area of interest were removed. The sample was then flipped over, and the second side was ground down to a total thickness of ~100-120 μm, followed by dimpling with a cloth wheel. Since the material removal rate was extremely high, the samples were regularly checked under an optical microscope about every 2

minutes. The dimpling was usually stopped at a sample thickness of about 30μm, which was much thicker relative to other materials, due to the brittleness of the CdZnTe substrate.

The sample was then glued onto a copper grid since the sample was still on a glass stub. After curing in a low temperature oven (90°C), the sample would be placed in fresh acetone for about an hour to remove the glass stub from the sample. The sample was finally argon-ion-milled at 3.5keV at liquid nitrogen temperature using Gatan Model 691 PIPS system until hole perforation was achieved.[2] Low-angle, low-energy (approximately 2.0keV) milling was used for final thinning to minimize the formation of any amorphous surface or interfacial layers. All of the major steps in this procedure are illustrated in Fig 2.2.

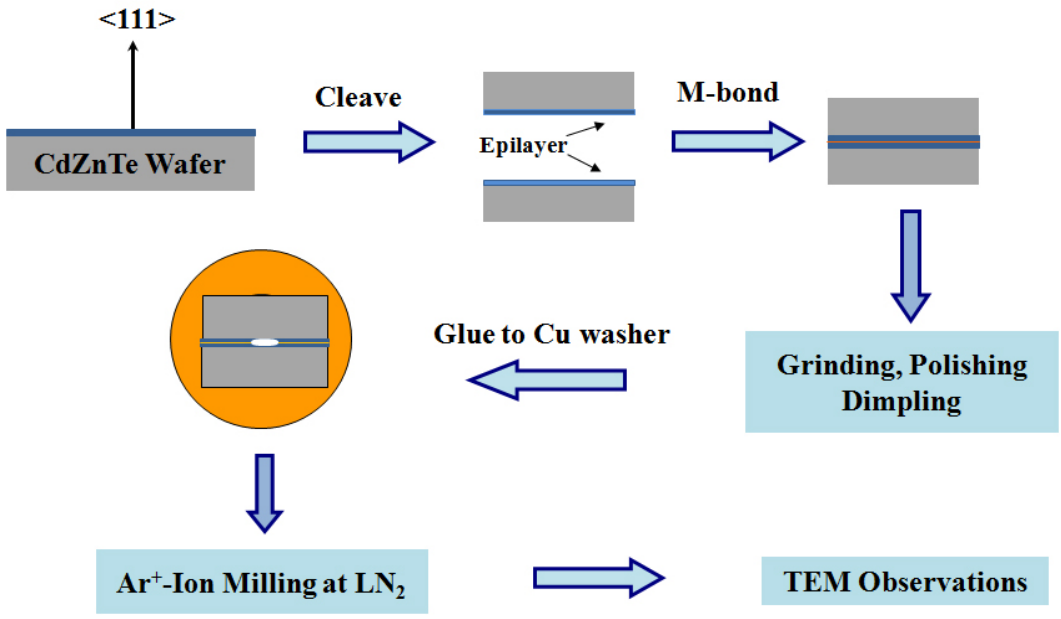

Figure 2.2. Schematic showing procedures used for TEM sample preparation.

2.2.2 HgCdTe/CdTe/Si heterostructures

The two major problems experienced when preparing TEM samples for this system were film adhesion to the substrate, and differences in the rate of material removal during ion milling.

Because Si substrates of the HgCdTe/CdTe/Si heterostructures had sufficient mechanical strength, they could usually be cut into small pieces to prepare cross-sectional samples. Samples were cut into slabs with sizes of about 2.5 mm$\times$2 mm, followed by gluing two pieces together for preparation of the cross-sectional samples. The first side was then mechanically ground by a few millimeters depending on the initial sample thickness, followed by polishing with diamond lapping paper until most visible scratches around the target area were again removed. The second side was mechanically ground to a thickness of ~100-120 μm, followed by dimpling with copper wheel to about 30 μm. Since the removal rate of CdTe in this polishing procedure was much greater than for Si, the sample was then dimpled off-center using a cloth wheel, which made the Si substrate thinner than the film layer. This “off-center dimpling” method allowed large thin areas of the CdTe/Si interface suitable for TEM observation to be obtained. Cloth-wheel dimpling was usually stopped when the hole being formed from the substrate side approached close to the film/substrate interface.

The sample was then glued onto a copper grid as it was still mounted on a glass stub. After curing in a low temperature oven at 90°C, the sample was placed in fresh acetone to remove the glass stub from the sample. Finally, the sample would be argon-ion-milled at 2.5keV at liquid nitrogen temperature until hole

perforation occurred. Low-angle, low-energy (approximately 2.0keV) milling was again used for final thinning to minimize the formation of any amorphous surface or interfacial layers. These procedures have summarized schematically in Fig. 2.3. Since the CdTe layers were etched away much faster than the Si substrate, the period of ion-milling had to be kept short. Otherwise, the entire CdTe layer would be gone.

The same off-center procedure was also applied to sample preparation for HgCdSe/ZnTe(112)/Si, HgCdSe/GaSb(112), and CdTe(211)B/GaAs(211) heterostructures.

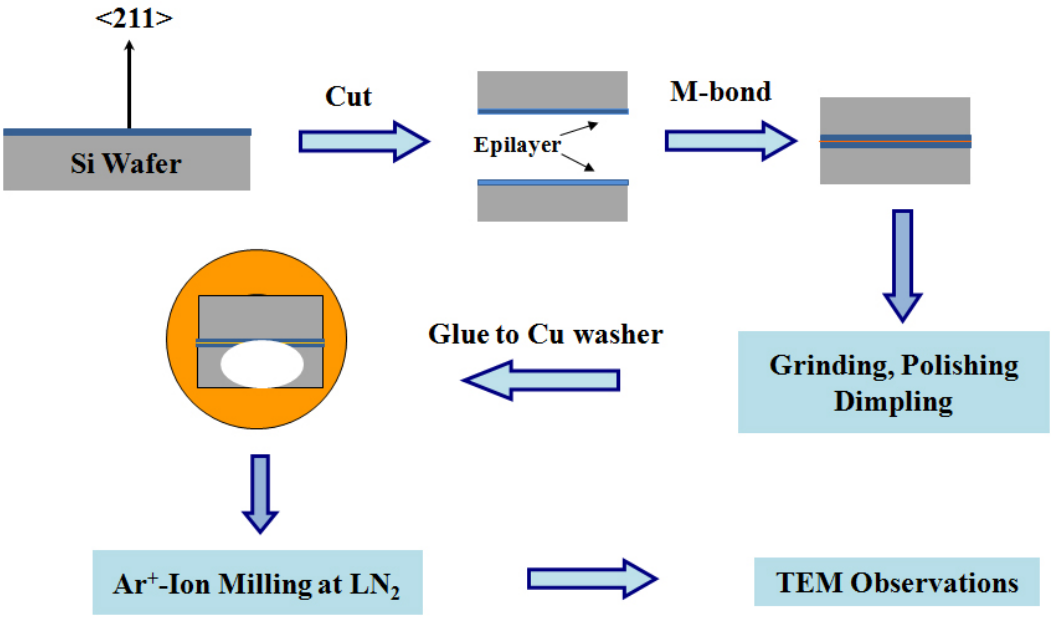

Fig. 2.3. Schematic showing procedures used for TEM sample preparation.

2.2.3 Focused ion beam

TEM cross-sectional samples were also prepared using an FEI Nova 200 focused-ion-beam (FIB) system. The FIB technique has a major advantage over conventional methods of TEM specimen preparation in that samples can be extracted from specific sites, and large uniform thin areas can be obtained. However, since HgCdTe samples are known to be susceptible to ion-milling damage, precautions must still be taken to minimize FIB damage. A platinum protection layer was first deposited over the area of interest to protect the film, as illustrated in Fig. 2.4 (a). Low-energy low-current milling was used during the final stages of milling to minimize ion damage. Figure 2.4 (b) shows that no major structural changes in the HgCdTe layer appears to have been caused as a result of the FIB milling, although the CdTe layer has clearly been badly damaged.

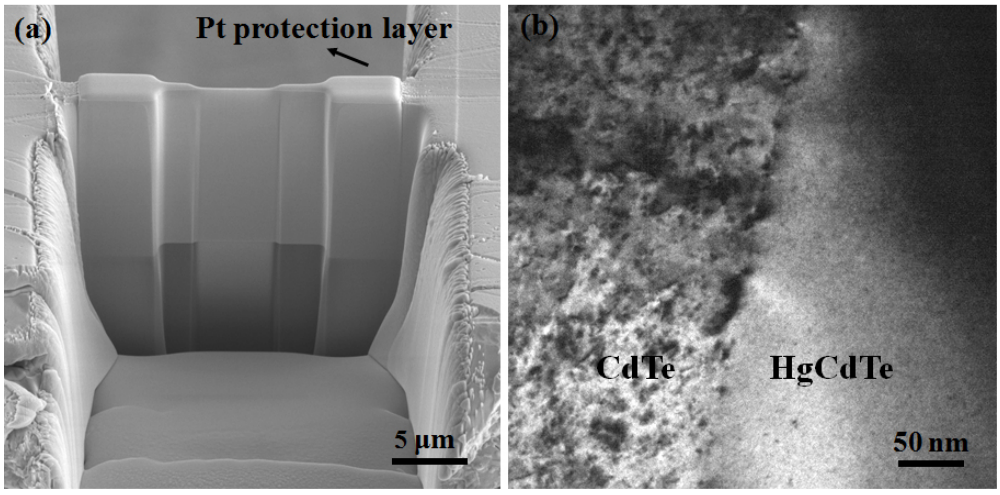

Fig. 2.4. (a) Scanning electron micrograph showing the Pt protection layer and the HgCdTe/CdTe/Si heterostructure; (b) Cross-section electron micrograph of sample prepared using the FIB system.

2.2.4 Ion-milling damage

Ion-milling damage during TEM sample preparation has been a serious ongoing issue for II-VI materials for many years.[3-5] During this research, it was consistently observed that argon-ion milling had induced severe damage in CdTe material, even when the sample was milled at very low energy and held properly at liquid nitrogen temperature. Typical high-resolution images taken at two different magnifications are presented in Fig. 2.5 (a) and (c). It is evident that the defects primarily consist of small (about 5-10 nm) dislocation loops, which lie mostly on {111} planes. In order to eliminate this ion-milling damage, methanol solutions of dilute bromine (0.01% volume concentration) were used to etch the samples for 10 seconds after ion milling. The loop defects observed previously were essentially eliminated after etching, as demonstrated in Fig. 2.5 (b). Several dislocations that thread through the layer, as well as defects near the interface, are visible, but relatively few of the dislocation loops can be seen. The high-resolution image in Fig. 2.4 (d) shows that no stacking faults are present and only a perfect lattice image is visible. However, it must be stated that a consistent and reliable method of etching for preparation has not yet been established since the thin areas quickly become thick and dirty after etching.

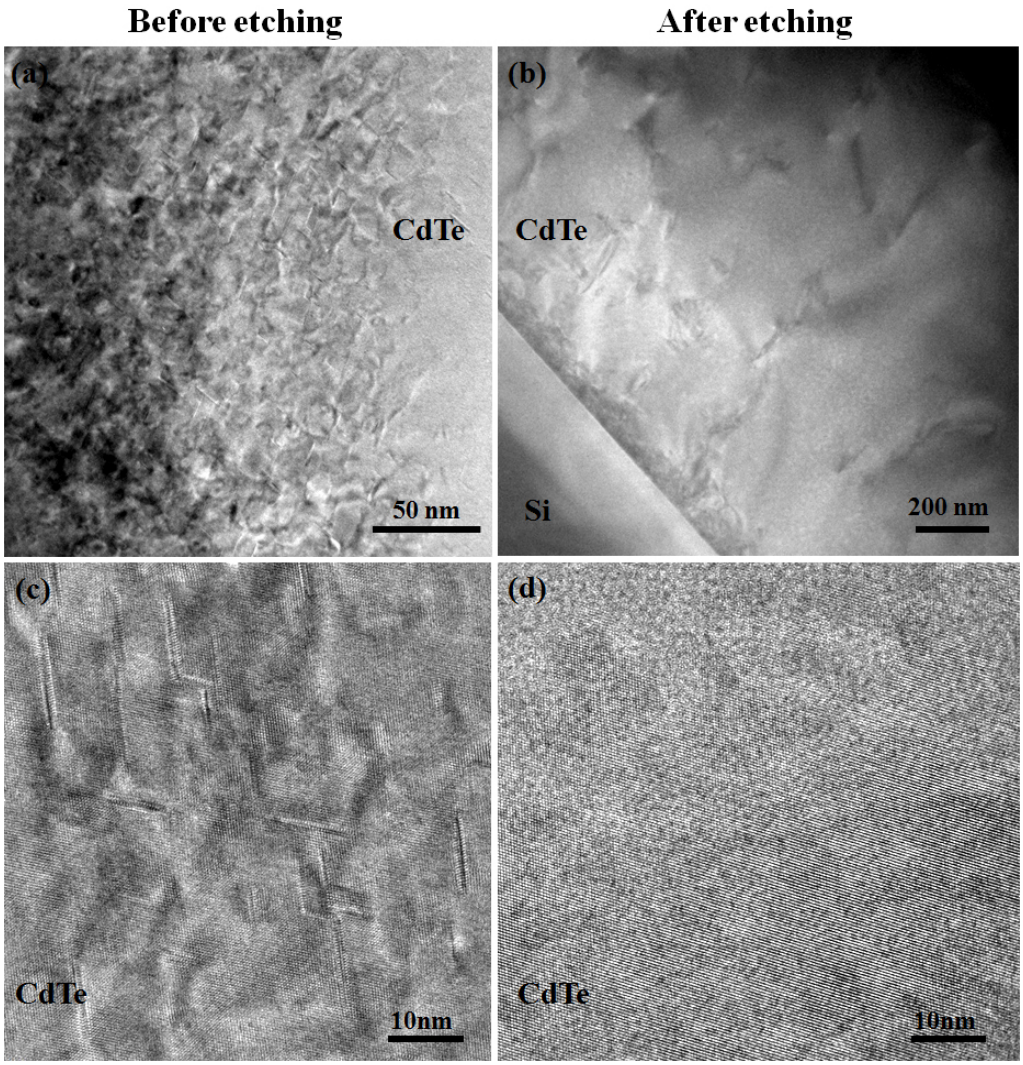

Fig. 2.5. Cross-section electron micrograph of CdTe samples prepared by argon ion milling: (a),(c) before etching; (b),(d) after etching.

2.3 Electron microscopy

2.3.1 High resolution transmission electron microscopy (HREM)

The electron microscopy observations reported in this dissertation were mostly carried out using a JEOL JEM-4000EX high-resolution electron microscope, operated at 400keV, and equipped with a double-tilt, top-entry-type

sample holder. The top-entry-type sample holder provides high stability against sample drift, which is essential for high resolution. All of the high-resolution images were taken under similar microscope operating conditions and the microscope was always corrected for objective-lens astigmatism and axial coma before final image recording took place. Both phase-contrast and diffraction – contrast imaging were used to characterize the thin-film samples.

2.3.2 Scanning transmission electron microscopy (STEM)

High-angle annular-dark-field (HAADF) imaging and energy-dispersive x-ray spectroscopy (EDXS) were carried out using a JEOL 2010F TEM, equipped with a field-emission electron gun and operated at 200keV.

A schematic illustrating the essential components essential for the STEM technique is shown in Fig. 2.6. The image-forming objective lens precedes the specimen, and is used to form a small probe which is scanned across the specimen in serial mode. In state-of the-art instruments, this probe can have Ångstrom-scale dimensions. The focused beam passes through the sample and is then scattered in all directions. The transmitted beam can be used to form bright-field images, which resemble the normal high-resolution TEM images, or pass through spectrometers from which energy-filtered images and/or the electron-energy-loss spectrum (EELS) can be obtained. X-rays are also produced due to inelastic scattering of electrons by the sample, allowing the technique of energy-dispersive X-ray spectroscopy (EDXS) to be used for element identification. The electrons that are scattered to relatively high angles are collected by an annular-dark-field

(ADF) detector. Images that result from collection of the scattered electrons reaching the high-angle annular detector give bright contrast roughly corresponding to the mean square of the atomic number. Thus, this type of high-angle annular-dark-field (HAADF) imaging is usually referred to as "Z-contrast" imaging.[6-8] A major strength of HAADF imaging is that it gives an image free of contrast reversal over a large range of thicknesses and defocus, thereby overcoming the image-interpretation problems in HREM imaging caused by dynamical diffraction.[8-10] The spatial resolution is limited by the probe size of the microscope (the optimization of which is achieved using the Ronchigram). In this research, HAADF images were obtained by using a focused probe diameter of ~0.2 nm.

2.3.3 Analytical Electron Microscopy

EDXS was performed to analyze the composition distributions, usually across sample interfaces. The electron beam incident on a sample excites electron from inner shells, leaving vacancies in the original shell location. Electrons from outer, higher-energy shells then fill the holes, together with emission of X-rays. The corresponding energies of the emitted X-rays carry characteristic information about the chemical species present in the specimen. The spatial resolution of the EDXS signal is mainly determined by the probe size and the interaction volume within the sample. In this research, elemental composition profiles were obtained by operating the microscope in STEM mode with the probe size of ~1 nm and scanning the electron probe across the region of interest.

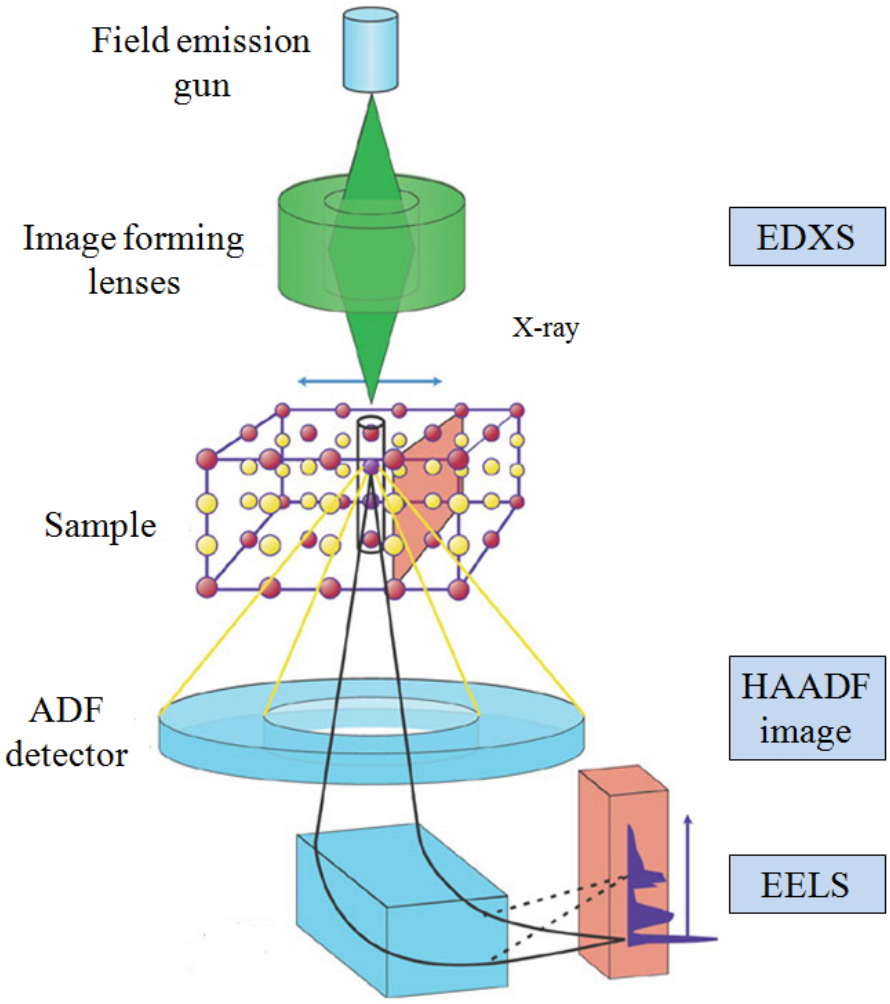

Fig. 2.6. Schematic showing the essential components associated with the scanning transmission electron microscopy technique.[11]

REFERENCES

[1] P. Capper, Properties of Narrow Gap Cadmium-based Compounds (EMIS Datareviews Series No. 10) (1994)

[2] M.A. Herman and H. Sitter, Molecular Beam Epitaxy: Fundamentals and Current Status (Springer Series in Materials Science), 1989.

[3] C. Wang, D.J. Smith, S. Tobin, T. Parodos, J. Zhao, Y. Chang and S. Sivananthan, J. Vac. Sci. Technol. A **24**, 995 (2006).

[4] A.G. Cullis, N.G. Chew and J.L. Hutchison, Ultramicroscopy **17**, 203 (1985).

[5] T. Aoki, Y. Chang, G. Badano, J. Zhao, C. Grein, S. Sivananthan, D.J. Smith, J. Cryst. Growth **265**, 224 (2004).

[6] J. Wall, J. Langmore, M. Isaacson and A.V. Crewe, Proc. Natl Acad. Sci. **71**, 1 (1974).

[7] A. Howie, J. Microsc. **17**, 11 (1979).

[8] E.J. Kirkland, R.F. Loane and J. Silcox, Ultramicroscopy **23**, 77 (1987).

[9] J. Fertig and H. Rose, Optik **59**, 407 (1981).

[10] R.F. Loane, E.J. Kirkland and J. Silcox, Acta Crystallogr. A **44**, 912 (1988).

[11] D.A. Muller, Nature Mater. **8**, 263 (2009).

Chapter 3

MICROSTRUCTURAL CHARACTERIZATION OF CDTE SURFACE PASSIVATION LAYERS

This chapter describes the characterization of CdTe surface passivation layers grown on HgCdTe. The samples were provided by Dr. Steve Tobin and colleagues at BAE Systems (Lexington, MA). My role has been the microstructural characterization using electron microscopy. The major results of this collaborative research have been published elsewhere.[1]

3.1 Introduction

Surface effects in infrared detectors based on HgCdTe (MCT) largely dominate the lifetime of excess carriers.[2] Thus, the fabrication of high-performance MCT detectors depends on developing a process that is suitable for producing low surface recombination velocities. Hence, it becomes important to properly passivate the HgCdTe surface. The use of CdTe (CT) as a surface passivation layer was originally considered to be promising since CdTe is transparent to the infrared, it has high resistivity and it is nearly-lattice-matched to MCT.[3] The passivation of HgCdTe infrared detectors with CdTe has since become the standard approach in the infrared detector industry.[4] Investigations of long-wavelength infrared (LWIR) focal plane arrays (FPAs) using *p*- on *n*-HgCdTe double-layer heterojunctions have demonstrated that passivation with CdTe significantly improves the overall device performance.[5]

The epitaxial growth of CdTe on HgCdTe might be anticipated to reduce the number of dangling bonds at the MCT surface, which would in turn reduce defect generation centers, recombination centers, and possible defect traps at the CT/MCT interface.[3] Furthermore, a CT/MCT heterojunction with graded composition could produce an electric field in the HgCdTe layer that would repel minority carriers away from the interface and consequently improve the surface recombination velocity.[6] It has been reported that a thermally interdiffused CT/MCT interface leads to improvement in passivation, irrespective of the CdTe growth method used.[4] Moreover, thermally-induced compositional grading near the CT/MCT interface has been reported to shift the effective HgCdTe electrical surface away from the initial defective interface.[6] Such interdiffusion should lead to devices that are more thermally stable and do not degrade over time. Thermal annealing in an Hg atmosphere was reported to improve the overall microstructure of HgCdTe epilayers grown on CdTe buffer layers.[7] This improvement was attributed to a decrease in the number of Hg vacancies in the HgCdTe epilayers. Several studies addressing aspects of CdTe passivation of HgCdTe have been published.[2-6] However, publications describing microstructural characterization of the CdTe passivation layer and the CT/MCT interface are still very limited.

The transmission electron microscope (TEM) is a powerful instrument that provides a range of imaging and analytical techniques that are well suited for determining the microstructure and chemistry of HgCdTe materials down to the atomic scale. Such information is usually considered as essential for

understanding defect origins. This chapter reports a microstructural investigation of CdTe passivation layers deposited onto MCT heterostructures by different methods. The effects of annealing on the CdTe passivation layer and the CT/MCT interface were also studied. Additionally, the use of focused-ion-beam (FIB) milling as an alternative approach for preparing large-area cross-sectional TEM specimens was briefly evaluated.

3.2 Experimental details

The devices studied consisted of thick (~10-20 μm) *n*-type layers and thin (~1-3 μm) *p*-type layers, with final CdTe (~0.3-0.6 μm) passivation layers. The $Hg_{1-x}Cd_xTe$ (x~0.2-0.4) epilayers were grown by liquid-phase epitaxy (LPE) on nominally lattice-matched CdZnTe (111)B substrates. The indium-doped *n*-type absorber layers were grown in a horizontal slider system using a Te-rich melt. The arsenic-doped *p*-type capping layers with larger bandgap were then grown in a vertical dipper system using an Hg-rich melt. The CdTe capping layers were deposited by two different methods, namely hot-wall epitaxy (HWE) and molecular beam epitaxy (MBE). One of the wafers with a CdTe layer grown by MBE was annealed in Hg atmosphere at 250°C for 96h, with the primary objective being to determine any changes in the quality of the CT/MCT interface.

Samples for TEM characterization were usually prepared in the cross-sectional geometry using standard mechanical polishing and dimpling to thicknesses of about 30-40 μm, followed by argon-ion milling with the sample held at liquid nitrogen temperature. It is well known that II-VI semiconductors are

susceptible to structural damage during TEM specimen preparation.[8] Samples that were cooled before initiation of ion milling, however, did not exhibit defects, emphasizing the importance of keeping the sample at low temperature during the thinning process.[9] Final low-angle, low-energy (2.0keV) ion milling for a short period was often used to minimize the thickness of any remaining amorphous surface layers. An FEI Nova 200 FIB instrument was also used to cross-section additional samples prepared with a mesa device geometry, in particular to assess the usefulness of this approach in allowing simultaneous access to extended sample regions, which is often not possible using argon ion milling. The electron microscopy observations were mostly carried out using a JEOL JEM-4000EX high-resolution electron microscopy (HREM), operated at 400keV and equipped with a double-tilt, top-entry-type sample holder. High-angle annular-dark-field (HAADF) imaging and energy-dispersive X-ray spectroscopy (EDXS) were carried out using a JEOL 2010F transmission electron microscopy (TEM), equipped with a field-emission electron gun (FEG) and operated at 200keV. Samples were usually oriented for TEM observation along a HgCdTe [110] projection so that the growth normal was aligned perpendicular to the incident beam direction.

3.3 Results and discussion

The as-grown CdTe passivation layers were generally found to be columnar and polycrystalline, as illustrated by the representative cross-sectional electron micrograph shown in Fig. 3.1. It appeared that the polycrystalline CdTe layers

were only weakly bonded to the HgCdTe layers since there were no signs of any misfit dislocations being introduced at the CT/MCT interface, despite the ~0.2% lattice mismatch between materials. Moreover, there were no apparent changes in microstructure visible in the uppermost part of the HgCdTe layers.

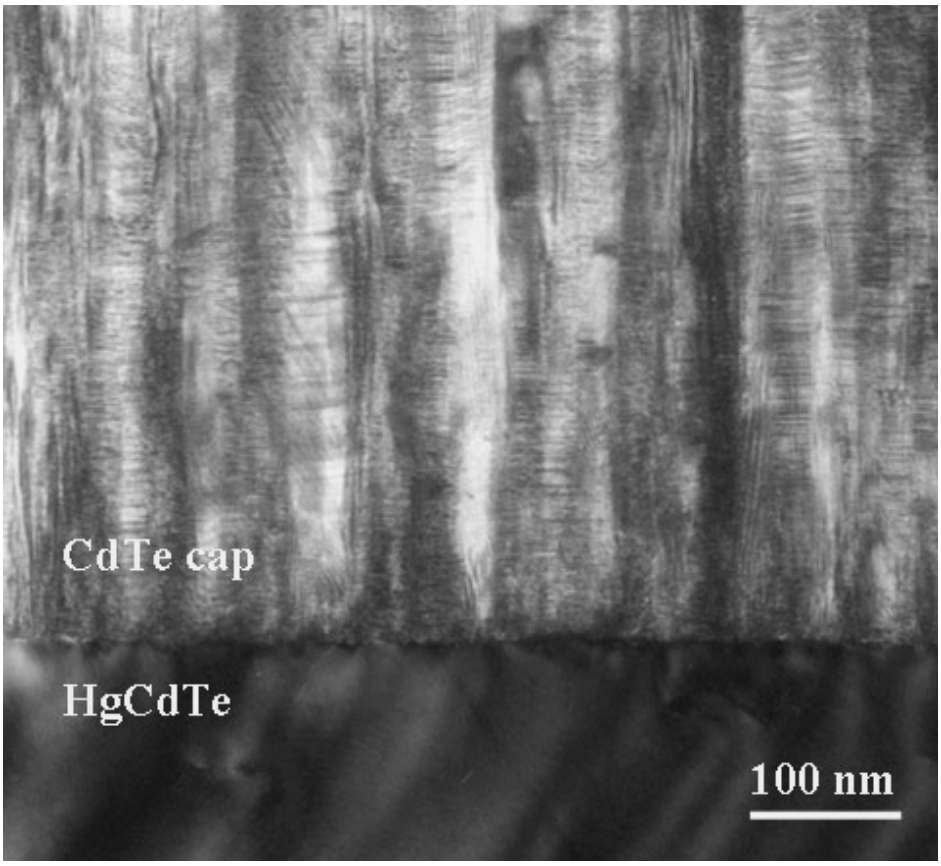

Fig. 3.1. Low-magnification bright-field electron micrograph showing cross section of CdTe/HgCdTe interface.

Two different growth techniques, namely hot-wall epitaxy (HWE) and molecular beam epitaxy (MBE), were used to deposit CdTe films on both planar and mesa MCT device structures, and these were found to result in different CdTe microstructure. As shown in Fig. 3.2, the CdTe grains were more irregular in shape when deposited by HWE, whereas those deposited by MBE were generally well-textured with mostly vertical grain boundaries. The average width of the CdTe grains deposited by HWE was determined to be approximately 40 nm, whereas the grains in the film grown by MBE were roughly 20 nm across.

Thermal annealing not only changed the morphology of the CdTe epilayer that was deposited by MBE, but also altered the nature of the interface. Micrographs such as those shown in Fig. 3.3 established that the CT/MCT interfaces had become more abrupt, and comparison of electron diffraction patterns (DPs), such as those shown as insets, also indicated that the overall crystallinity of the CdTe grains was substantially improved.

As visible in Fig. 3.4 (a), lattice fringes near the CT/MCT interface of the as-deposited sample were often considerably blurred, which was attributed to local interfacial disorder and roughness. Annealing transformed the initially disordered regions at the interfaces into more ordered regions, such as shown in Fig. 3.4 (b). Based on observations of the respective crystalline lattices, and measurements from extensive regions of several samples, the average width of this rough and uneven CT/MCT interfacial region was estimated to be about 4.0 nm before annealing, whereas the width of this region was reduced to approximately 1.0 nm after annealing.

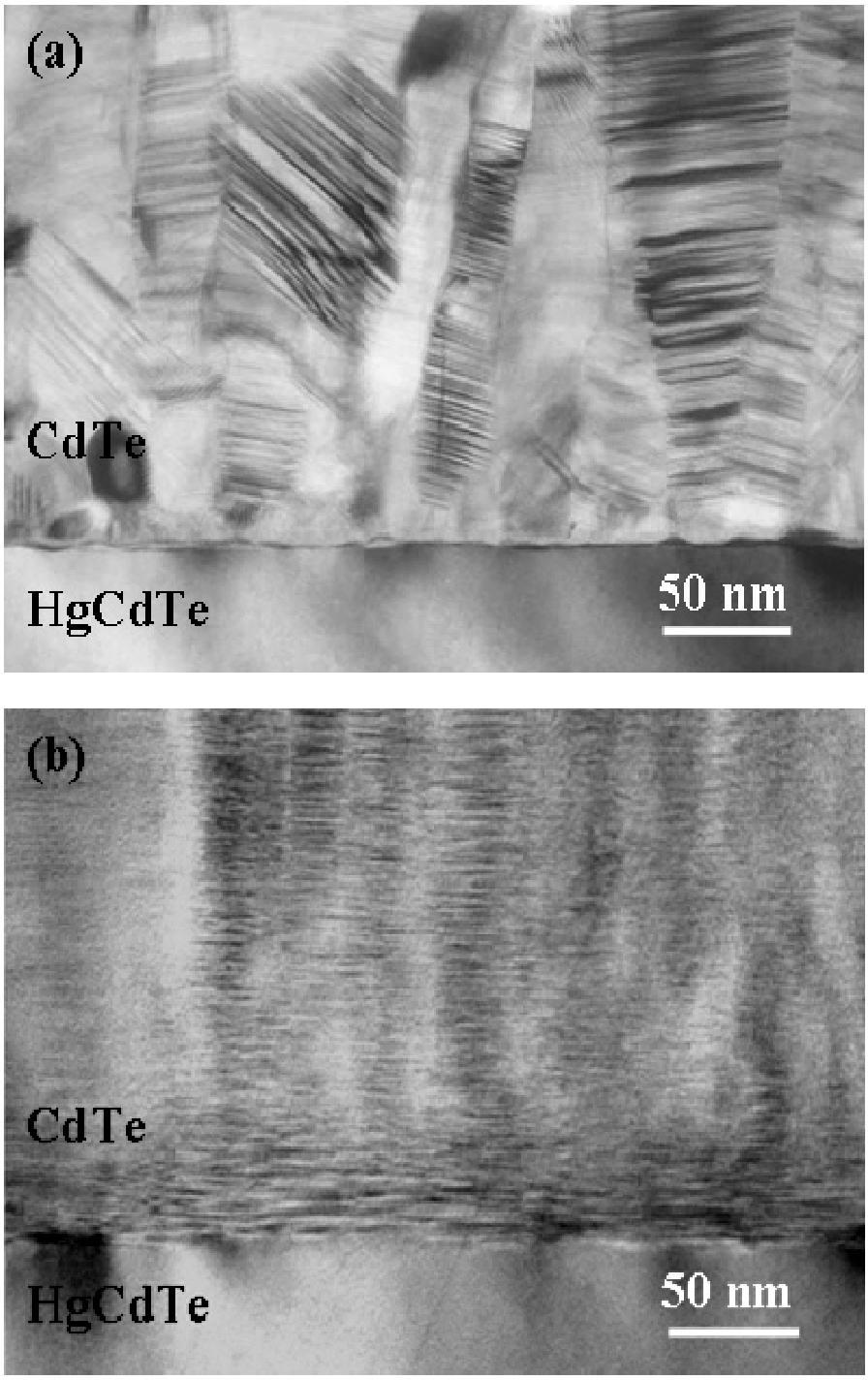

Fig. 3.2. Cross-sectional electron micrographs comparing the typical microstructure of CdTe capping layers deposited by: (a) HWE; and (b) MBE.

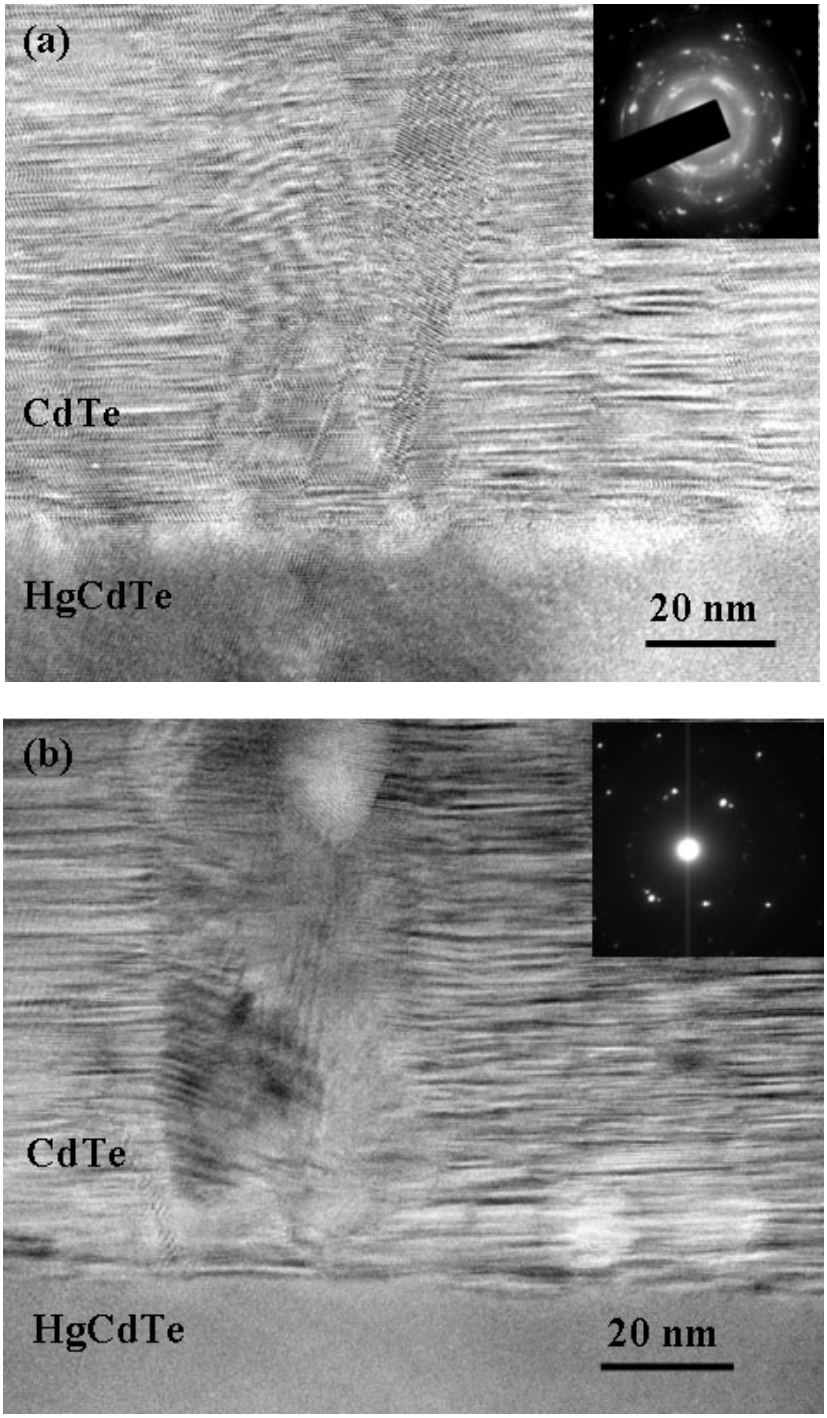

Fig. 3.3. Cross-sectional electron micrographs and inset selected-area electron diffraction patterns comparing the CdTe/HgCdTe interface (for MBE-grown CdTe sample): (a) before annealing; and (b) after annealing.

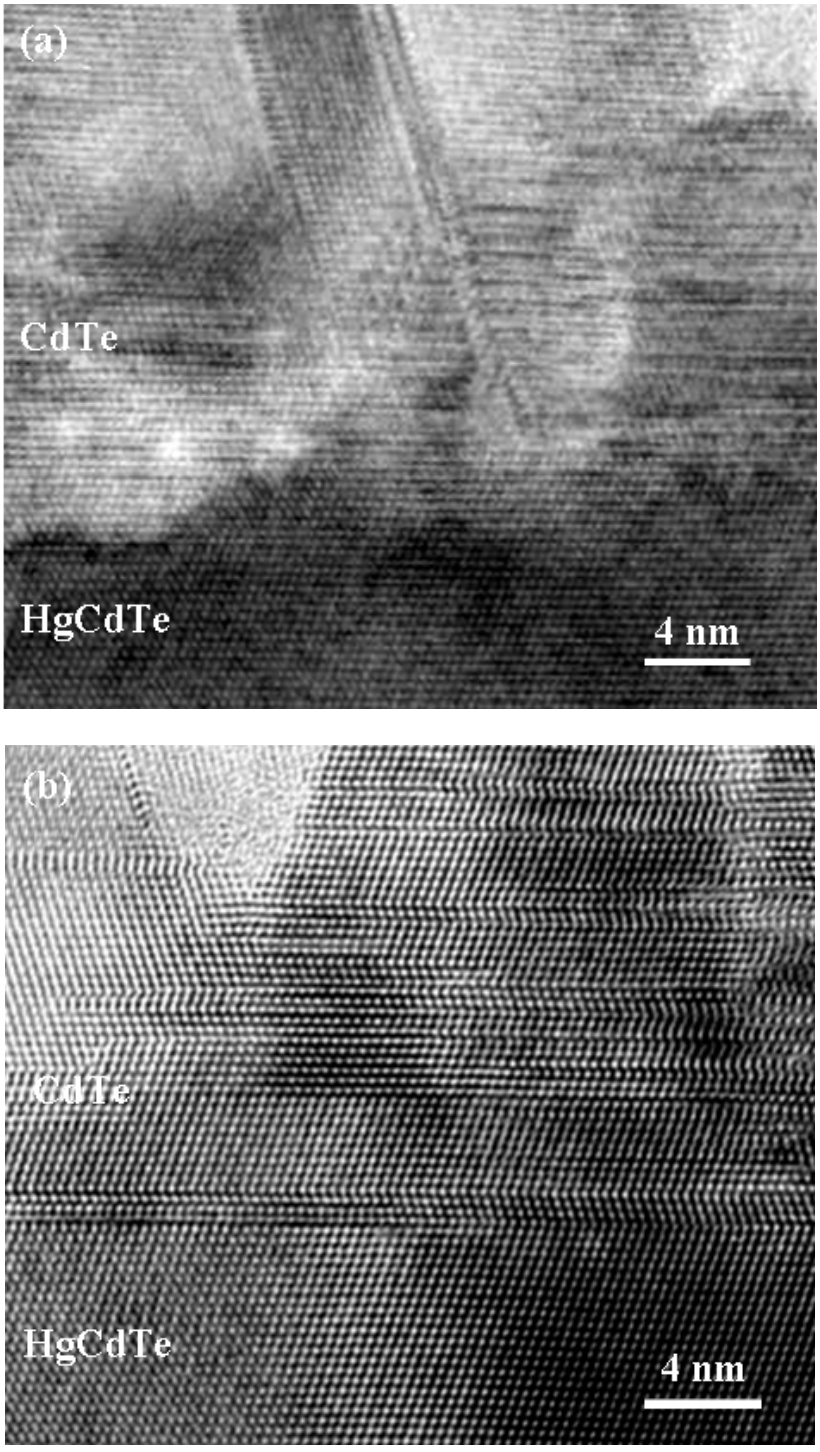

Fig. 3.4. High-resolution electron micrographs comparing flatness of CdTe/HgCdTe interface: (a) before annealing; and (b) after annealing.

HAADF has been used previously as a method for characterizing CT/MCT interfaces,[10] as well as MT/MCT superlattices.[11] Figures 3.5 (a) and (b) show HAADF images of CT/MCT interfaces before and after annealing, respectively. Since the level of contrast in HAADF images is strongly dependent on atomic number, the differences between the Cd-rich layers and the Hg-rich layers are clearly visible. From the intensity profiles of the HAADF images, the chemical profiles can also be estimated. Thus, the widths of the interface transition regions, corresponding to the samples before and after annealing, were determined to be ~8 nm and ~4.5 nm, respectively, based on measurements of the 10-90% change in intensity levels. These HAADF images and line profiles thus show the same trend of reduced surface abruptness after annealing. This trend is contrary to previous reports for epitaxial MCT/CT strained-layer superlattices,[12] but interfacial misfit strain is likely to be a strong driving force for interdiffusion in this specific system, which is unlike the current set of samples.

Figures 3.6 (a) and (b) show EDXS profiles corresponding to the lines arrowed in Figs. 3.5 (a) and (b). These profiles were obtained using a relatively large probe diameter (~1 nm) for statistical purposes. Based on measurements of the EDXS line profiles, the compositional abruptness of the CT/MCT interface was reduced from 16 nm to 11 nm by annealing. There are two major reasons for the differences between the line profile measurements of the interface abruptness from HAADF and EDXS. First, some broadening of the region excited by the beam (i.e., larger excitation volume) can be anticipated in the latter case. Second, EDXS signals are usually taken from much thicker sample areas than is the case

for HAADF images, also leading to beam broadening and apparent loss of spatial resolution.

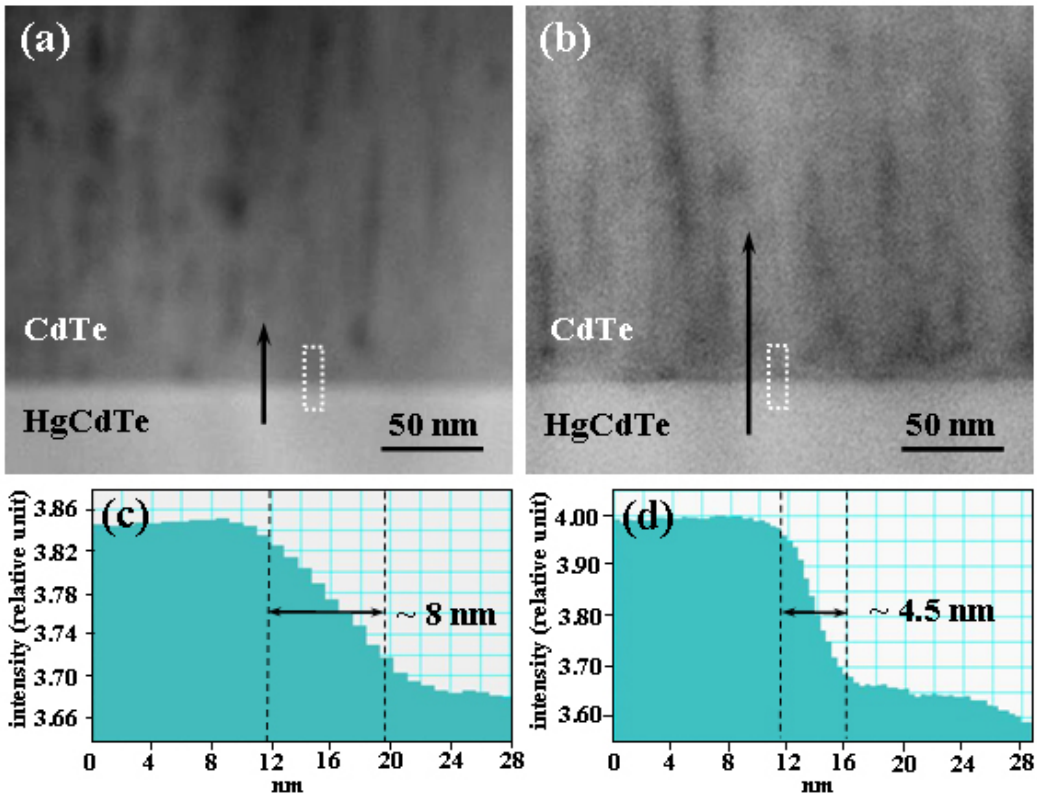

Fig. 3.5. HAADF images of CdTe/HgCdTe interface: (a) before annealing; and (b) after annealing; (c) profile along white box in (a); (d) profile along white box in (b).

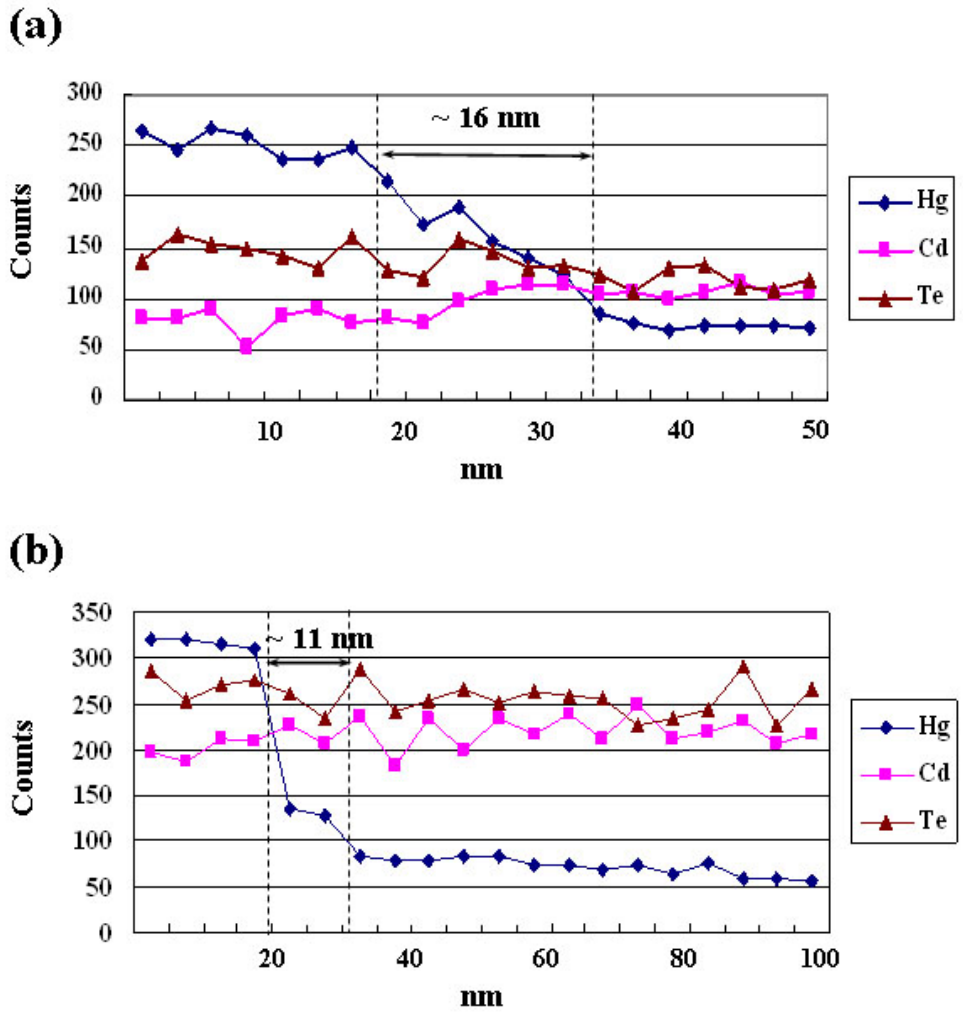

Fig. 3.6. (a) EDXS profile along line arrowed in Fig. 3.5 (a); and (b) EDXS profile along line arrowed in Fig. 3.5 (b).

Cross-sectioning of TEM samples using focused-ion-beam (FIB) milling enables the possibility of selecting highly specific areas as well as preparing much larger thin areas that are suitable for TEM observation. In the case of CdTe deposited on mesa structures, use of the FIB allowed simultaneous TEM observation of the top and side walls of the mesas, which could not otherwise have been achieved by conventional argon-ion-milling. As an example, Fig. 3.7 is a cross-section electron micrograph of a sample prepared using the FIB system, showing the *p*-type HgCdTe region, as well as the CdTe passivation layers deposited on the top and side walls of the mesa, which are also shown at higher magnification in the two enlargements. No major structural changes appear to have been induced as a result of the FIB milling process.

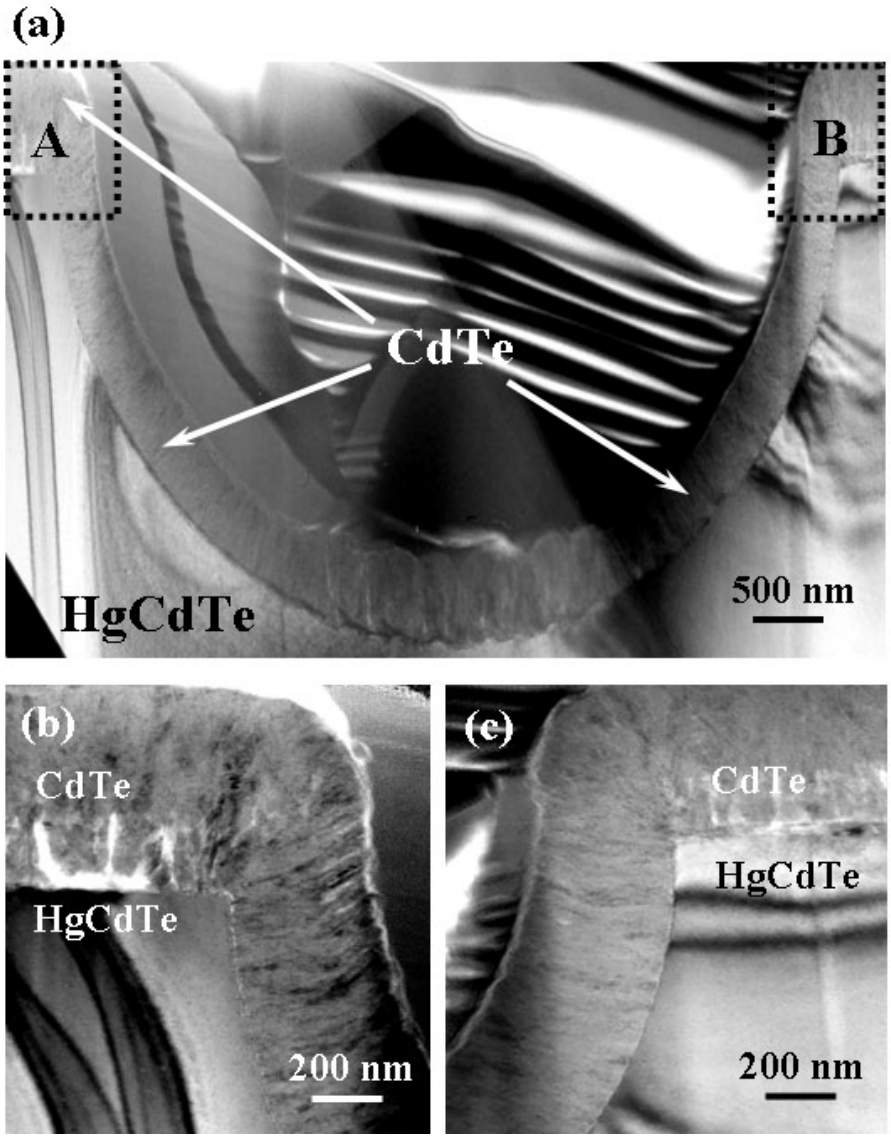

Fig. 3.7. (a) Cross-section electron micrograph of sample prepared using FIB milling showing *p*-type HgCdTe as well as CdTe passivation layers; (b) and (c) enlargements from boxed regions labeled A and B in (a).

3.4 Conclusions

In summary, the growth of CdTe passivation layers on HgCdTe by different techniques has been compared. TEM imaging was used to investigate the structural properties of the CdTe passivation layers, as well as to determine the effect of annealing on the CdTe/HgCdTe interface. The CdTe grains were larger and more irregular in shape when deposited by the hot-wall epitaxy method, while those deposited by MBE were generally well textured with mostly vertical grain boundaries. The flatness and abruptness of the CdTe/HgCdTe interface for the MBE-grown CdTe was shown by several different TEM methods to be substantially improved by annealing. The widths of the interface transition regions before and after annealing were determined to be ~8 nm and ~4.5 nm, respectively, and the compositional abruptness of the CdTe/HgCdTe interface was reduced from 16 nm to 11 nm.

REFERENCES

[1] W.F. Zhao, J. Cook, T. Parodos, S. Tobin, and D.J. Smith, J. Electron. Mater. **39**, 924 (2010).

[2] V. Kumar, R. Pal, P.K. Chaudhury, B.L. Sharma, and V. Gopal, J. Electron. Mater. **34**, 1225-1229 (2005).

[3] V. Ariel, V. Garber, D. Rosenfeld, and G. Bahir, J. Electron. Mater. **24**, 1169 (1995).

[4] L.O. Bubulac, W.E. Tennant, J. Bajaj, J. Sheng, R. Brigham, A.H.B. Vanderwyck, M. Zandian, and W.V. Mc Levige, J. Electron. Mater. **24**, 1175 (1995).

[5] O.P. Agnihotri, C.A. Musca, and L. Faraone, Semicond. Sci. Technol. **13**, 839 (1998).

[6] S.Y. An, J.S. Kim, D.W. Seo, and S.H. Suh, J. Electron. Mater. **31**, 683 (2002).

[7] Y.S. Ryu, T.W. Kang, T.W. Kim, Mater. Sci. Eng. B **122**, 80 (2005).

[8] T. Aoki, Y. Chang, G. Badano, J. Zhao, C. Grein, S. Sivananthan, and D.J. Smith, J. Cryst. Growth **265**, 224 (2004).

[9] C. Wang, S. Tobin, T. Parodos, and D.J. Smith, J. Electron. Mater. **35**, 1192 (2006).

[10] H. Lakner, B. Bolling, S. Underechts, and E. Kubalek, J. Phys. D: Appl. Phys. **29**, 1767 (1996).

[11] T. Aoki, M. Takeguchi, P. Boieriu, R. Singh, C. Grein, Y. Chang, S. Sivananthan, and D. J. Smith, J. Cryst. Growth **271**, 29 (2004).

[12] M.A. Mattson, T. H. Myers, M. Richards-Babb, and J. R. Meyer, J. Electron. Mater. **26**, 578 (1997).

Chapter 4

MICROSTRUCTURAL CHARACTERIZATION OF CDTE(211)B/ZNTE/SI(211) AND HGCDTE/CDTE/GAAS(211) HETEROSTRUCTURES GROWN BY MOLECULAR BEAM EPITAXY

The research described in this chapter was carried out in collaboration with Dr. Randy Jacobs and colleagues at U.S. Army RDECOM, CERDEC Night Vision and Electronic Sensors Directorate (Fort Belvoir, VA) and Dr. Yuanping Chen and colleagues at U.S. Army Research Laboratory (Adelphi, MD). The primary purpose of this specific research has been to contribute towards the development of improved HgCdTe (MCT) detectors and devices by investigating alternative substrates for MCT growth. My role has been the microstructural characterization using electron microscopy. Some of the results of this collaborative research have already been published.[1]

4.1 Introduction

The As-passivated Si(211) surface is currently the preferred alternative substrate for growth of HgCdTe by molecular beam epitaxy (MBE) for the large-scale production of HgCdTe focal-plane arrays (FPAs).[2] Si substrates offer overwhelming advantages relative to bulk CdZnTe for several reasons that include much larger size at very low cost, thermal expansion matching to Si readout chips, significantly reduced risk of impurity diffusion due to higher chemical purity, and the strength required for safe handing by automated wafer

processing equipment.[3] However, the large (~19%) lattice mismatch between Si and HgCdTe, as well as the big difference (~94% at 300K) in their thermal expansion coefficients, are major obstacles to high quality heteroepitaxial growth. Indeed, the lattice mismatch is considered as the primary reason accounting for the relatively high dislocation densities, that in turn adversely affect current state-of-art material.[4] The observed dislocation density in such HgCdTe/CdTe/Si structures is reported to be mid 10^6 cm^{-2}.[5] A further reduction in the CdTe buffer dislocation density is expected to benefit long-wave infrared (LWIR) HgCdTe detectors.[6] Close attention must, therefore, be given to controlling the generation and propagation of defects into the HgCdTe epilayer.

Much research has been undertaken to improve the quality of the CdTe layer that is often used as an intermediary buffer between Si and HgCdTe.[7-9] One promising approach involves deposition of thin buffer layers of ZnTe on the As-exposed Si(211) surfaces, followed by the growth of CdTe by MBE.[10] The ZnTe layer is commonly grown using migration-enhanced epitaxy (MEE). The MEE approach promotes a two-dimensional growth mode, while still minimizing the generation of growth defects.[11-14] The stepped Si(211) surface, which is composed of (111) terraces and (100) edges, allows a step-flow (Frank-van der Merwe) growth mechanism, which leads to reduced twinning and antiphase domain formation.[15] The primary role of the initial layer of ZnTe, which exhibits less lattice mismatch with Si (~12%) than CdTe with Si (~19%), is to provide improved B-face nucleation and better crystallinity for growth of the epitaxial CdTe layer.[16] The best HgCdTe/CdTe/Si composite structures suitable for short-

wave infrared and mid-wave infrared FPAs have been obtained using thick CdTe buffer layers (~ 10 μm). However, further reduction in dislocation density, by at least an order of magnitude, is still needed for high-performance long-wave infrared (LWIR) HgCdTe FPAs.[17]

The initiation of ZnTe growth and the microstructure of the CdTe(211)B/ZnTe/Si(211) heterointerfacial region are important factors that impact the final material quality. Thus, improved understanding of ZnTe nucleation, and better knowledge of the interface structure, should help to facilitate growth of higher quality epitaxial CdTe and HgCdTe for large-format, LWIR FPAs. In this study, the nucleation of ZnTe layers on stepped Si(211) surfaces, and the microstructure of the composite CdTe(211)B/ZnTe/Si(211) material have been characterized, using a wide range of transmission electron microscopy imaging and analytical techniques, including high-resolution electron microscopy (HREM), high-angle annular-dark-field (HAADF) imaging, and energy-dispersive X-ray spectroscopy (EDXS).

4.2 Experimental details

In this study, Si(211) substrate preparation by a common RCA technique was used.[18] The cleaning process consisted of degreasing in H_2O:NH_4OH:H_2O_2 (5:1:1) , stripping of the native oxide in dilute HF, and then formation of a thin protective oxide layer in a solution of H_2O:HCl:H_2O_2 (5:1:1). The final step involved spin-drying under a nitrogen atmosphere for 1 min. The wafer was then loaded into the MBE vacuum chamber, where oxide layer desorption and

passivation under an As flux were performed. This processing left a monolayer of As on the Si surface prior to deposition of ZnTe by MEE. The ZnTe layers were grown by alternating Zn and Te_2 fluxes with the substrate held at approximately 300°C. The full procedure consisted of 60 cycles followed by annealing at 450°C. The growth progress was closely monitored by observing reflection-high-energy electron diffraction (RHEED) patterns. Finally, the CdTe layer was deposited, and up to 10 cycles of periodic annealing during growth were incorporated in order to enhance dislocation interaction and annhiliation.[19]

Samples suitable for transmission electron microscope observation were prepared in the cross-sectional geometry using standard mechanical polishing and dimpling to thicknesses of about 5-10 μm, followed by argon-ion-milling at liquid nitrogen temperature to avoid any ion-milling-induced artefacts.[20] Low-angle, low-voltage (approximately 2.0keV) milling was used for final thinning to minimize the formation of any amorphous surface or interfacial layers. The electron microscopy observations were mostly carried out using a JEOL JEM-4000EX high-resolution electron microscope (HREM), operated at 400keV and equipped with a double-tilt, top-entry-type specimen holder. HAADF or "Z-contrast" imaging and EDXS analysis were carried out using a JEOL 2010F TEM, equipped with a field-emission electron gun and operated at 200keV. Samples were usually oriented for TEM observation along the common <110> projection.

4.3 CdTe(211)B/ZnTe/Si(211) heterostructure

Figure 4.1 is a cross-sectional electron micrograph of the CdTe(211)B/ZnTe/Si(211) interface showing short structural defects, most of which consisted of {111}-type stacking faults, originating at the Si substrate surface and typically terminating within less than 50 nm, as indicated by the arrows. The presence of these defects would seem to help alleviate the large misfit strain with the substrate. Electron diffraction patterns (see inset) revealed rotation angles of ~3.5° between the Si substrate and final CdTe epilayer. Higher magnification images, such as Fig. 4.2, showed the stepped nature of the Si(211) surface and suggested that many of the {111} lattice fringes were continuous across the interface.

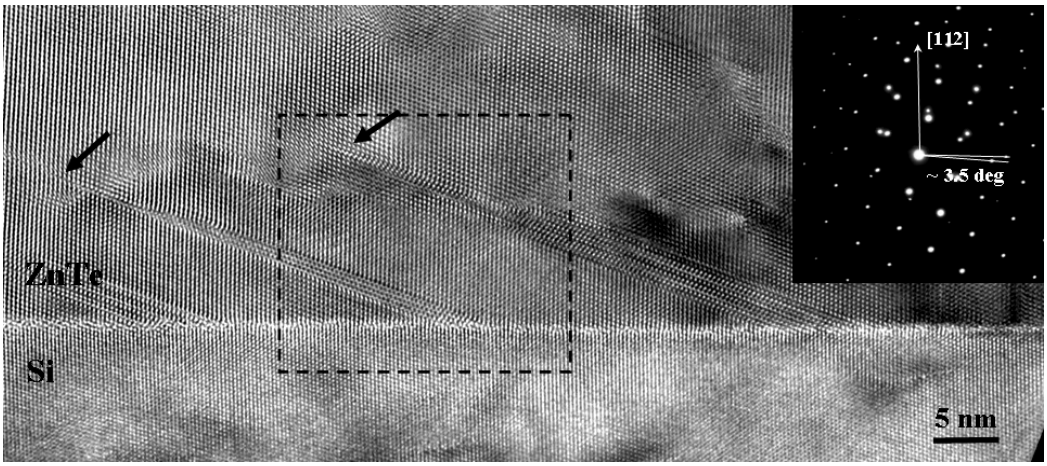

Fig. 4.1. Cross-sectional electron micrograph of CdTe(211)B/ZnTe/Si(211) interface. Electron diffraction pattern (inset) shows slight rotation (~3.5°) between CdTe/Si crystal lattices.

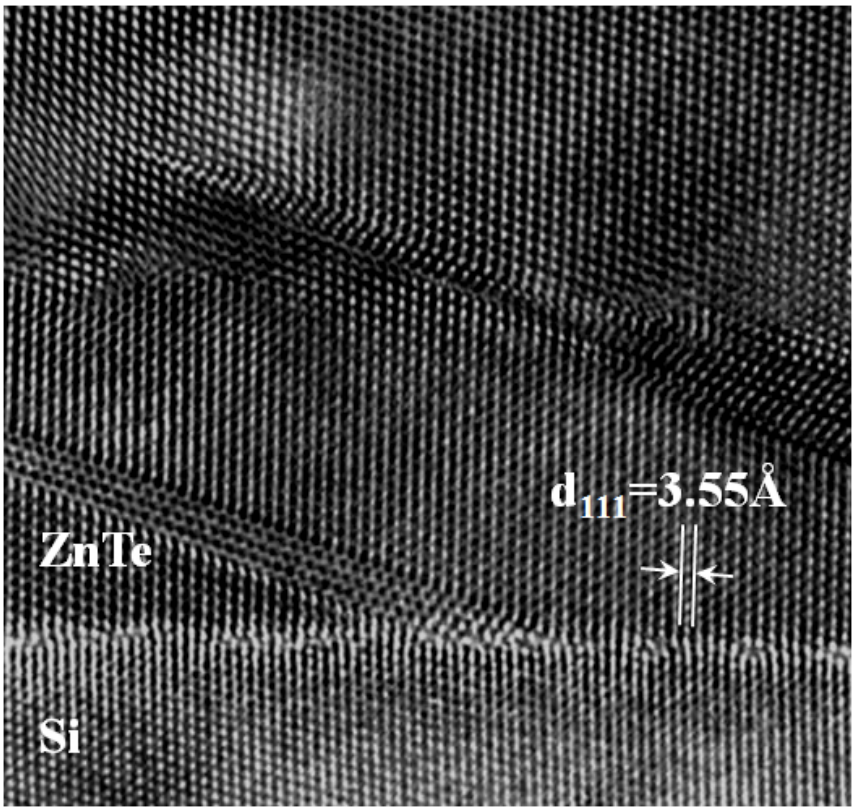

Fig. 4.2. Enlargement of Fig. 4.1 showing atomic structure at the ZnTe(211)/Si(211) interface region.

Direct measurement of lattice-fringe spacings was used to estimate the Zn concentration in the $Cd_{1-x}Zn_xTe$ layer for different distances from the interface based on Vegard's law. If y is the local lattice constant, which can be calculated from the d(111) spacings, then x can be calculated using the expression $y = 6.477 - 0.376x$. The results are shown in Fig. 4.3. The concentration of Zn was estimated to be about 87% from the Si substrate surface up to about 4 nm, then dropping continuously to zero between 4 nm and 14 nm, indicating a progressive change to CdTe upon moving further away from the substrate.

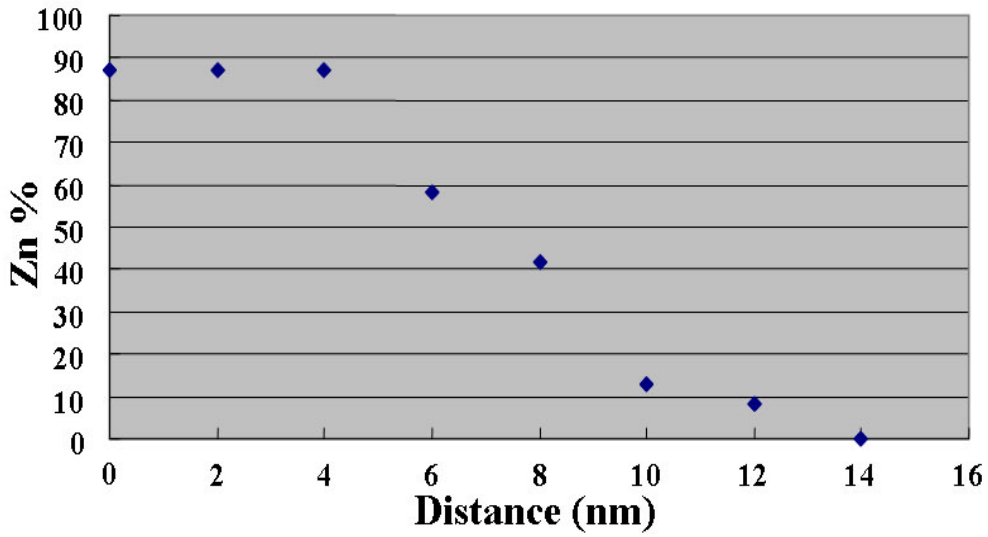

Fig. 4.3. Zn concentration profiles based on Vegard's law, as obtained from measurement of lattice-fringe spacings using Si substrate for calibration purposes.

Compositional analysis was also used to determine elemental profiles. Figure 4.4 (a) shows a HAADF image of the CdTe(211)B/ZnTe/Si(211) interface, and Fig. 4.4 (b) show an EDXS line profile from the arrowed region. A relatively large probe size (~1 nm) was used for acquiring the EDXS line scan. The result shows that the Zn signal peaks in the middle of the ZnTe layer, and also indicates that there is some intermixing of Zn and Cd, which is consistent with the lattice-spacing measurements. The spectra shown in Fig. 4.4 (c) were recorded by placing the focused probe in turn at the ZnTe/Si interface, in the middle of the ZnTe buffer layer, and in the CdTe layer, as indicated by the numbers in Fig. 4.4 (a). It is clear that As was present at the ZnTe/Si interface, and that it had not diffused into the ZnTe layer.

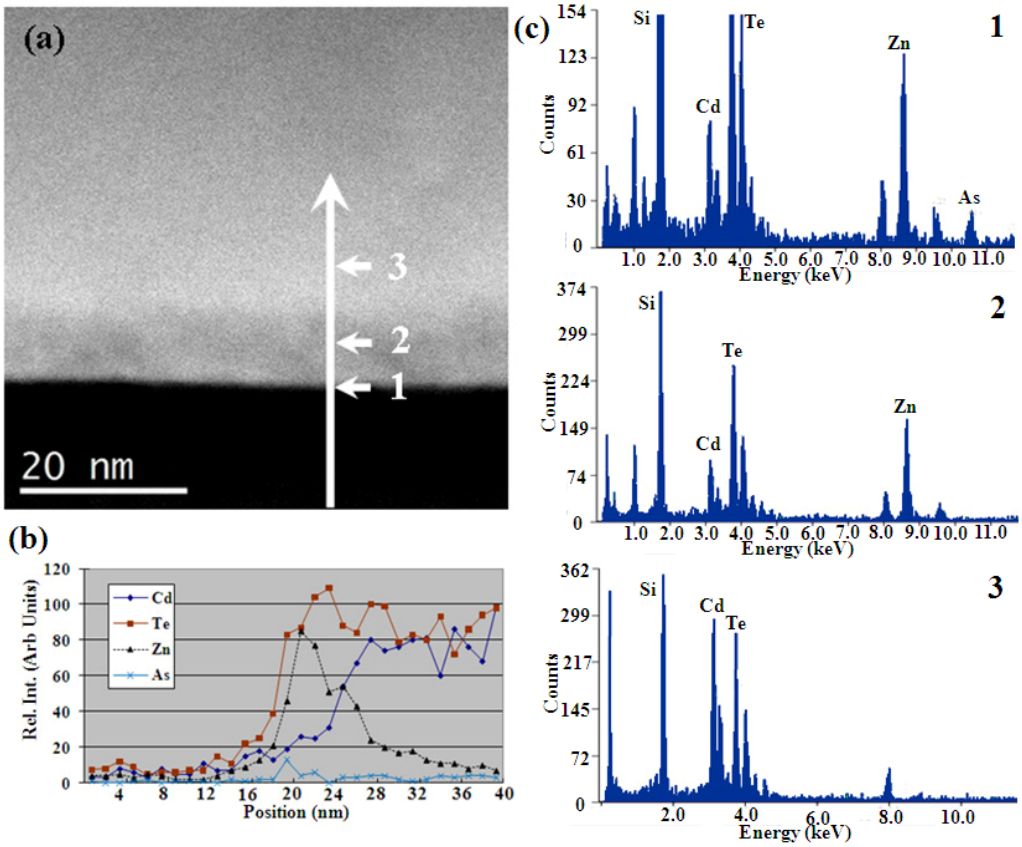

Fig. 4.4. (a) HAADF image showing region used for analysis; (b) EDXS elemental profile along line indicated in (a); (c) individual spectra taken in turn from three different regions, as indicated by the numbers 1, 2, and 3.

As shown by the Z-contrast image in Fig. 4.5 (a), which was obtained using a small probe (~0.2 nm), the region of the CdTe/ZnTe interface was often quite disordered and uneven. The widths of the ZnTe layer and the (Cd, Zn)Te transition region were measured to be roughly 6.5 nm and 3.5 nm, respectively, for the specific growth conditions used in these experiments, as shown in Fig. 4.5 (b). Thus, it can be concluded that the {111}-type stacking faults were present throughout the entire ZnTe layer, terminating near the point of initiation of the

CdTe growth (as shown in Fig. 4.1), which was also consistent with *in situ* RHEED pattern observations made during growth. Formation of the (Cd, Zn)Te transition region may happen either as a result of interdiffusion occurring at the onset of CdTe growth or as a result of annealing.[21]

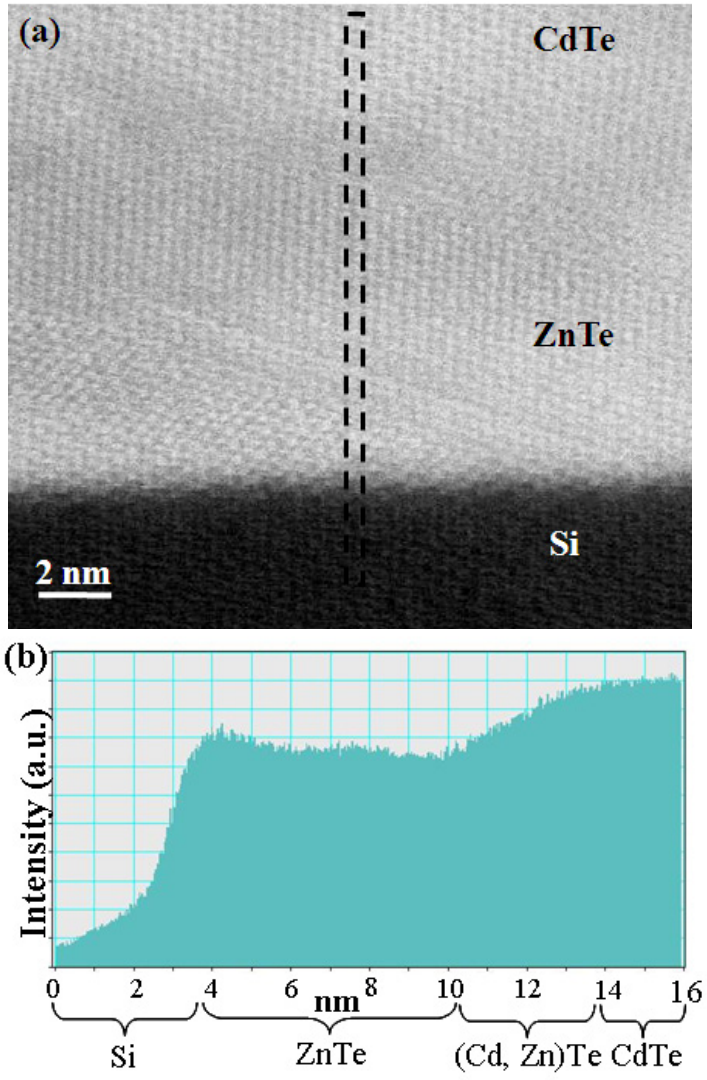

Fig. 4.5. (a) HAADF image of CdTe(211)B/ZnTe/Si(211) interfacial region; (b) intensity profile along box in (a).

4.4 The effects of *in situ* annealing on CdTe/Si

It has been reported that *in situ* thermal cycle annealing (TCA), wherein annealing is performed intermittently during the growth process itself, is an effective means to reduce etch pit density (EPD) to the value of mid-10^5 cm^{-2} and improve overall crystal quality.[5] The effects of annealing on the microstructure of CdTe layers grown by MBE on ZnTe/Si(112) substrates were studied using TEM.

Figure 4.6 (a) and (b) are high-resolution electron micrographs showing the CdTe(211)B/ZnTe/Si(211) heterostructure before annealing and after 10 cycles of annealing, respectively. Most of the growth defects observed in the thin ZnTe layer consisted of {111}-type stacking faults originating at the Si substrate surface and typically terminating within less than 50 nm. The CdTe(211)B/ZnTe/Si(211) heterostructure after annealing seems to have less {111}-type stacking faults near the interface. Otherwise, not much change of film microstructure has been identified between samples before annealing and after annealing.

Figure 4.7 (b) is the corresponding fast Fourier transform (FFT) of the region shown in Fig. 4.7 (a). When only the {111} reflections marked by triangles were used for the inverse FFT, then Fig. 4.7 (c) was obtained, with fringes due to the (111) planes being visible. It is apparent that the (111) lattice fringes cross the CdTe(211)B/ZnTe/Si(211) interface continuously, without any misfit dislocations. When the other two {111} reflections marked by circles were used, then Fig. 4.7 (d) was obtained, with fringes due to the (-111) planes being visible. As shown in Fig. 4.7 (d), the misfit dislocations distributed evenly at the ZnTe/Si(211)

interface. Apparent misfit dislocations present at the CdTe(211)B/ZnTe interface are also visible, as arrowed in Fig. 4.7 (d).

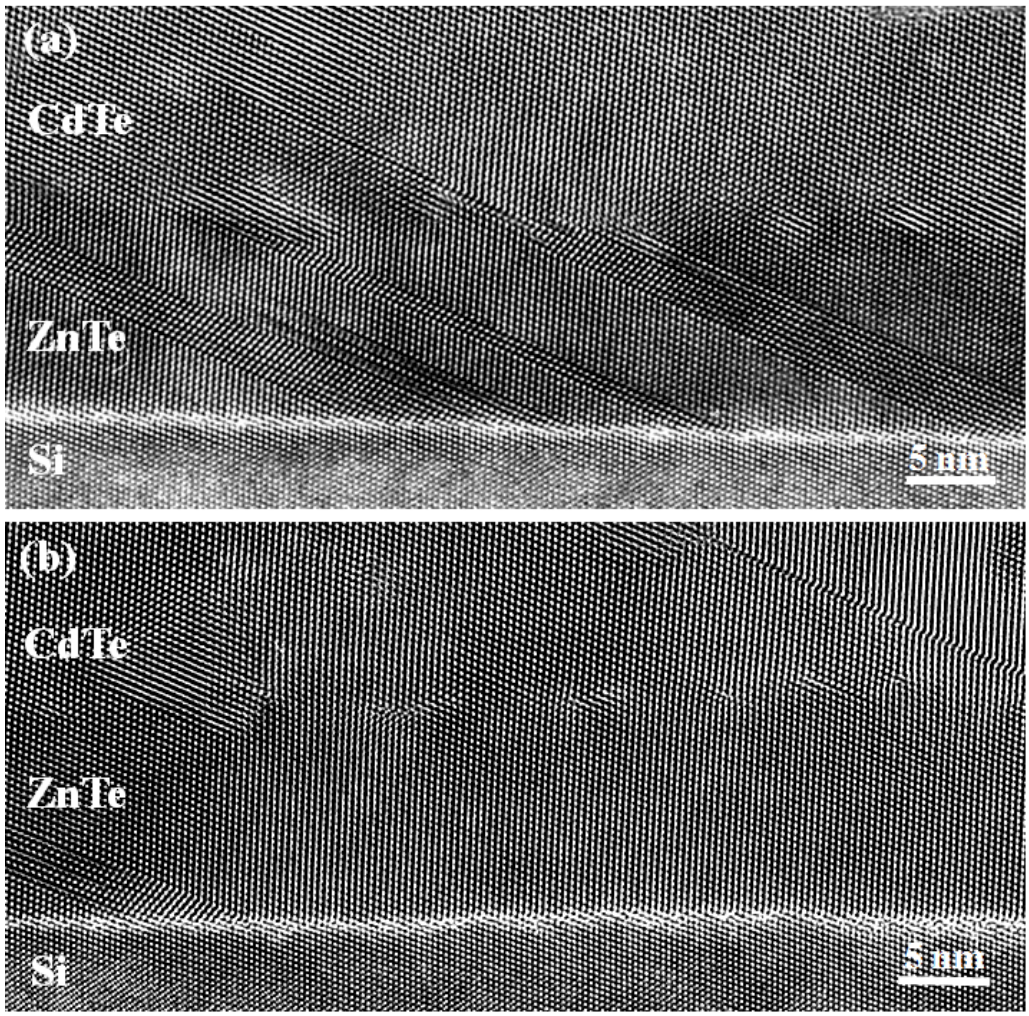

Fig. 4.6. High-resolution electron micrographs comparing the CdTe(211)B/ZnTe/Si(211) heterostructure: (a) before annealing; (b) after 10 cycles of annealing.

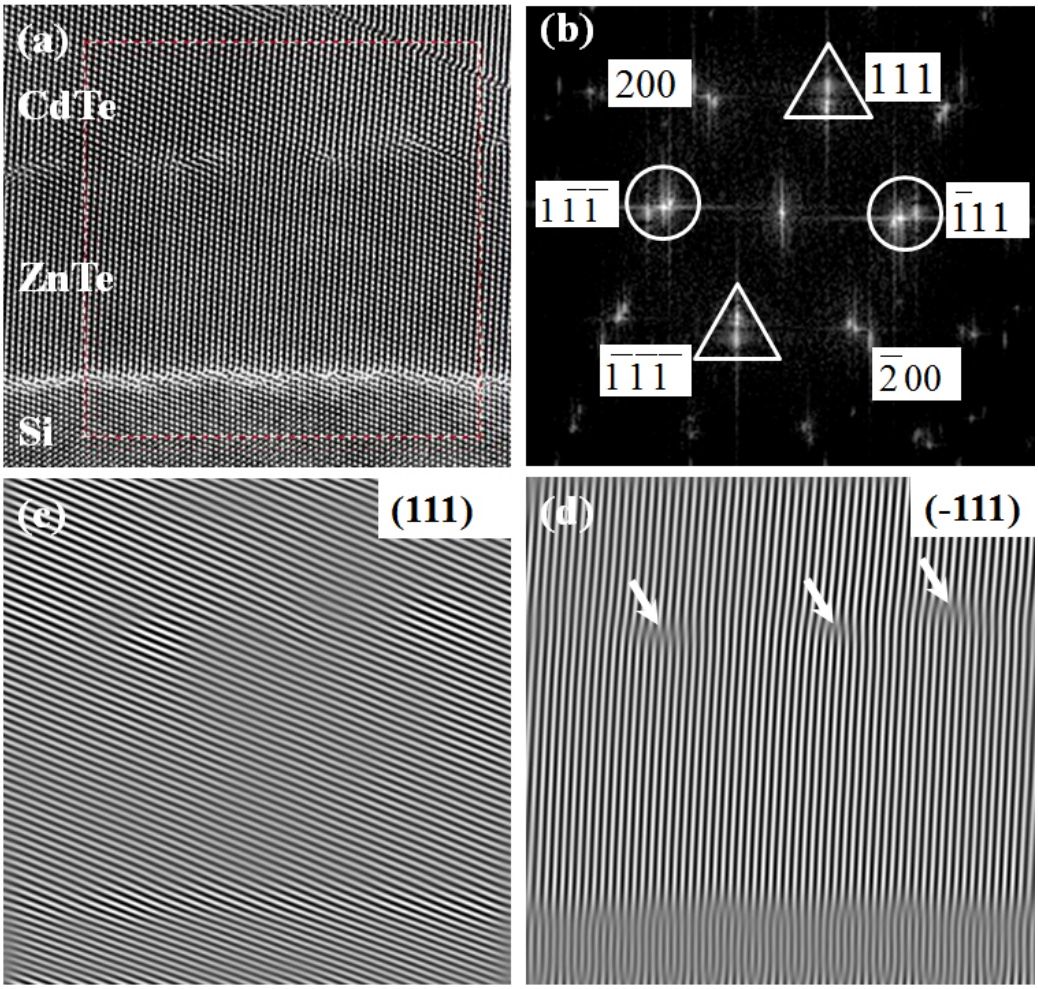

Fig. 4.7. (a) HREM of the CdTe(211)B/ZnTe/Si(211) interface; (b) diffractogram of TEM image; (c) inverse fast Fourier transform image displaying (111) planes. (d) inverse FFT image displaying (-111) planes.

4.5 Alternative GaAs-based substrates for growth of HgCdTe (MCT)

The quest to identify alternative substrates for MCT growth also includes GaAs(211). Since 1983, GaAs has been the subject of much research as an alternative substrate for HgCdTe.[22] Similar to Si, GaAs substrates are much stronger, available in larger areas with high quality, and less expensive than

CdZnTe. The lattice mismatch of GaAs with CdTe is 14.6%, considerably lower than that of Si which is 19.3%. GaAs has an advantage over Si as a substrate for MBE growth of MCT in that the temperature required for GaAs surface cleaning is lower than for Si, therefore reducing the likelihood of recontamination of the substrate surface.[23] Preliminary observations of CdTe(211)B/GaAs(211) heterostructures grown by MBE suggest much reduced defect densities both near the vicinity of the substrate and within the CdTe epilayers.

Figure 4.8 is a cross-sectional electron micrograph of CdTe(211)B/GaAs(211) showing examples of dislocations that originate at or near the interface and also terminate close to the interface. Figure 4.9 is a selected-area electron diffraction pattern (DP) of the interfacial region, taken along <110> projection. The inner spots correspond to CdTe, while the outer spots correspond to GaAs. The DP shows accurate alignment of the two lattices and also reveals the large lattice mismatch (14.6%) between CdTe and GaAs.

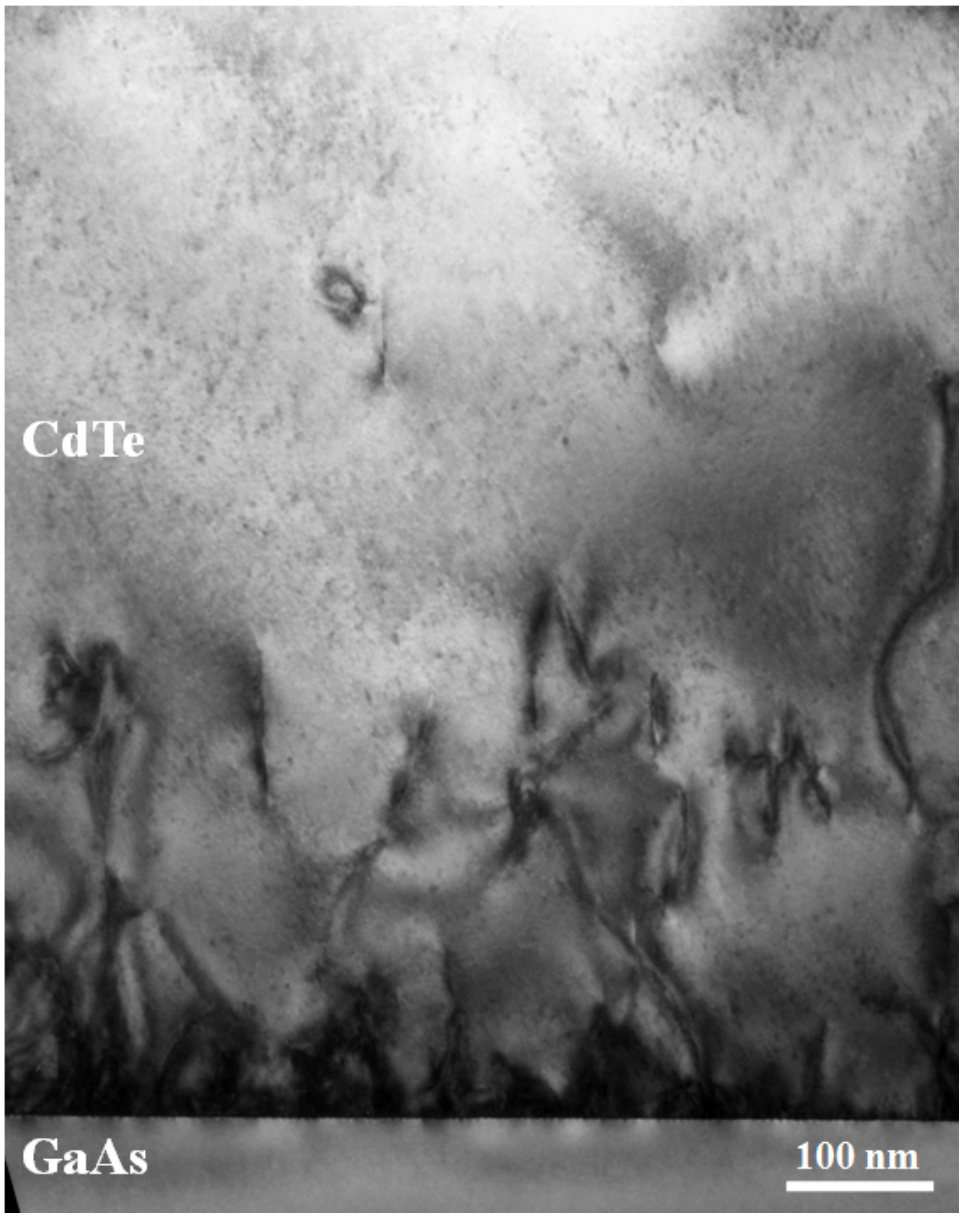

Fig. 4.8. Cross-sectional electron micrograph showing dislocations originating from the vicinity of CdTe(211)B/GaAs(211) interface.

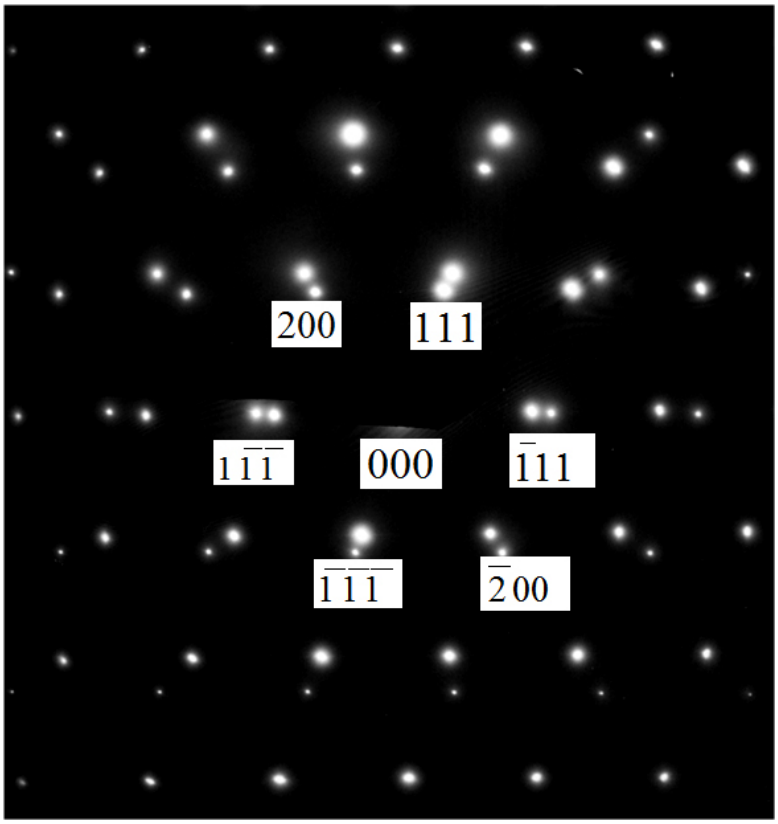

Fig. 4.9. Electron diffraction pattern for the CdTe(211)B/GaAs(211) heterostructure showing excellent alignment between two materials.

Figures 4.10 (a) and (b) are cross-sectional TEM micrographs showing the microstructure of the CdTe(211)B/GaAs(211) heterostructure, as grown by MBE. Most of the growth defects observed in the CdTe layer consist of {111}-type stacking faults originating at the Si substrate surface and typically terminate within less than 50 nm, as shown in Fig. 4.10 (a). The presence of these defects would help to alleviate the large misfit strain with the GaAs substrate, similar to the case for CdTe thin films grown on Si substrates. However, there seem to be less {111}-type stacking faults for CdTe grown on GaAs compared with CdTe grown on Si. The most likely reason could be the lattice mismatch of GaAs with CdTe, which is at 14.6%, is lower than that of Si (19.3%). Higher magnification images, as shown in Fig. 4.10 (b), showed the stepped nature of the GaAs(211)B surface, and suggested that the majority of the {111} lattice fringes were continuous across the interface.

Figure 4.11 (b) is the corresponding FFT of the interface region shown in Fig. 4.11 (a). When only the {111} reflections marked by the triangles were used for the inverse FFT, then Fig. 4.11 (c) was obtained, with fringes due to the (111) planes being visible. It is apparent that the (111) lattice fringes cross the CdTe(211)B/GaAs(211) interface continuously, without any misfit dislocations. When the other two {111} reflections marked by the circles were used, then Fig. 4.11 (d) was obtained, with fringes due to the (-111) planes being visible. As indicated by the arrows, the misfit dislocations are distributed evenly along the CdTe(211)B/GaAs(211) interface.

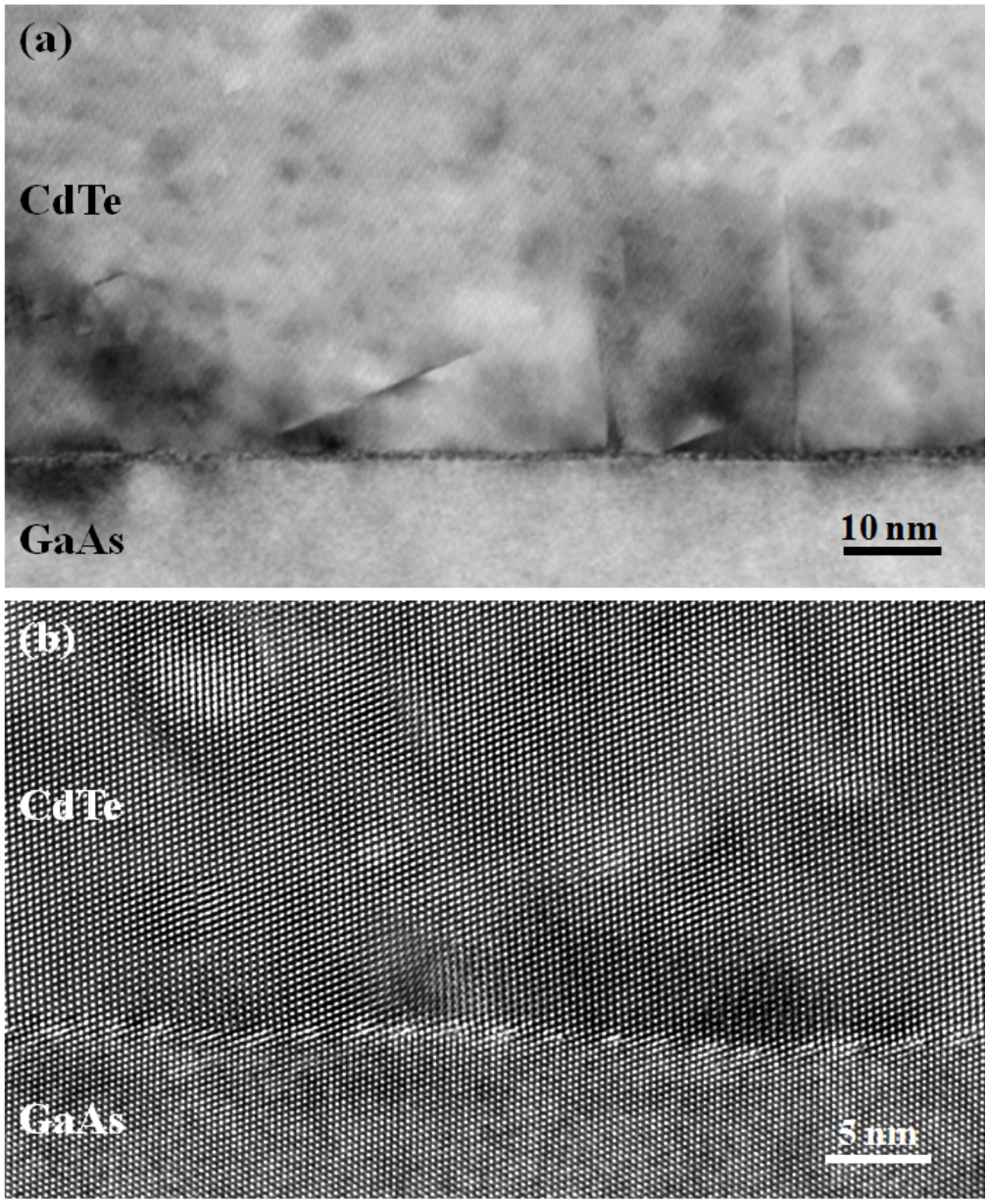

Fig. 4.10. (a) Cross-sectional electron micrograph showing interface of MBE-grown CdTe(211)B/GaAs(211) heterostructure; (b) High-resolution electron micrograph showing the interface between CdTe and GaAs.

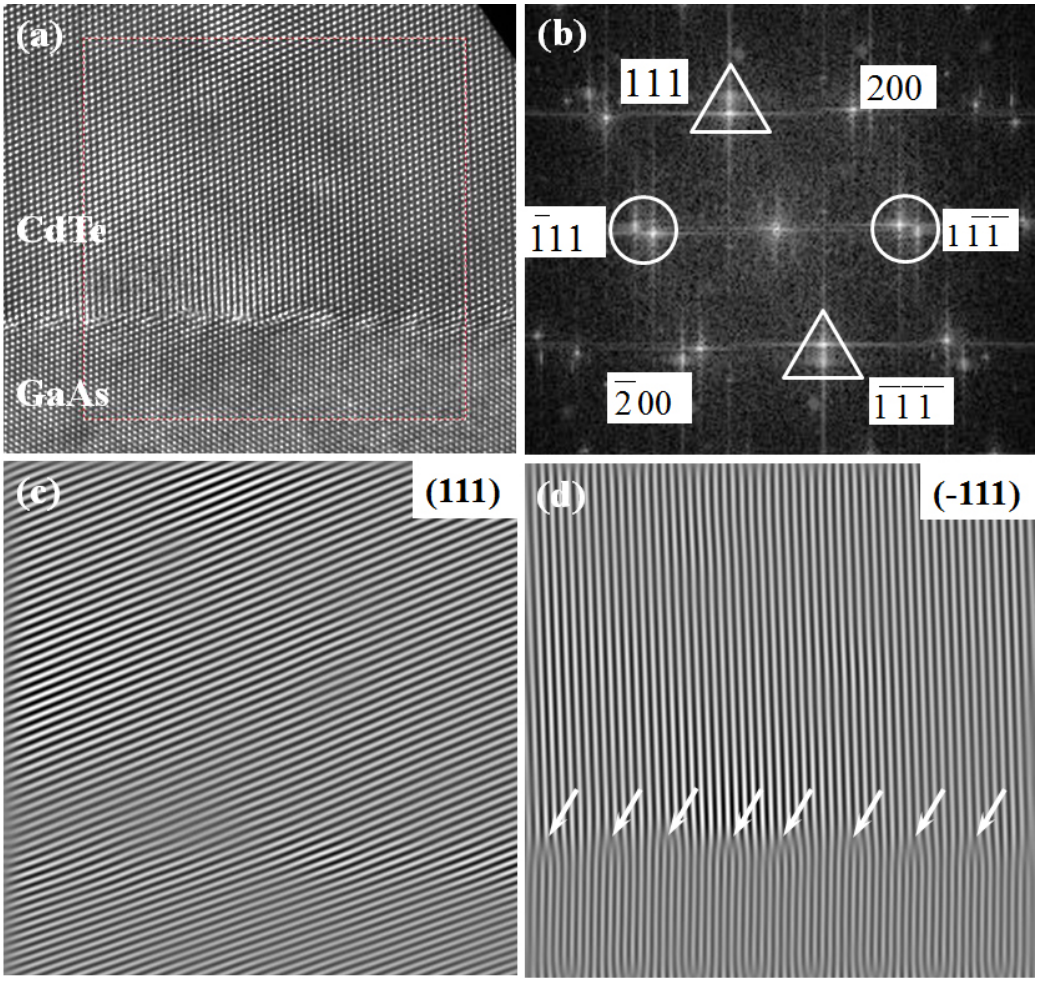

Figure 4.11. (a) HREM of the CdTe(211)B/GaAs(211) interface; (b) diffractogram of TEM image; (c) inverse fast Fourier transform image displaying (111) planes. (d) inverse fast Fourier transform image displaying (-111) planes.

Figure 4.12 is a cross-sectional electron micrograph showing the presence of precipitates and stacking faults at the CdTe surface, which are indicated by the white and black arrows. These precipitates were initially observed at the CdTe surface, before growth of the HgCdTe epilayer.

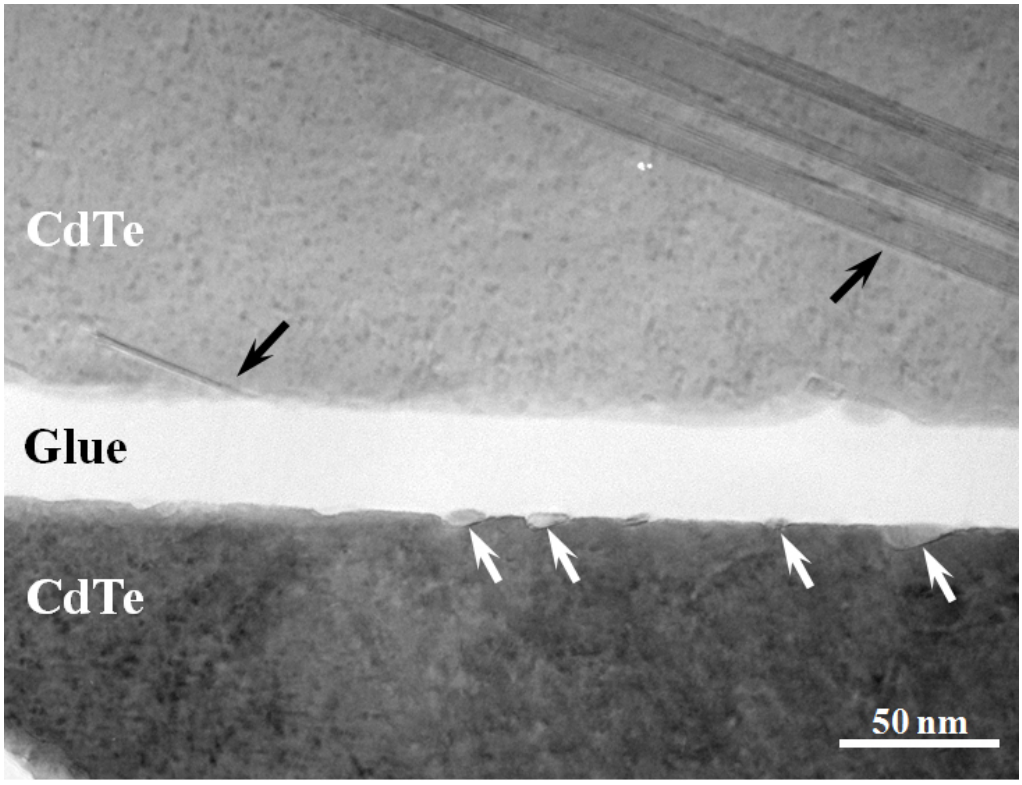

Figure 4.12. Cross-sectional electron micrograph showing precipitates and stacking faults on CdTe(211)B/GaAs(211) surface.

Similar precipitates were later observed at the HgCdTe/CdTe interface of a composite HgCdTe/CdTe(211)B/GaAs(211) sample, as shown in Fig. 4.13. The formation of these precipitates could possibly be caused by the growth interruption that occurred because deposition of the CdTe buffer layer and growth of the subsequent HgCdTe epilayer were carried out sequentially in two separate MBE chambers. It appears that no defects in the HgCdTe layer were caused by these precipitates, but whether or not these precipitates are detrimental to detector performance is not yet been known.

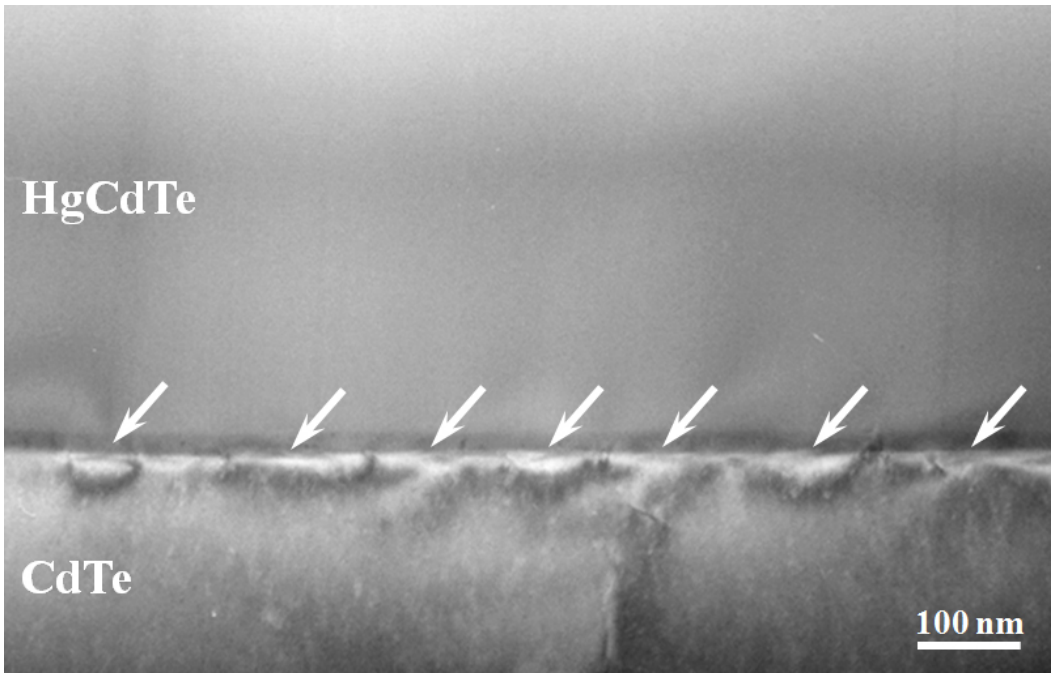

Figure 4.13. Cross-sectional electron micrograph showing HgCdTe(211)/CdTe(211)B heterostructure. Arrows indicate the presence of precipitates.

Figure 4.14 is a cross-sectional electron micrograph showing an example of dislocations that originate at the HgCdTe/CdTe interface and terminate at the early stages of HgCdTe growth.

High-resolution electron micrographs such as Fig. 4.15 confirmed that high quality HgCdTe could be achieved on CdTe(211)B/GaAs(211) composite substrate. No dislocations or stacking faults were observed at or near the interface in this region. Indeed, the precise position of the HgCdTe/CdTe interface is difficult to determine because of the uniform contrast between HgCdTe and CdTe. However, since CdTe was greatly damaged by argon-ion milling, whereas

HgCdTe was relatively free of ion-milling damage, the position of the HgCdTe/CdTe interface as indicated by the arrows can be determined by observing structural differences between the two layers.

Figure 4.16 is a cross-sectional electron micrograph taken near the top surface of the HgCdTe. In general, the bulk HgCdTe material was generally of high quality, whereas the region near the top surface was found to be quite defective.

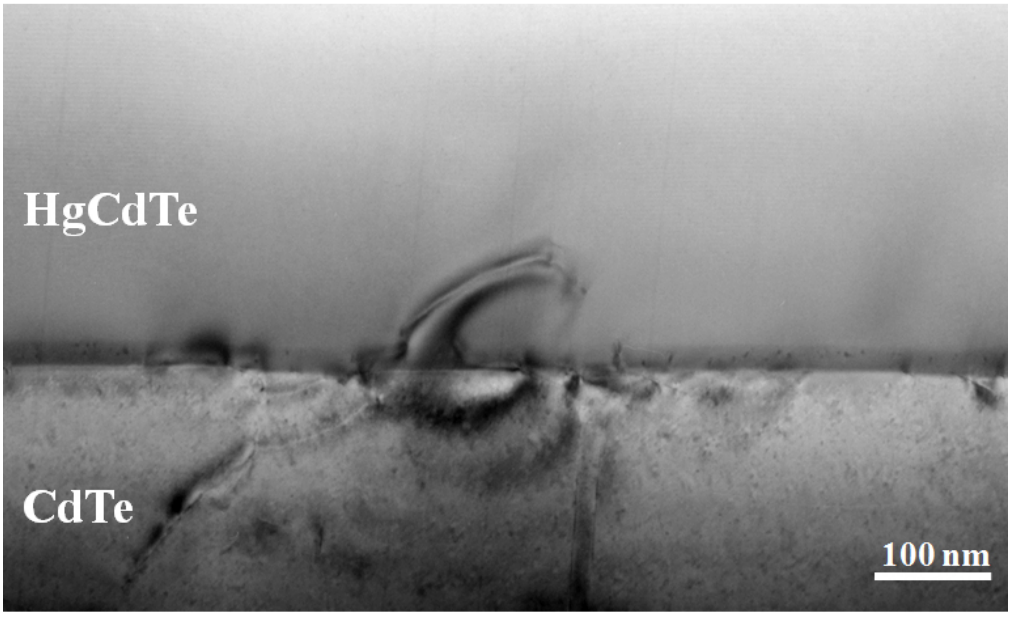

Figure 4.14. Cross-sectional electron micrograph showing HgCdTe(211)/CdTe(211)B heterostructure.

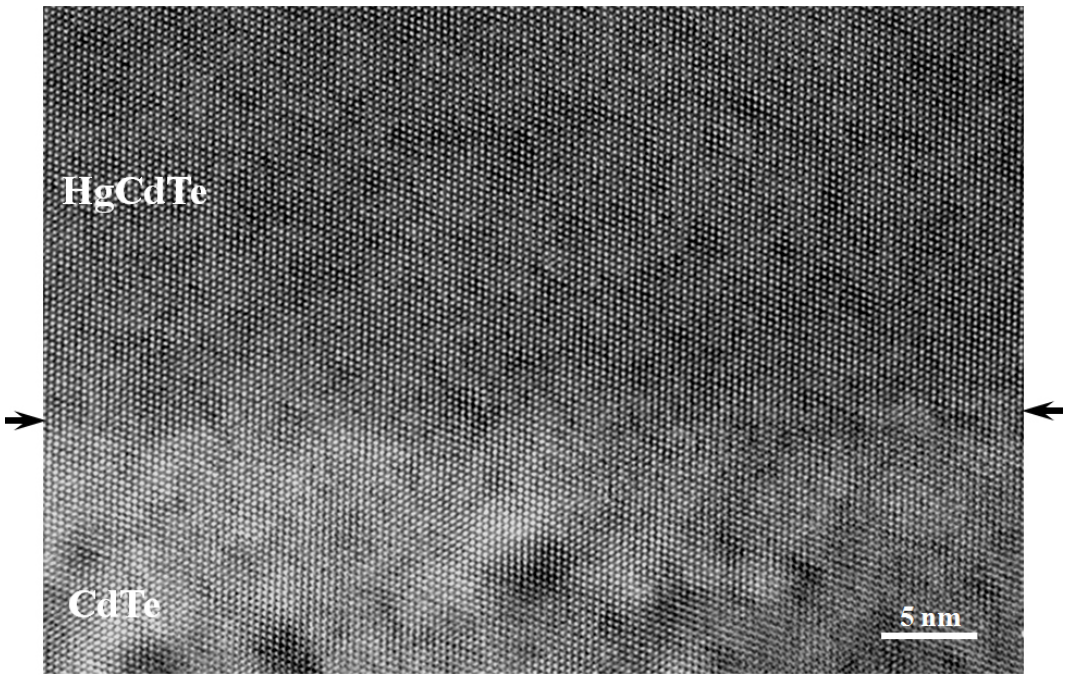

Figure 4.15. High-resolution electron micrograph showing the interface between HgCdTe and CdTe.

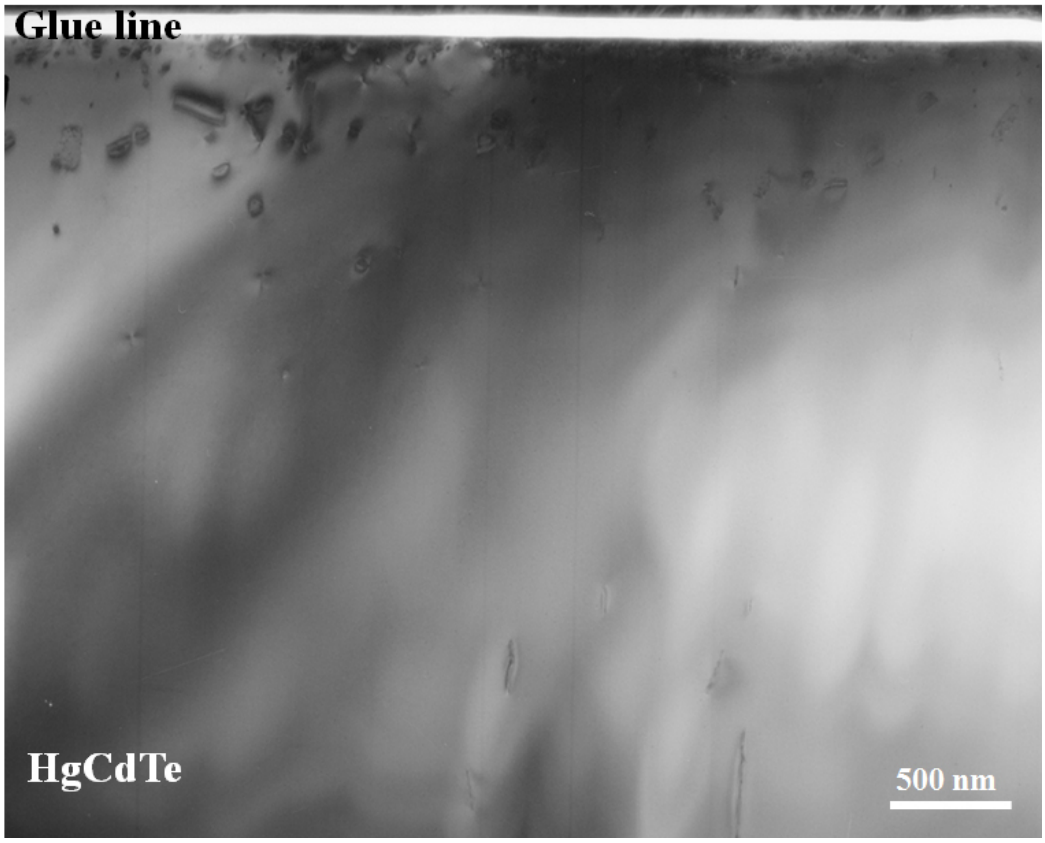

Fig. 4.16. Cross-sectional electron micrograph showing microstructure near the top surface of the HgCdTe.

4.4 Conclusions

In summary, CdTe(211)B/ZnTe/Si(211) and CdTe(211)B/GaAs(211)B heterostructures grown by MBE have been evaluated using different electron microscopy techniques. HREM imaging revealed the morphology of the CdTe(211)B/ZnTe/Si(211) interface and showed that most stacking faults formed at the Si substrate surface continued through the entire ZnTe layer, terminating near the point of initiation of CdTe growth. Lattice-spacing measurements and microanalytical studies mapped out chemical profiles across the CdTe(211)B/ZnTe/Si heterostructures, and indicated that interdiffusion between CdTe and ZnTe had occurred. HAADF imaging revealed that the region of the CdTe/ZnTe interface was quite disordered and uneven in thickness. The average width of the ZnTe layer and the (Cd, Zn)Te transition region were measured to be approximately 6.5 nm and 3.5 nm, respectively. Preliminary observation of CdTe(211)B/GaAs(211) heterostructures suggests much reduced defect densities both near the vicinity of the substrate and within the CdTe epilayers. HgCdTe epilayers grown on CdTe(211)B/GaAs(211) composite substrates were generally of high quality, despite the presence of precipitates at the HgCdTe/CdTe interface.

REFERENCES

[1] W.F. Zhao, R.N. Jacobs, M. Jaime-Vasquez, L.O. Bubulac and D.J. Smith, J. Electron. Mater. **40**, 1733 (2011).

[2] M.A. Kinch, J. Electron. Mater. **39**, 1043 (2010).

[3] T.J. de Lyon, J.E. Jensen, M.D. Gorwitz, C.A. Cockrum, S.M. Johnson, and G.M. Venzor, J. Electron. Mater. **28**, 705 (1999).

[4] D.J. Smith, S.C.Y. Tsen, D. Chandrasekhar, P.A. Crozier, S. Rujirawat, G. Brill, Y.P. Chen, R. Sporken, and S. Sivananthan, Mater. Sci. Eng. **B77**, 93 (2000).

[5] Y. Chen, S. Farrell, G. Brill, P. Wijewarnasuriya, and N. Dhar, J. Cryst. Growth **310**, 5303 (2008).

[6] R.N. Jacobs, P.J. Smith, J.K. Markunas, J.D. Benson, and J. Pellegrino, J. Electron. Mater. **39**, 1036 (2010).

[7] Y.P. Chen, S. Sivananthan, and J.P. Faurie, J. Electron. Mater. **22**, 951 (1993).

[8] Y.P. Chen, J.P. Faurie, S. Sivananthan, G.C. Hua, and N. Otsuka, J. Electron. Mater. **24**, 475 (1995).

[9] Y. Xin, N.D. Browning, S. Rujirawat, S. Sivananthan, Y.P. Chen. P.D. Nellist, and S.J. Pennycook, J. Appl. Phys. **84**, 4292 (1998).

[10] H.Y. Wei, L. Salamance-Riba, and N.K. Dhar, Mat. Res. Soc. Symp. Proc. **484**, 329 (1998).

[11] N.K. Dhar, C.E.C. Wood, A. Gray, H.Y. Wei, L. Salamanca-Riba, and J.H. Dinan, J. Vac. Sci. Technol. **B14**, 2366 (1996).

[12] N.K. Dhar, P.R. Boyd, M. Martinka, J.H. Dinan, L.A. Almeida, and N. Goldsman, J. Electron. Mater. **29**, 748 (2000).

[13] N.K. Dhar, N. Goldsman, and C.E.C. Wood, Phys. Rev. B **61**, 8256 (2000).

[14] B. Brill, Y. Chen, N.K. Dhar, and R. Singh, J. Electron Mater. **32**, 717 (2003).

[15] M. Jaime-Vasquez, M. Martinka, R.N. Jacobs, and M. Groenert, J. Electron Mater. **35**, 1455 (2006).

[16] M. Jaime-Vasquez, M. Martinka, R.N. Jacobs, and J.D. Benson, J. Electron Mater. **36**, 905 (2007).

[17] M. Jaime-Vasquez, R.N. Jacobs, J.D. Benson, A.J. Stoltz, L.A. Almeida, L.O. Bubulac, Y. Chen, and G. Brill, J. Electron Mater. **39**, 951 (2010).

[18] W. Kern, and D.A. Puotinen, RCA Rev. **31**, 187 (1970).

[19] R.N. Jacobs, J. Markunas, J. Pellegrino, L.A. Almeida, M. Groenert, M. Jaime-Vasquez, N. Mahadik, C. Andrews, and S.B. Qadri, J. Cryst. Growth. **310**, 2960 (2008).

[20] C. Wang, D.J. Smith, S. Tobin, T. Parodos, J. Zhao, Y. Chang, and S.Sivananthan, J. Vac. Sci. Technol. A **24**, 995 (2006).

[21] S. Rujirawat, Y. Xin, N.D. Browning, S. Sivananthan, D.J. Smith, S.C.Y. Tsen, Y.P. Chen, and V. Nathan, Appl. Phys. Lett. **74**, 2346 (1999).

[22] M.D. Lange, R. Sporken, K.K. Mahavadi, J.P. Faurie, Y. Nakamura, and N. Otsuka, Appl. Phys. Lett. 58, 1988 (1991).

[23] J.P. Faurie, R. Sporken, Y.P. Chen, M.D. Lange and S. Sivananthan, Mater. Sci. Eng. **B16**, 51 (1993).

Chapter 5

MICROSTRUCTURAL CHARACTERIZATION OF HGCDTE GROWN BY MOLECULAR BEAM EPITAXY ON ZNTE/SI(112) AND GASB(112) SUBSTRATES

The research described in this chapter was carried out in collaboration with Dr. Greg Brill and colleagues from U.S. Army Research Laboratory (Adelphi, MD). The overall purpose of this project is to develop a better understanding of the proper conditions needed to achieve high-quality HgCdSe growth by molecular beam epitaxy (MBE) on ZnTe/Si(112) and GaSb(112) substrates. My role has been the microstructural characterization using electron microscopy. The results of this study have recently been submitted for publication.[1]

5.1 Introduction

HgCdTe has played a significant role in infrared (IR) focal-plane-array (FPA) technology for more than 50 years, and it continues to be a dominant material technology for all IR spectral bands.[2] The ongoing development of IRFPAs requires high sensitivity, small pixel size, large-area substrates, low cost, low dislocation density, and long-term thermal-cycling reliability.[3] However, the development of third-generation IRFPAs using HgCdTe grown on scalable substrates, such as Si, has been hindered by the approximately 100 times greater dislocation density relative to material grown on CdZnTe substrates.[4] This higher

dislocation density results in lower device performance, especially in the long-wavelength infrared (LWIR) regime.[5]

It has been proposed that HgCdSe could provide performance similar to HgCdTe in terms of its IR response, with the added advantage that large-area substrates are readily available commercially.[6] Analogous to the alloying of HgTe and CdTe, HgSe and CdSe crystallize in the zincblende structure and also form continuous alloys of $Hg_{1-x}Cd_xSe$. The bandgap of this alloyed material can then be tuned simply by adjusting the composition x to absorb any IR wavelength, similar to the situation for $Hg_{1-x}Cd_xTe$. In addition, two commercially available III-V binary semiconductors, namely InAs and GaSb, are nearly lattice-matched to HgCdSe and can thus be used as large-area substrates. With the small lattice mismatch between these substrates and HgCdSe, it seems reasonable to expect that the final HgCdSe dislocation density could be similar to the dislocation densities obtained for HgCdTe grown on bulk CdZnTe substrates.

There is very little information about the epitaxial growth of HgCdSe published in the scientific literature, even though the first paper about the growth of HgCdSe on ZnTe and CdZnTe substrates using molecular beam epitaxy (MBE) was published in 1993.[7] Recently, HgCdSe growth by MBE on ZnTe/Si(112) and GaSb(112) substrates was demonstrated.[6] It was reported that the optimal substrate temperature range for HgCdSe growth was between 80°C and 100°C, and it was found that materials grown at higher temperature generally had poorer quality, as determined using X-ray diffraction (XRD) rocking curves and Nomarski optical microscopy studies of surface morphology. In this chapter,

transmission electron microscopy (TEM) has been used to characterize samples of HgCdSe grown by MBE at different temperatures on closely-lattice-matched substrates of ZnTe/Si(112) and GaSb(112).

5.2 Experimental details

The ZnTe/Si(112) and GaSb(112) substrate surfaces were prepared carefully before the HgCdSe growth was initiated. The ZnTe/Si substrate preparation was similar to that used for CdTe/Si substrates intended for HgCdTe growth. Methanol solutions of dilute bromine were used to remove approximately 0.3 μm of the ZnTe surface layer, followed by several methanol rinses and a dilute HCL:deionized (DI) water dip to remove any residual oxide. The samples were then rinsed in DI water for 2 min to 4 min. Once loaded into the MBE chamber, the substrates were heated to remove any excess Te. The final heating was done under Te overpressure to ensure that no surface roughening occurred. This process was monitored *in situ* by reflection-high-energy electron diffraction (RHEED). The GaSb substrates were firstly heated to 590°C under an Sb flux in a III-V MBE system to remove the native oxide layer from the surface, followed by deposition of an approximate 0.2 μm-thick GaSb homoepitaxial layer at 500°C. This substrate preparation process was taken directly from the III-V growth process normally used for GaSb(001) substrates. A thin layer of As was then deposited at room temperature to prevent reoxidation of the GaSb surface during transportation from the III-V system through atmosphere to the II-VI system. The As layer was then thermally desorbed in the II-VI MBE chamber. HgCdSe growth

was conducted using elemental Hg, Cd, and Se sources, with variations in growth temperature and flux to investigate the effects on the $Hg_{1-x}Cd_xSe$ material quality. The $Hg_{1-x}Cd_xSe$ layers were typically grown to thicknesses in the range of 4-10 μm, with *x* ranging from 0.18 to 0.28.

Samples suitable for TEM observation were prepared in the cross-sectional geometry using standard mechanical polishing and dimpling to thicknesses of about 30μm, followed by argon-ion-milling at liquid nitrogen temperature to minimize any ion-milling-induced artefacts.[8] Low-angle, low-voltage (approximately 2.0keV) milling was used for final thinning to minimize the formation of any amorphous surface or interfacial layers. The electron microscopy observations were mostly carried out using a JEOL JEM-4000EX high-resolution electron microscope (HREM), operated at 400keV and equipped with a double-tilt, top-entry-type specimen holder. HAADF or "Z-contrast" imaging and EDXS analysis were carried out using a JEOL 2010F TEM, equipped with a field-emission electron gun and operated at 200keV. Samples were usually oriented for TEM observation along the common <110> projection. Nomarski microscopy, also known as differential interference contrast microscopy, was used to examine the topography of the the top surface of the epitaxial grown HgCdSe layers.

5.3 Results and discussion

For epitaxial $Hg_{0.71}Cd_{0.29}Se$ layers grown on ZnTe/Si(112) composite substrates at 100°C, very few structural defects were observed in cross-sectional

TEM images, as shown in Fig. 5.1 (a), and the top surfaces were generally smooth, as shown by the corresponding Nomarski optical micrograph in Fig. 5.1 (b). For $Hg_{0.80}Cd_{0.20}Se$ layers grown at 140°C, additional {111}-type stacking defects were visible near the HgCdSe/ZnTe interface, as shown arrowed in Fig. 5.1 (c), while the top $Hg_{0.80}Cd_{0.20}Se$ surface showed evidence for pitting, as visible in Fig. 5.1 (d). When the Se/Hg flux ratio was increased at the same growth temperature of 140°C, high dislocation densities were observed in parts of the $Hg_{0.79}Cd_{0.21}Se$ epilayer, as shown in Fig. 5.1 (e), and the surface displayed an odd type of defect structure which has not yet been identified, as shown in Fig. 5.1 (f). The high-resolution electron micrograph of the $Hg_{0.71}Cd_{0.29}Se$/ZnTe interface region shown in Fig. 5.2 confirmed the high-quality $Hg_{0.71}Cd_{0.29}Se$ epitaxial growth achieved at the lower growth temperature (T=100°C).

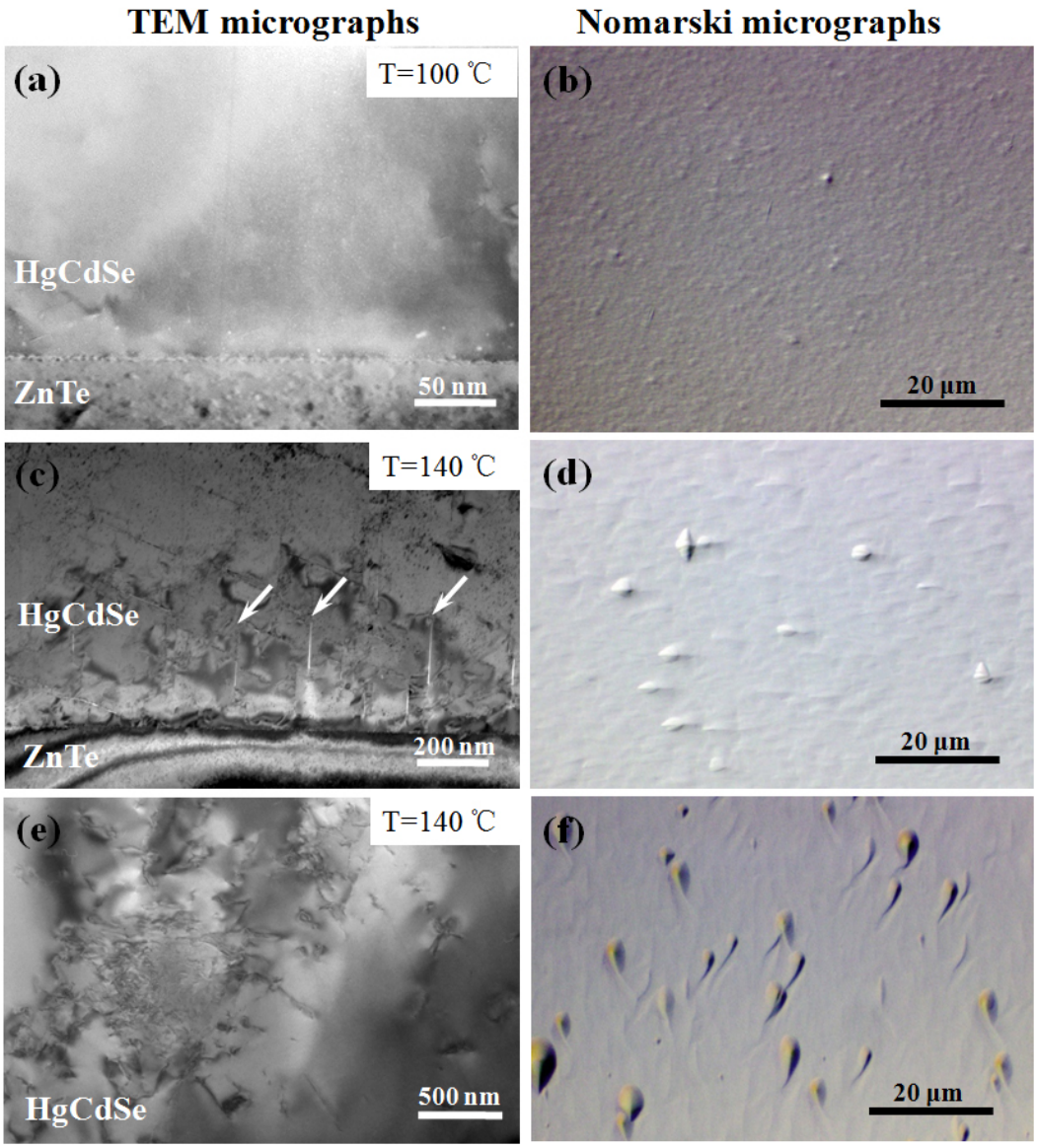

Fig. 5.1. (a), (c) and (e): cross-sectional electron micrographs of $Hg_{1-x}Cd_xSe$/ZnTe(112) heterostructure grown at T=100°C, 140°C and 140°C; (b), (d), and (f): Nomarski optical images of the corresponding $Hg_{1-x}Cd_xSe$ surface.

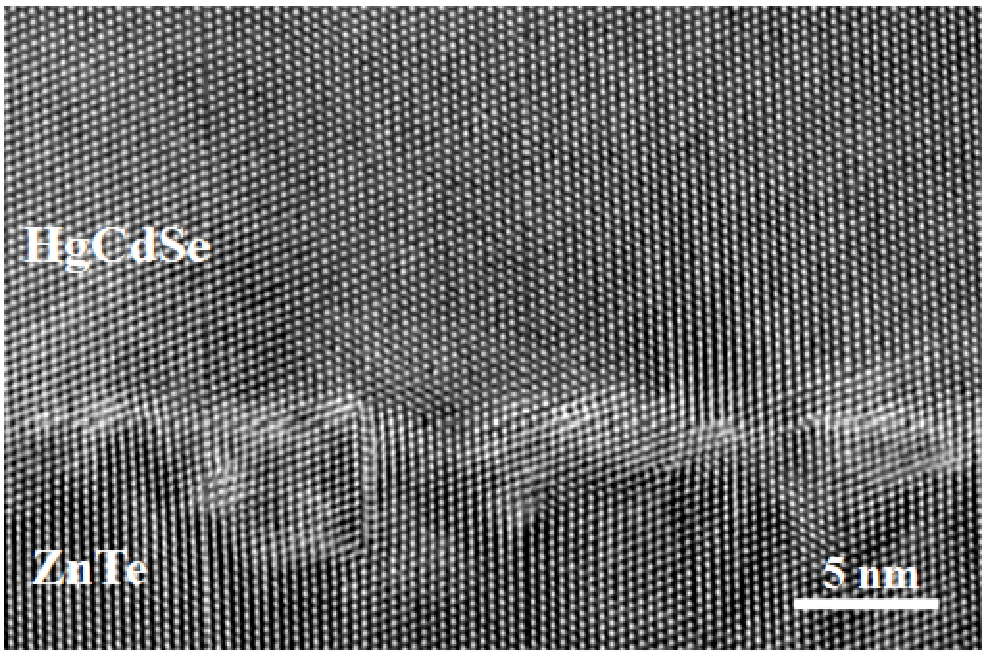

Fig. 5.2. High-resolution electron micrograph of $Hg_{0.71}Cd_{0.29}Se$/ZnTe(112) interface showing high-quality epitaxial growth of $Hg_{0.71}Cd_{0.29}Se$ achieved at T=100°C on ZnTe/Si(112) composite substrate.

The epitaxial $Hg_{0.81}Cd_{0.19}Se$ films grown on GaSb(112) substrates with GaSb(112) buffer layers were generally of good quality, and most growth defects again terminated close to the interface, as shown by the representative cross-sectional electron micrograph in Fig. 5.3. The high-resolution electron micrograph shown in Fig. 5.4 confirmed that high quality epitaxial growth of $Hg_{0.81}Cd_{0.19}Se$ layers could be achieved, despite the lack of flatness of the GaSb(112) buffer layer surface. When growth of the GaSb buffer layer was not well optimized, poorer quality HgCdSe layers were produced.

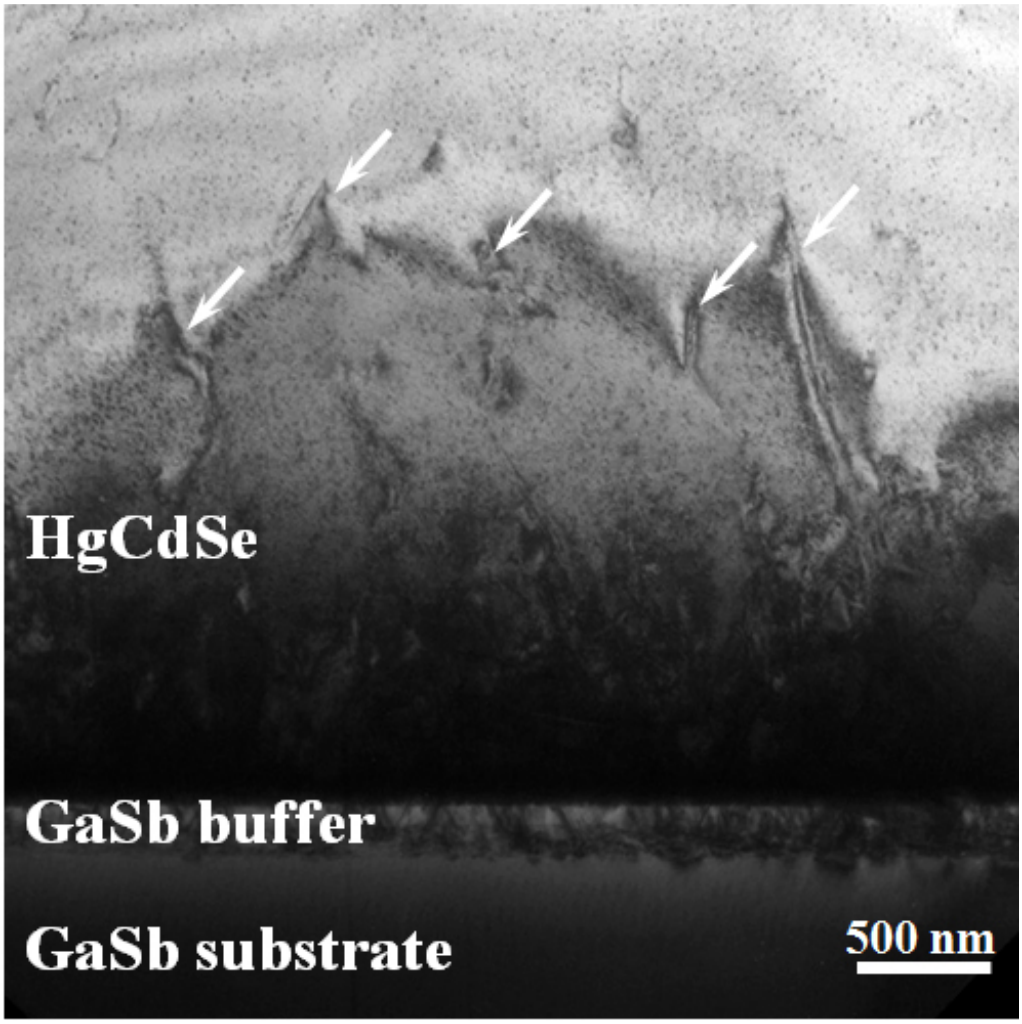

Fig. 5.3. Cross-sectional electron micrograph of $Hg_{0.81}Cd_{0.19}Se$/GaSb(112) heterostructure grown at T=110°C showing $Hg_{0.81}Cd_{0.19}Se$ film with low density of dislocations.

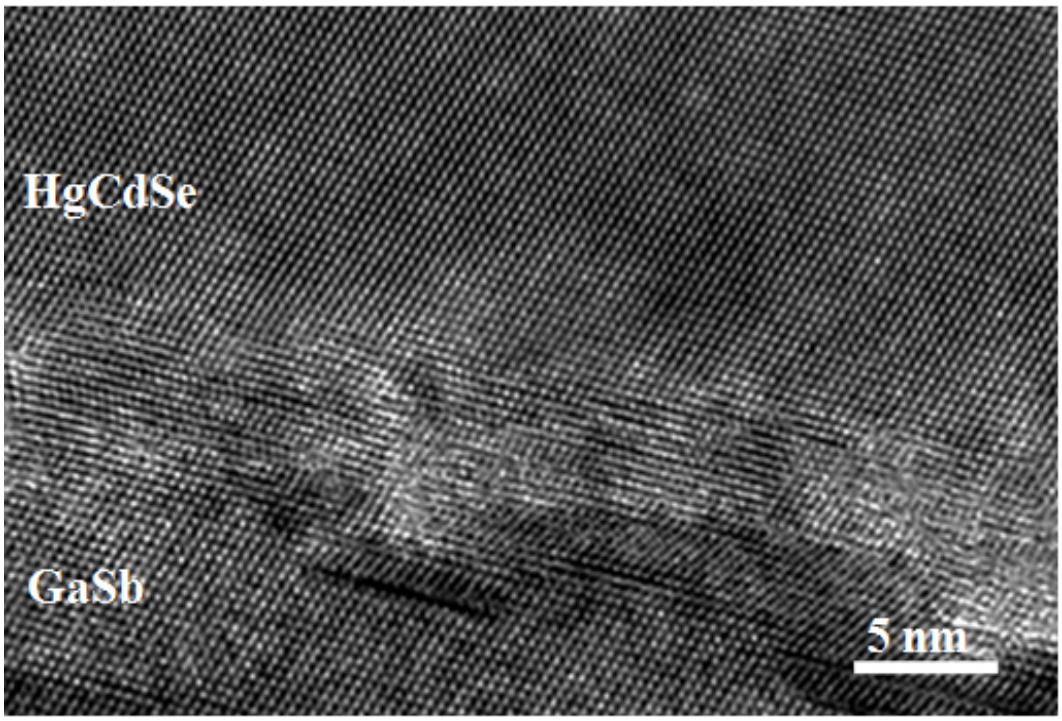

Fig. 5.4. High-resolution electron micrograph of $Hg_{0.81}Cd_{0.19}Se$/GaSb(112) interface showing epitaxial growth of $Hg_{0.81}Cd_{0.19}Se$ at T=110°C.

Figure 5.5 shows an example where the HgCdSe/GaSb buffer interface was very uneven, causing the subsequent HgCdSe layer to develop a pronounced columnar structure. This result demonstrates the importance of optimizing the buffer growth, and indicates that a new buffer growth process will need to be developed for future studies involving GaSb(112) surfaces.

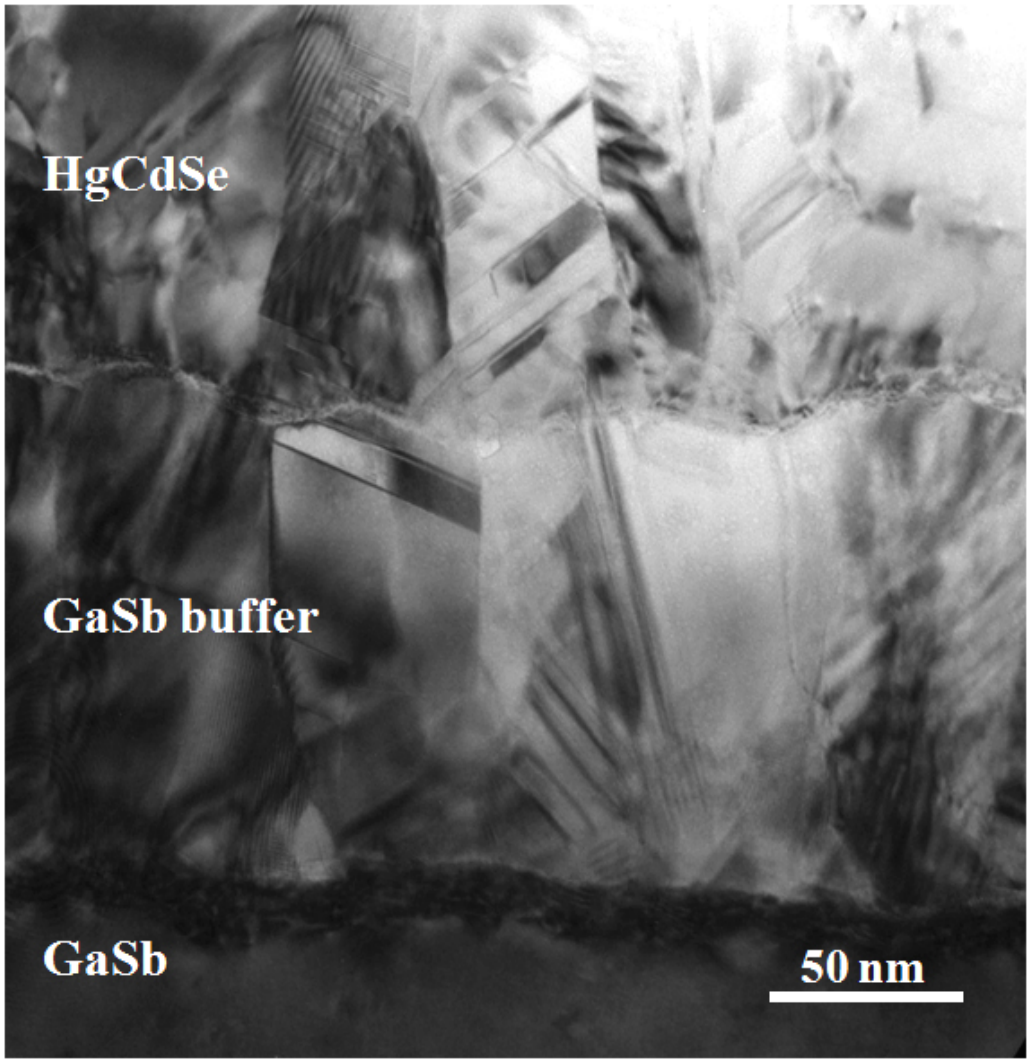

Fig. 5.5. Cross-sectional electron micrograph of HgCdSe/GaSb buffer/GaSb(112) heterostructure showing polycrystalline HgCdSe film with columnar structure.

The Z-contrast image in Fig. 5.6 (a) shows a region of dark contrast at the $Hg_{0.81}Cd_{0.19}Se$/GaSb interface and Fig. 5.6 (b) shows an EDXS line profile taken along the arrowed region. These results reveal the presence of a Ga-rich region at the surface of the GaSb buffer layer, which was presumably caused when the substrate was heated to remove As and O, also causing removal of Sb.

Strain fields were also observed originating from the presence of small plate-like defects, as shown in Fig. 5.7 (a), but it has not yet been established whether these features are dislocation loops or precipitates. Figure 5.7 (b) is a high-resolution electron micrograph showing the atomic-scale microstructure of one of these defects, which lies predominantly along $\{111\}_{HgCdSe}$ planes. Although the defect is not fully coherent with the HgCdSe matrix, no missing or extra planes are visible. It has proven to be difficult to analyze these precipitates in detail because of their small size and low density. Similar types of defects have been previously reported to occur during growth of HgCdTe.[9]

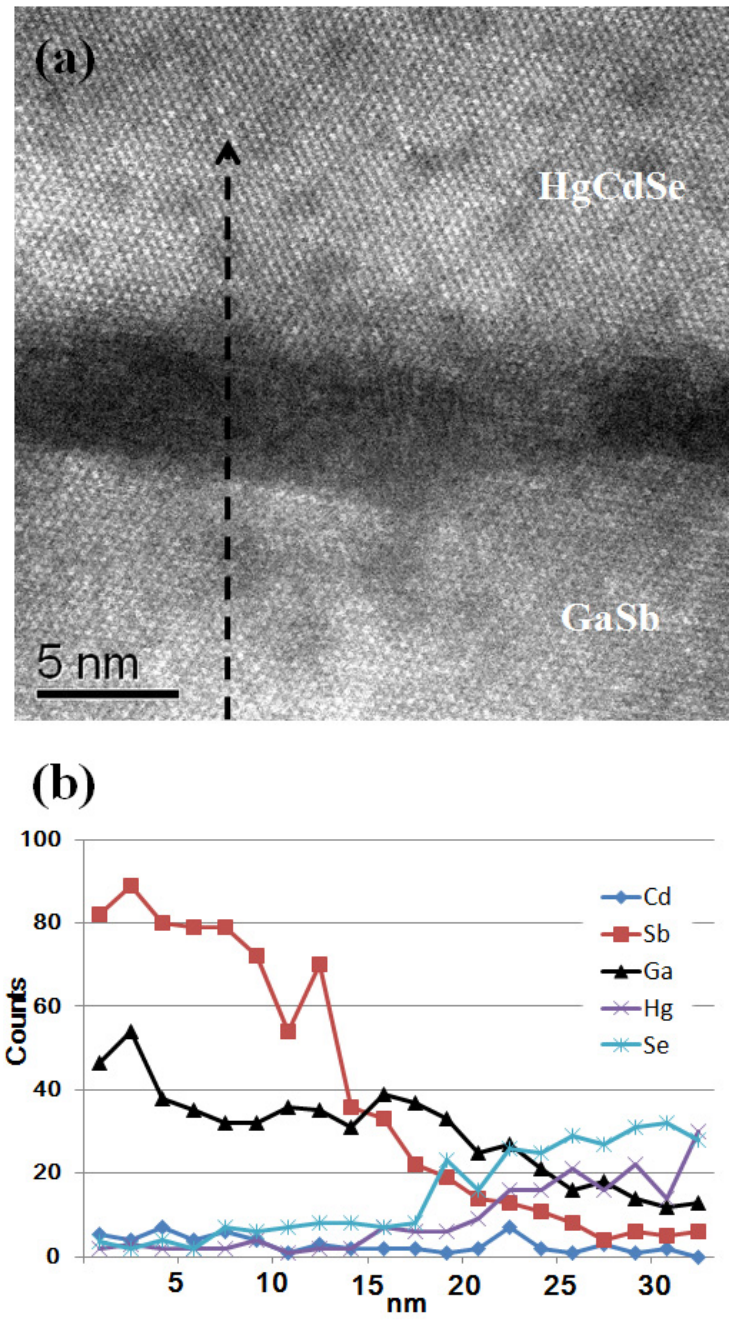

Fig. 5.6. Compositional analysis of $Hg_{0.81}Cd_{0.19}Se$/GaSb(112) heterostructure. (a) HAADF image of $Hg_{0.81}Cd_{0.19}Se$/GaSb(112) interfacial region used for analysis; (b) EDXS elemental profile along line indicated in (a).

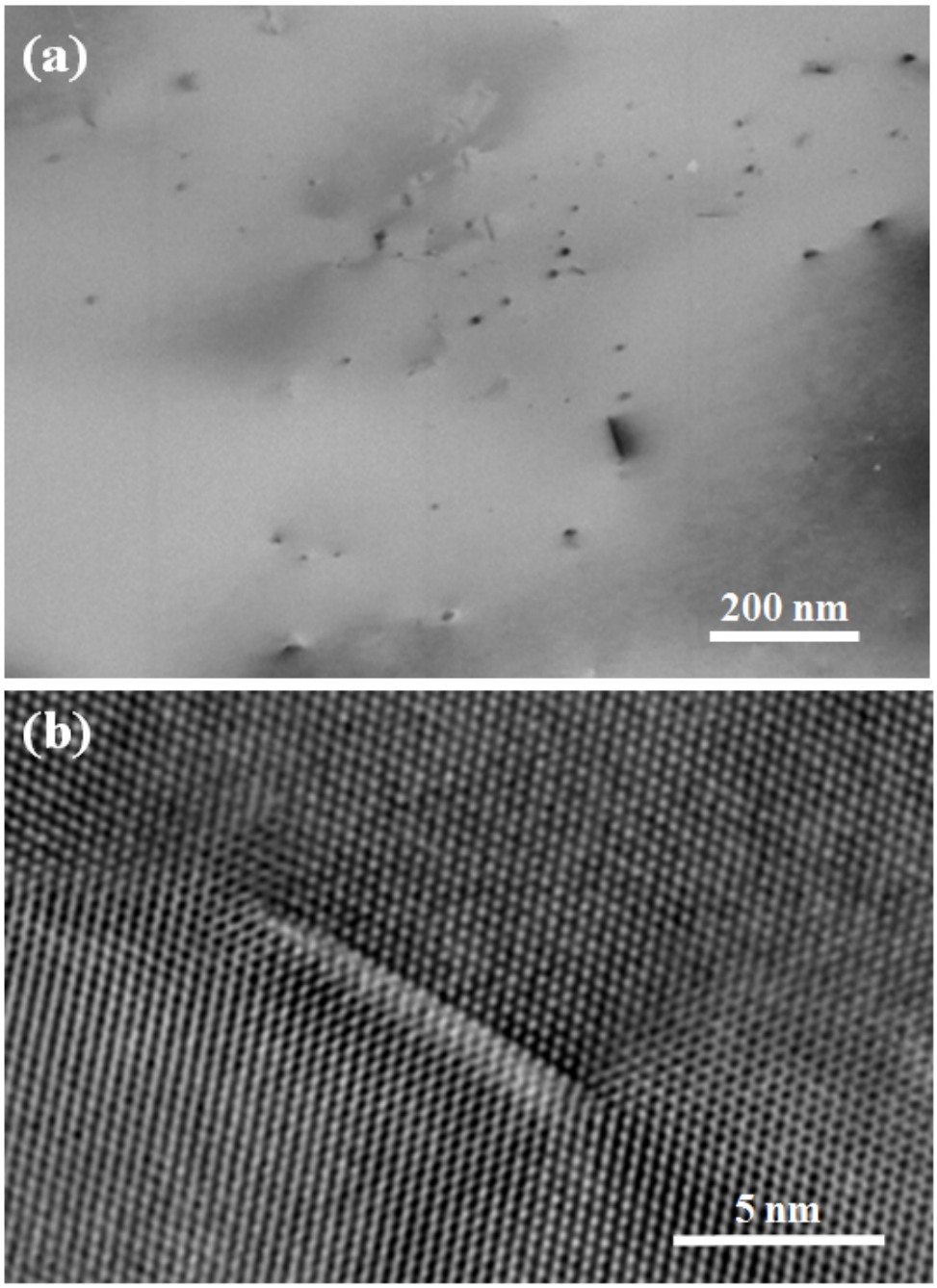

Fig. 5.7. (a) Low magnification electron micrograph showing small plate-like defects present in HgCdSe epilayer; (b) high-resolution electron micrograph showing microstructure of plate-like defects observed in cross-section.

5. 4 Conclusions

In summary, the microstructure of HgCdSe thin films grown by MBE on ZnTe/Si(112) and GaSb(112) substrates has been characterized. The quality of the HgCdSe growth was dependent on the growth temperature and materials flux, independent of the substrate. The materials grown at 100°C were generally of high quality, while those grown at 140°C had {111}-type stacking defects and higher dislocation densities. For epitaxial growth of HgCdSe on GaSb(112) substrates, better preparation of the GaSb buffer layer will be needed in order to ensure that high-quality HgCdSe can be grown on a consistent basis.

REFERENCES

[1] W.F. Zhao, G. Brill, Y. Chen, and D.J. Smith, J. Electron. Mater. (2012). (In press)

[2] M.A. Kinch, J. Electron. Mater. **39**, 1043 (2010).

[3] M.A. Kinch, J. Electron. Mater. **29**, 809 (2000).

[4] S. Farrell, G. Brill, Y. Chen, P.S. Wijewarnasuriya, Mulpuri V. Rao, N. Dhar, and K. Harris, J. Electron. Mater. **39**, 43 (2010).

[5] T. Parodos, E.A. Fitzgerald, A. Caster, S. Tobin, J. Marciniec, J. Welsch, A. Hairston, P. Lamarre, J. Riendeau, B. Woodward, S. Hu, M. Reine, and P. Lovecchio, J. Electron. Mater. **36**, 1068 (2007).

[6] G. Brill, Y. Chen, and P. Wijewarnasuriya, J. Electron. Mater. **40**, 1679 (2011).

[7] Y. Lansari, J.W. Cook, and J.F. Schetzina, J. Electron. Mater. **22**, 809 (1993).

[8] C. Wang, D.J. Smith, S. Tobin, T. Parodos, J. Zhao, Y. Chang and S. Sivananthan, J. Vac. Sci. Technol. A **24**, 995 (2006).

[9] T. Aoki, Y. Chang, G. Badano, J. Zhao, C. Grein, S. Sivananthan, D.J. Smith, J. Cryst. Growth **265**, 224 (2004).

Chapter 6

SUMMARY AND FUTURE WORK

6.1 Summary

The research of this dissertation has involved the use of transmission electron microscopy (TEM) to characterize HgCdTe and HgCdSe epilayers and HgCdTe-based devices grown by liquid-phase epitaxy (LPE) and molecular beam epitaxy (MBE).

The growth of CdTe passivation layers on HgCdTe by different techniques has been compared.[1] TEM imaging was used to investigate the structural properties of the CdTe passivation layers, as well as to determine the effect of annealing on the CdTe/HgCdTe interface. The CdTe grains were larger and more irregular in shape when deposited by the hot-wall epitaxy method, while those deposited by MBE were generally well textured with mostly vertical grain boundaries. The flatness and abruptness of the CdTe/HgCdTe interface for the MBE-grown CdTe was shown by several different TEM methods to be substantially improved by annealing.

The CdTe(211)B/ZnTe/Si(211) heterostructures grown by MBE were evaluated using different TEM techniques.[2] HREM imaging revealed the morphology of the CdTe(211)B/ZnTe/Si(211) interface and showed that most stacking faults formed at the Si substrate surface continued through the thin ZnTe layer, terminating near the point of initiation of CdTe growth. Lattice-spacing measurements and microanalytical studies mapped out chemical profiles across

the CdTe(211)B/ZnTe/Si heterostructures, and indicated that interdiffusion between CdTe and ZnTe had occurred. HAADF imaging revealed that the region of the CdTe/ZnTe interface was quite disordered and uneven in thickness. The average width of the ZnTe layer and the (Cd, Zn)Te transition region were measured to be approximately 6.5 nm and 3.5 nm, respectively. Preliminary observations of CdTe(211)B/GaAs(211) heterostructures suggest much reduced defect densities both near the vicinity of the substrate and within the CdTe epilayers. The HgCdTe epilayer grown on the CdTe(211)B/GaAs(211) composite substrate was generally of high quality, despite the presence of small precipitates at the HgCdTe/CdTe interface.

The microstructure of HgCdSe thin films grown by MBE on ZnTe/Si(112) and GaSb(112) substrates was characterized.[3] The quality of the HgCdSe growth was dependent on the growth temperature and materials flux, independent of the substrate. The materials grown at 100°C were generally of good quality, while those grown at 140°C had {111}-type stacking defects and increased dislocation densities. For epitaxial growth of HgCdSe on GaSb substrates, careful preparation of the GaSb buffer layer was shown to be essential in order to ensure that high-quality HgCdSe could be grown.

6.2 Future work

6.2.1 Minimization of ion-milling damage

Ion-milling damage during TEM sample preparation has been a serious ongoing issue for II-VI materials for many years.[4-6] During this research, it was

consistently observed that argon-ion milling had induced severe damage in CdTe material, even when the sample was milled at very low energy and held properly at liquid nitrogen temperature. In order to eliminate this ion-milling damage, methanol solutions of either dilute bromine or dilute iodine should be used to etch the samples after ion milling.

6.2.2 Origins of precipitates at the HgCdTe/CdTe interface

Precipitates were observed at the HgCdTe/CdTe interface were observed, but it was unclear what had caused the formation of these defects. Further high-resolution electron microscopy and small-probe microanalysis of the precipitates need to be carried out. In order to do this, samples will need to be very carefully prepared so that the region of interest is very thin and free of contamination.

6.2.3 Identification of the chemistry of precipitates in HgCdSe

Strain fields were observed originating from the presence of small plate-like defects in HgCdSe epilayers, but it has not yet been established whether these features are dislocation loops or precipitates.[3] It has proven to be difficult to analyze these precipitates in detail because of their small size and low density. Sample contamination might be another serious drawback since modification of the sample may occur as a result of plasma cleaning. Further studies are essential to identify the chemistry of the precipitates by utilizing Z-contrast imaging together with small-probe microanalysis.

6.2.4 Growth of HgCdSe by MBE

TEM characterization of HgCdSe epitaxial material was carried out for the first time.[3] It is clear that much attention will need to be directed towards developing proper growth conditions to achieve high-quality HgCdSe by MBE on either ZnTe/Si(112) or GaSb(112) substrates. The optimal window of the growth temperature still needs to be established. Substrate surface cleaning methods will also need to be improved in order to achieve better quality HgCdSe material.

REFERENCES

[1] W.F. Zhao, J. Cook, T. Parodos, S. Tobin, and D.J. Smith, J. Electron. Mater. **39**, 924 (2010).

[2] W.F. Zhao, R.N. Jacobs, M. Jaime-Vasquez, L.O. Bubulac and D.J. Smith, J. Electron. Mater. **40**, 1733 (2011).

[3] W.F. Zhao, G. Brill, Y. Chen, and D.J. Smith, J. Electron. Mater. (2012). (In press)

[4] C. Wang, D.J. Smith, S. Tobin, T. Parodos, J. Zhao, Y. Chang and S. Sivananthan, J. Vac. Sci. Technol. A **24**, 995 (2006).

[5] A.G. Cullis, N.G. Chew and J.L. Hutchison, Ultramicroscopy **17**, 203 (1985).

[6] T. Aoki, Y. Chang, G. Badano, J. Zhao, C. Grein, S. Sivananthan, D.J. Smith, J. Cryst. Growth **265**, 224 (2004).

APPENDIX A

REFERENCES

Agnihotri, O.P. and *et al.*, Semicond. Sci. Technol. **13**, 839 (1998).

An, S.Y. and *et al.*, J. Electron. Mater. **31**, 683 (2002).

Aoki, T. and *et al.*, J. Cryst. Growth **265**, 224 (2004).

Aoki, T. and *et al.*, J. Cryst. Growth **271**, 29 (2004).

Ariel, V. and *et al.*, J. Electron. Mater. **24**, 1169 (1995).

Brill, G. and *et al.*, J. Electron Mater. **32**, 717 (2003).

Brill, G. and *et al.*, J. Electron. Mater. **40**, 1679 (2011).

Bubulac, L.O. and *et al.*, J. Electron. Mater. **24**, 1175 (1995).

Capper, P., Properties of Narrow Gap Cadmium-based Compounds (EMIS Datareviews Series No. 10) (1994).

Cullis, A.G. and *et al.*, Ultramicroscopy **17**, 203 (1985).

Chen, Y.P. and *et al.*, J. Electron. Mater. **22**, 951 (1993).

Chen, Y.P. and *et al.*, J. Electron. Mater. **24**, 475 (1995).

Chen, Y.P. and *et al.*, J. Cryst. Growth **310**, 5303 (2008).

Dhar, N.K. and *et al.*, J. Vac. Sci. Technol. **B14**, 2366 (1996).

Dhar, N.K. and *et al.*, J. Electron. Mater. **29**, 748 (2000).

Dhar, N.K. and *et al.*, Phys. Rev. B **61**, 8256 (2000).

Farrell, S. and *et al.*, J. Electron. Mater. **39**, 43 (2010).

Faurie, J.P. and *et al.*, Mater. Sci. Eng. **B16**, 51 (1993).

Fertig, J. and *et al.*, Optik **59**, 407 (1981).

Finkman, E. and *et al.*, J. Appl. Phys. **56**, 2896 (1984).

Golding, T.D. and *et al.*, J. Electron. Mater. **32**, 882 (2003).

Hansen, G.L. and *et al.*, J. Appl. Phys. **53**, 7099 (1982).

Hansen, G.L. and *et al.*, J. Appl. Phys. **54**, 1639 (1983).

Harman, T.C. and *et al.*, J. Electron. Mater. **8**, 191 (1979).

Herman, M.A. and *et al.*, Molecular Beam Epitaxy: Fundamentals and Current Status (Springer Series in Materials Science), (1989).

Horn, S. and *et al.*, Proc. SPIE **5074**, 44 (2003).

Howie, A., J. Microsc. **17**, 11 (1979).

Jaime-Vasquez, M. and *et al.*, J. Electron Mater. **35**, 1455 (2006).

Jaime-Vasquez, M. and *et al.*, J. Electron Mater. **36**, 905 (2007).

Jaime-Vasquez, M. and *et al.*, J. Electron Mater. **39**, 951 (2010).

Kern, W. and *et al.*, RCA Rev. **31**, 187 (1970).

Kinch, M.A., and *et al.*, J. Electron. Mater. **29**, 809 (2000).

Kinch, M.A., and *et al.*, J. Electron. Mater. **39**, 1043 (2010).

Kirkland, E.J. and *et al.*, Ultramicroscopy **23**, 77 (1987).

Kruse, P.W., Semicond. Semimet. **18**, 1 (1981).

Kumar, V. and *et al.*, J. Electron. Mater. **34**, 1225 (2005).

Lakner, H. and *et al.*, J. Phys. D: Appl. Phys. **29**, 1767 (1996).

Lansari, Y. and *et al.*, J. Electron. Mater. **22**, 809 (1993).

Lawson, W.D. and *et al.*, J. Phys. Chem. Solids **9**, 325 (1959).

Loane, R.F. and *et al.*, Acta Crystallogr. A **44**, 912 (1988).

Lyon,T.J. and *et al.*, J. Electron. Mater. **28**, 705 (1999).

Mattson, M.A. and *et al.*, J. Electron. Mater. **26**, 578 (1997).

Micklethwaite, W.F.H., Semicond. Semimet. **18**, 47, (1981).

Muller, D.A., Nature Mater. **8**, 263 (2009).

Norton, P. and *et al.*, Proc. SPIE **4130**, 226 (2000).

Norton, P., Opto-Electron. Rev. **10**, 159 (2002).

Parodos, T. and *et al.*, J. Electron. Mater. **36**, 1068 (2007).

Reago, D. and *et al.*, Proc. SPIE **3701**, 108 (1999).

Reddy, M. and *et al.*, J. Electron. Mater. **37**, 1274 (2008).

Rogalski, A., Rep. Prog. Phys. **68**, 2267 (2005).

Rogalski, A., Infrared Phys. Technol. **50**, 240 (2007).

Rujirawat, S. and *et al.*, Appl. Phys. Lett. **71**, 1810 (1997).

Rujirawat, S. and *et al.*, Appl. Phys. Lett. **74**, 2346 (1999).

Ryu, T.S. and *et al.*, Mater. Sci. Eng. B **122**, 80 (2005).

Scott, M.W., J. Appl. Phys. **1**, 239 (1962).

Singh, R.R. and *et al.*, Semicond. Sci. Technol. **23**, 1 (2008).

Smith, D.J. and *et al.*, Mater. Sci. Eng. **B77**, 93 (2000).

Tennant, W.E. and *et al.*, J. Vac. Sci. Technol. **B 10**, 1359 (1992).

Wall, J. and *et al.*, Proc. Natl Acad. Sci. **71**, 1 (1974).

Wang, C. and *et al.*, J. Vac. Sci. Technol. A **24**, 995 (2006).

Wang, C. and *et al.*, J. Electron. Mater. **35**, 1192 (2006).

Wei, H.Y. and *et al.*, Mat. Res. Soc. Symp. Proc. **484**, 329 (1998).

Zhao, W.F. and *et al.*, J. Electron. Mater. **39**, 924 (2010).

Zhao, W.F. and *et al.*, J. Electron. Mater. **40**, 1733 (2011).

Zhao, W.F. and *et al.*, J. Electron. Mater. (2012). (In press)

APPENDIX B

TABLE OF ACRONYMS

CT	CdTe
EDXS	Energy Dispersive X-ray Spectroscopy
EELS	Electron Energy Loss Spectroscopy
EPD	Etch Pit Density
FIB	Focused Ion Beam
FPA	Focal Plane Array
HAADF	High Angle Annular Dark Field
HREM	High Resolution Electron Microscopy
HWE	Hot Wall Epitaxy
IR	Infrared
LPE	Liquid Phase Epitaxy
LWIR	Long Wavelength Infrared
MBE	Molecular Beam Epitaxy
MCT	HgCdTe
MWIR	Mid Wavelength Infrared
RHEED	Reflection High Energy Electron Diffraction
STEM	Scanning Transmission Electron Microscopy
SWIR	Short Wavelength Infrared
TEM	Transmission Electron Microscopy